



HAL
open science

Numerical study of constrained many-body systems

Bhupen Dabholkar

► **To cite this version:**

Bhupen Dabholkar. Numerical study of constrained many-body systems. Physics [physics]. Université de Toulouse, 2024. English. NNT : 2024TLSES068 . tel-04693055

HAL Id: tel-04693055

<https://theses.hal.science/tel-04693055v1>

Submitted on 10 Sep 2024

HAL is a multi-disciplinary open access archive for the deposit and dissemination of scientific research documents, whether they are published or not. The documents may come from teaching and research institutions in France or abroad, or from public or private research centers.

L'archive ouverte pluridisciplinaire **HAL**, est destinée au dépôt et à la diffusion de documents scientifiques de niveau recherche, publiés ou non, émanant des établissements d'enseignement et de recherche français ou étrangers, des laboratoires publics ou privés.

Doctorat de l'Université de Toulouse

préparé à l'Université Toulouse III - Paul Sabatier

Étude numérique des systèmes à N corps contraints

Thèse présentée et soutenue, le 11 juin 2024 par

Bhupen Dilip DABHOLKAR

École doctorale

SDM - SCIENCES DE LA MATIERE - Toulouse

Spécialité

Physique

Unité de recherche

LPT - Laboratoire de Physique Théorique

Thèse dirigée par

Fabien ALET

Composition du jury

M. Michel CAFFAREL, Président, CNRS Occitanie Ouest

M. Grégoire MISGUICH, Rapporteur, CEA Paris-Saclay

Mme Laura MESSIO, Rapporteur, Sorbonne Université

M. Didier POILBLANC, Examineur, CNRS Occitanie Ouest

M. Sumiran PUJARI, Examineur, Indian Institute of Technology Bombay

M. Fabien ALET, Directeur de thèse, CNRS Occitanie Ouest

Abstract

This thesis presents computational studies of three different models of many-body physics with direct or indirect constraints. The presence of constraints in complex many-body systems calls for non-trivial numerical algorithms to study them. The first two models which have a direct form of local constraint are the Rokhsar-Kivelson Quantum Dimer model (QDM) and a classical statistical mechanics model of non-intersecting loops with attractive interactions, both on the square lattice. The investigations of such constrained models have found a recent resurgence with their direct realizations on Rydberg atom arrays quantum simulators. The study of the classical model uses a Monte Carlo directed loop algorithm while the QDM calls for a novel Quantum Monte Carlo scheme based on the framework of Stochastic Series Expansions called the Sweeping Cluster Algorithm (SCA). We present a modification of the SCA in order to render simulations fully ergodic at finite temperature. For both models, our numerical studies show the existence of a critical phase separated by a phase transition at finite temperature to an ordered phase of dimers or loops which spontaneously breaks certain lattice symmetries. We show that for the case where the interaction is attractive this phase transition is of Kosterlitz-Thouless type and can be understood by constructing a coarse-grained field theory through a height mapping. The finite temperature phase diagram of the QDM presents an unusual re-entrance behavior in the critical phase. The final part of this thesis deals with the role of non-abelian symmetries in the thermalization process of quantum many-body systems. We study the high-energy eigenstates of a $SU(3)$ symmetric spin chain in presence of disorder. While the model does not directly have constraints, we perform exact diagonalization in a constrained basis of Young tableau making use of the full $SU(3)$ symmetry of the model. By looking at the commonly used probes for thermalization (spectral statistics, distribution of local observables and scaling of entanglement entropy), we show that the model exhibits a non-ergodic regime over a broad range of system sizes for strong enough disorder, contrasting with the rapid thermalization observed at weak disorder.

Résumé

Cette thèse présente une étude numérique de trois modèles de physique à N corps soumis à des contraintes directes ou indirectes. La présence de contraintes dans un système complexe à plusieurs corps requiert des algorithmes numériques non triviaux pour les étudier. Les deux premiers modèles comportent une forme directe de contrainte locale et sont le modèle de Dimères Quantiques (QDM) de Rokhsar-Kivelson et un modèle de mécanique statistique classique de boucles sans croisement avec des interactions attractives, tous les deux étudiés sur un réseau carré. L'étude de tels modèles contraints a connu un regain d'intérêt récemment avec leur réalisations directes sur des simulateurs quantiques de réseaux d'atomes de Rydberg. Les simulations du modèle classique utilisent l'algorithme Monte Carlo de boucles dirigées (Directed loop algorithm) tandis que le QDM nécessite un nouveau schéma de Monte Carlo quantique basé sur le cadre des expansions en séries stochastiques appelé Sweeping Cluster Algorithm (SCA). Nous présentons une modification du SCA pour rendre les simulations ergodiques à température finie. Notre étude numérique montre l'existence d'une phase critique dans les deux modèles séparée par une transition de phase à température finie vers une phase ordonnée de dimères ou de boucles qui brise spontanément certaines symétries du réseau. Nous montrons que dans le cas où les interactions sont attractives, cette transition de phase est de type Kosterlitz-Thouless et peut être comprise en construisant une théorie des champs de hauteurs. Le diagramme de phase à température finie du QDM présente quant à lui une ré-entrance inhabituelle dans la phase critique. La partie finale de cette thèse traite du rôle des symétries non-abéliennes dans les processus de thermalisation des systèmes quantiques. Nous étudions les états propres de haute énergies d'une chaîne de spins désordonnée avec une symétrie $SU(3)$. Le modèle n'a pas directement de contraintes mais nous effectuons une diagonalisation exacte dans une base contrainte de tableaux de Young en utilisant la symétrie $SU(3)$ complète de ce modèle. En examinant les sondes couramment utilisées pour la thermalisation (statistiques spectrales, distribution des observables locales et entropie d'intrication), nous montrons que le modèle présente un régime non ergodique sur une grande plage de tailles de système pour un désordre fort, contrastant avec la thermalisation rapide observée à faible désordre.

Dedication

I dedicate this thesis to my parents, to whom I am grateful for their constant love and support.

I would also like to dedicate this thesis to all the amazing friends I made in Toulouse, who I would cherish for the rest of my life.

Lastly but most importantly, I dedicate this thesis to my late grandfather P.D Samant who always encouraged me to pursue higher education and excellence in anything I chose to do.

Contents

1	Introduction	8
2	Quantum Dimer model on the square lattice	15
2.1	Quantum dimer model on the square lattice	15
2.1.1	Topological invariants	16
2.1.2	Monomers	18
2.1.3	Ground state phase diagram on the square lattice	18
2.1.4	Perspectives on other phases	22
2.2	Brief review of the Classical Interacting Dimer Model on the square lattice	22
2.2.1	Phase Diagram of CIDM	23
2.2.2	Height Mapping	24
2.2.3	Action for the high temperature phase	25
2.2.4	Coulomb Gas Construction	25
2.2.5	The Dimer Correlators	26
2.2.6	Fluctuations of Winding Numbers	26
3	Monte Carlo methods for Constrained models	28
3.1	Classical Monte Carlo	28
3.2	Directed Loop Monte Carlo	31

3.3	Stochastic Series Expansion	34
3.3.1	Monte Carlo updates	36
3.4	Sweeping Cluster Algorithm	38
3.4.1	Rules for building the Cluster	40
3.4.2	Cluster acceptance probability	40
3.5	Classical Loop Move	43
4	Finite temperature phase diagram of the QDM on square lattice	46
4.1	Quantum Dimer Model at finite temperature	46
4.1.1	Order parameters	47
4.1.2	Columnar side $V/t < 1$	48
4.1.3	Staggered side $V/t > 1$	49
4.1.4	Critical phase	50
4.2	High Temperature Expansion	54
4.3	Discussion and Perspectives	56
5	Interacting loop model on the square lattice	57
5.1	The model	58
5.2	Field theoretical description	59
5.2.1	Height Mapping	60
5.2.2	Sine-Gordon action revisited	60
5.3	Phase Diagram	62
5.3.1	Fluctuations of winding numbers	64
5.3.2	Susceptibility of nematic order parameter	65
5.3.3	Correlation functions	66

5.4	Discussion and outlook	70
6	Exact diagonalization of a disordered $SU(3)$ spin chain	74
6.1	Thermalization in quantum systems	75
6.1.1	Eigenstate thermalization hypothesis	75
6.1.2	Connection to Random matrix theory	77
6.1.3	Probes of ETH	78
6.2	Breakdown of ETH	79
6.2.1	Many body localization	80
6.2.2	Probes of MBL	80
6.2.3	Structure of MBL eigenstates : Local integrals of motion	82
6.2.4	Current status of MBL	82
6.3	Brief review of disordered $SU(2)$ spin chain.	83
6.3.1	Existence of a broad non-ergodic regime	84
6.4	$SU(N)$ Heisenberg Hamiltonian	85
6.4.1	Young tableau	86
6.4.2	Matrix elements in tableau basis	86
6.5	Results on disordered $SU(3)$ spin chains	87
6.5.1	Model and methods	88
6.5.2	Spectral statistics	89
6.5.3	Distribution of local observable	92
6.5.4	Scaling of entanglement entropy	95
6.6	Conclusion	96
7	Conclusion	98

8	Résumé en Français	101
8.1	Introduction	101
8.2	Diagramme de phase à température finie du modèle de dimères quantiques sur le réseau carré	106
8.3	Modèle classique de boucles en interactions sur le réseau carré	110
8.4	Régime non-ergodique dans une chaîne de spins désordonnée avec symétrie SU(3)	113
A	Exact expression for $\langle W^2 \rangle$ at $g = 1$	118
B	Computation of entanglement entropy in Young tableaux basis	120
	References	123

Chapter 1

Introduction

The goal of this introduction is to underline the importance of studying constrained models in condensed matter and statistical physics by describing various situations in which they emerge as effective models capturing the low energy physics. Our focus would be on models with a dimer or loop like constraint. Both the constraints are illustrated in Fig.1.1. Dimers could be viewed as objects which connect two lattice sites. For the model studied in this thesis, the dimers connect two neighbouring lattice sites and therefore live on the links of the lattice. In addition, they obey a hard-core constraint, i.e the dimers are arranged such that one and only one dimer touches a lattice site. A loop constraint is made up of closed loops on the links of the lattice passing through multiple sites.

Dimer models have been extensively studied in classical statistical physics. Introduced as a simple model for adsorption of diatomic molecules on crystalline surfaces [1], the dimer model caught attention after Kasteleyn [2] gave an exact solution to the partition function, which assigned fugacities to dimers on each type of bonds of the lattice. In its bare form the partition function boils down to enumerating exactly all the possible dimer coverings of the lattice. The problem in fact also bears resemblance to domino tiling problems in mathematics. In addition to Kasteleyn, an independent exact solution was also given by Temperley and Fisher [3] at the same time. However, in Kasteleyn's model, assigning on bond fugacities to the dimers resulted in a peculiar phase transition in which the specific heat below the transition temperature T_K is zero while above T_K it is non-zero and diverges as $(T - T_K)^{-1/2}$ which shows stark contrast to another familiar exactly solvable model, the 2D Ising model, where the specific heat has a logarithmic divergence. This class of phase transition is now called Kasteleyn type phase transitions. Note that the Kasteleyn solution for enumerating dimer coverings works only for planar graphs.

One of the most significant contributions of dimer models lies in their ability to map

onto other important physical models. Take for instance the classical Ising model on the triangular lattice with antiferromagnetic couplings. Since this is a frustrated model the ground state is an extensively degenerate manifold of different spin configurations. Fig.1.1 shows how each spin configuration could be mapped to a dimer covering on a dual Honeycomb lattice. As we will see in the next chapter, dimer coverings on bipartite lattices are critical, i.e they have power law decaying correlations. This mapping helps unveil the critical spin-spin correlations in the frustrated Ising model [4]. The mappings are not limited to 2D. The well known Coulomb phase observed experimentally in spin ice materials [5] could also be understood by a similar dimer mapping in 3D [6]. Moreover, dimer models find their use beyond classical models. A dimer on a bond could represent a spin-1/2 singlet state $1/\sqrt{2}(|\uparrow\downarrow\rangle - |\downarrow\uparrow\rangle)$ of two spins on the neighbouring sites. A state made of such singlets was proposed by Anderson as a mechanism by which a quantum antiferromagnet could escape long-range magnetic ordering leading to a spin liquid phase [7]. Rokhsar and Kivelson [8], building up on this go further and consider a "quantum hard-core dimer gas" essentially washing out the spin degrees of freedom. This is the beginning of the Quantum dimer model which we will explore in the next chapter.

In some systems loop constraints arise in subtle ways, as effective degrees of freedom of the partition function, but providing much deeper insight into the system. A familiar example is the duality between the low and high temperature expansions of the 2D Ising model which is captured by their mapping to the same ensemble of loop configurations [9]. Loop models appear more directly in the study of polymer chains and self avoiding walks. In general the partition function of loop models have the form [10]

$$Z = \sum_{\mathcal{L}} w(\mathcal{L}) t^{L(\mathcal{L})} \quad (1.1)$$

where \mathcal{L} denotes a single loop configuration on a lattice, $L(\mathcal{L})$ is the total length of all the loops in \mathcal{L} and $w(\mathcal{L})$ is the weight assigned to a single loop configuration which may depend on the topological properties of the configuration \mathcal{L} . The loop configurations \mathcal{L} on a lattice could be divided in different categories depending on whether the loops intersect or not, if every site of the lattice is visited by a loop or not (these are called fully-packed loop models) and sometimes the loops could be assigned a 'colour' degree of freedom. For example, the most widely studied class of loop models called $O(n)$ loop models [11] have $w(\mathcal{L}) = n^{\mathcal{N}}$ where \mathcal{N} is the number of loops in a configuration \mathcal{L} and n is the loop fugacity.

More importantly, loop models are widely used to study critical phenomena - Fig.1.1 shows loops acting as boundaries of percolating clusters of Ising spins at the critical point. Due to their critical nature these models could be studied using analytical tools

for critical phenomena such as the Coulomb Gas formalism [12], conformal field theory and Schramm-Loewner evolution [13].

As we will see in chapter 5, loop models are intrinsically linked to another class of constrained models called vertex models. The most well known of these is the six-vertex model [14, 15], finding itself the center of attention in numerous models of statistical physics and condensed matter physics. In its early stages the six-vertex model was used to understand the entropy of water ice (this class of models are also called ice-models) and phase transitions in ferroelectrics. Lieb solved the partition function exactly using Bethe ansatz methods for a special case which assigned equal weights to all the six vertex configurations, Baxter later gave an exact solution in any general case using what is now known as the Yang-Baxter equation [16].

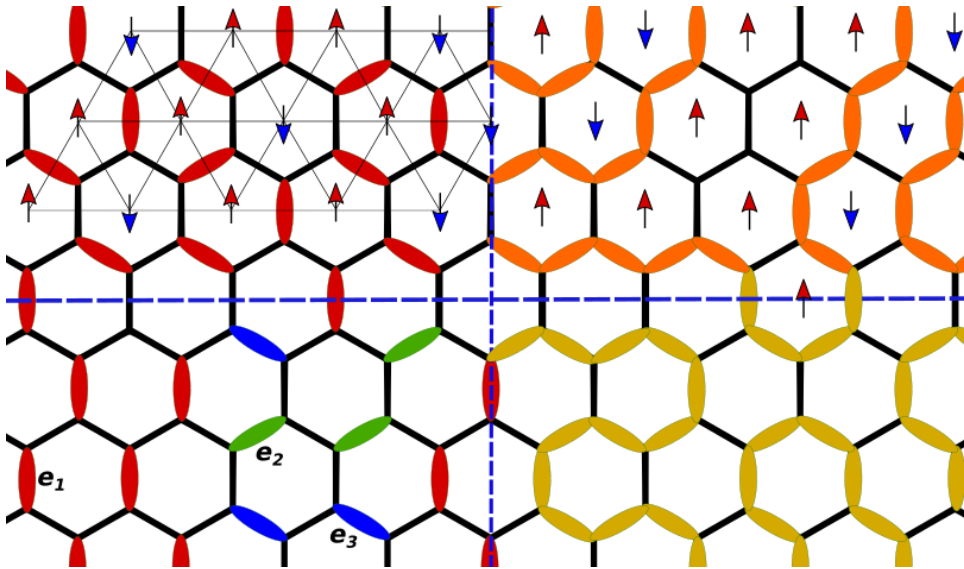


Figure 1.1: Top left : Mapping the ground states of antiferromagnetic Ising model on the triangular lattice to dimer coverings of the dual hexagonal lattice. A dimer is assigned to the bond which crosses the link of two up or two down spins. Bottom left : dimers represent diatomic molecules on a hexagonal crystal surface. Three different orientations of dimers are assigned different fugacities. Top right : Boundary of domain wall of spins seen as a loop. Here the loop model is incompletely-packed since some lattices sites have no loops passing through them. Bottom right : A fully-packed loop configuration on the hexagonal lattice.

Constrained models on Rydberg atom simulators

The advancement in technology to laser trap individual atoms on optical lattices has led to a recent surge in realising quantum many-body Hamiltonians on programmable quantum simulators [17]. This harkens back to the idea proposed by Richard Feynmann to use a quantum system to solve a quantum problem [18].

Rydberg states are atomic states with a large principal quantum number n . Such states

have long lifetimes which scale as n^3 , because of this one can essentially treat a Rydberg atom as a two level system with a ground state $|g\rangle$ and an excited state $|r\rangle$ called a Rydberg state. For two Rydberg atoms separated by a distance R , simultaneous excitations to the Rydberg state $|rr\rangle$ have an energy cost which goes as $\Delta E = C_6/R^6$. This implies that within a certain critical distance $R_b = (C_6/\hbar\Omega)^{1/6}$ called the *blockade radius* [19], one cannot have simultaneous excitations of two Rydberg atoms. Ω here is the Rabi oscillation frequency introduced by the laser trap.

Consider the following Hamiltonian for Rydberg atoms trapped on an optical lattice,

$$H_{Rydberg} = \sum_{i=1}^N \frac{\Omega}{2} (|g\rangle_i \langle r| + |r\rangle_i \langle g|) - \delta |r\rangle_i \langle r| + \frac{1}{2} \sum_{(i,j)} V(|\mathbf{r}_i - \mathbf{r}_j|/a) |r\rangle_i \langle r| \otimes |r\rangle_j \langle r| \quad (1.2)$$

The parameters Ω and δ are the Rabi oscillation frequency and the detuning of the coherent laser field. The potential $V(x) = C_6/x^6$ is the Van der Waals interaction between two Rydberg atoms. a here is the lattice spacing. As mentioned before there is a blockade radius R_b which depends on Ω , such that there cannot be simultaneous excitations of two Rydberg atoms within this radius. One has a control over the range of this blockade by just changing the lattice spacing a .

We can see that for very large and negative δ/Ω it is energetically favourable for all atoms to be in the ground state $|g\rangle$. For large positive δ/Ω all atoms are in the excited state but Rydberg blockade now introduces constraints on how many could be simultaneously excited. This leads to certain Rydberg *crystalline orderings* depending on the range of the blockade, which can be controlled by the ratio R_b/a [20].

Consider now an array of Rydberg atoms on a Kagome lattice. Ref. [20] shows that in the limit of large detuning, Eq.(1.2) could be approximated by a model of hard-core bosons on the Kagome lattice. Using this mapping one can identify the Rydberg crystalline orderings to dimer and loop like orderings on the triangular lattice constructed by connecting the centers of Kagome hexagons, see Fig.1.2.

Now consider the Rydberg atoms to sit on the links of the Kagome lattice. If we associate a dimer to an excited Rydberg atom on that link (see Fig.1.3), the authors of Ref. [21] show that they are able to prepare with high fidelity an equal superposition of dimer coverings of the Kagome lattice for 219 Rydberg atoms. Since such a state is a quantum spin liquid they also probe its various topological excitations.

Very recent works have proposed realising dimer models on square and triangular lattices [22], even different types of constraints like trimers showing \mathbb{Z}_3 topological order have been proposed in Rydberg atom arrays [23].

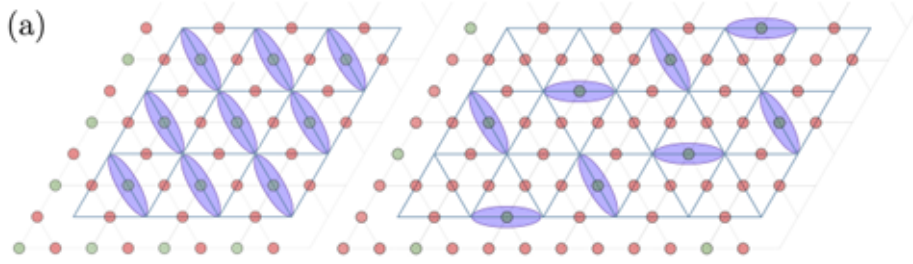


Figure 1.2: Rydberg atoms on the Kagome lattice. Every excited atom (shown in green) is placed with a dimer on the corresponding link of the triangular lattice. The left picture shows a Nematic loop like state while the picture on the right shows a staggered arrangement of dimers. The picture is taken from [20].

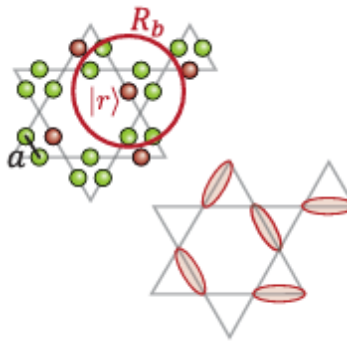


Figure 1.3: Rydberg atoms on the links of Kagome lattice. The red atoms are in the excited state $|r\rangle$, and within the blockade radius R_b all the green atoms are in the ground state $|g\rangle$. A dimer represents an excited atom. The figure is taken from [21].

Rydberg atom arrays allow to probe a quite different phenomenon of quantum many-body physics, namely the possibility to escape thermalization (ergodicity breaking). Here again constraints play a crucial role. One landmark experiment which observed the phenomenon of ergodicity breaking, used trapped Rydberg atoms on chains up to sizes of 51 atoms [24]. The blockade was tuned such that no two nearest atoms could be in the excited state at the same time. This basically formed a constrained Hilbert space in which states like, $|\dots rrr \dots\rangle$ are energetically forbidden. By performing a quench experiment, the authors observe that, starting from a Néel like initial state, $Z_2 = |rgrgrg\dots\rangle$, the system oscillates with time between Z_2 and its flipped counterpart i.e $|grgrgr\dots\rangle$. This revival behaviour, usually seen for a single spin precession in a magnetic field, is surprising for a quantum many-body system.

The paradigmatic constrained model which was able to explain the above revivals and also capture various mechanisms which could lead to weak ergodicity breaking is the PXP model [25]. The model is a 1D chain of two level Rydberg atoms like before with the following Hamiltonian

$$H_{PXP} = \sum_i P_{i-1} \sigma_i^x P_{i+1} \quad (1.3)$$

where, $\sigma_i^x \equiv |g_i\rangle\langle r_i| + |r_i\rangle\langle g_i|$ and $P_i \equiv |g_i\rangle\langle g_i|$ projects to the ground state on the neighbouring atoms. As one can see, the Hamiltonian essentially imposes the constraint of no two neighbouring atoms being in the excited state. Numerical simulations of quench dynamics on the PXP model show the revival behaviour not only for the Z_2 initial state but also for $Z_3 = |rggrggr\dots\rangle$ [26]. The model also hosts some special outlying eigenstates which show a logarithmic scaling of entanglement entropy [26], a characteristic of weak ergodicity breaking.

Plan of the thesis

- *Chapter 2* : We briefly review the important results pertaining to the Quantum dimer model on the square lattice. In addition, we recap the phase diagram of the classical interacting dimer model. The chapter also briefly describes the construction of a coarse-grained field theory through a height mapping and characterizing the critical dimer phase using Coulomb-gas methods.
- *Chapter 3* : Chapter 3 describes the Monte Carlo algorithms which will be used to obtain the phase diagrams in Chapters 4 and 5. These include the Directed Loop algorithm, to be used in classical Monte Carlo simulations of chapter 4, and the Sweeping Cluster Algorithm (SCA), which is a Quantum Monte Carlo scheme designed specifically to handle hard-core constraints. We also show how to supplement the SCA with a classical directed loop move to render it ergodic at finite temperature.
- *Chapter 4* : In this chapter we present the finite temperature phase diagram of the Quantum Dimer Model on the square lattice obtained numerically using QMC simulations. We characterize the high temperature critical phase with the Coulomb gas constant which is calculated from the fluctuations of the topological invariant (winding numbers) and various correlation functions. Finally, we try to explain the variation of the Coulomb gas constant in the high temperature critical phase using a high temperature expansion argument. The results in this chapter are based on the publication : **Bhupen Dabholkar, G. J. Sreejith, and Fabien Alet. "Reentrance effect in the high-temperature critical phase of the quantum dimer model on the square lattice". *Phys. Rev. B* 106, 205121 – Published 14 November 2022**
- *Chapter 5* : In this chapter we study a classical statistical mechanics model of fully-packed non-intersecting loops on the square lattice with attractive interaction between loop segments. We present its finite temperature phase diagram using classical Monte Carlo simulations. We show the model hosts a high temperature critical phase with a Kosterlitz-Thouless type phase transition to a low temperature

nematic phase of loops. We estimate the transition temperature with two complementary approaches : i) collapse of the susceptibility of nematic order parameter and ii) scaling of the fluctuations of winding numbers near the transition temperature. This is followed by a detailed study of various correlation functions to extract the variation of the Coulomb gas constant in the critical phase. The results in this chapter are based on the following publication : **Bhupen Dabholkar, Xiaoxue Ran, Junchen Rong, Zheng Yan, G. J. Sreejith, Zi Yang Meng, and Fabien Alet. "Classical fully packed loop model with attractive interactions on the square lattice". *Phys. Rev. B* 108, 125112 – Published 6 September 2023**

- *Chapter 6* : The final chapter of the thesis changes topics to exploring thermalization in a disordered $SU(3)$ symmetric spin chain. We begin by recalling the important concepts of thermalization for an isolated quantum many body system. These include the Eigenstate Thermalization Hypothesis, its connection to Random Matrix theory and Many Body Localization. We also recall the commonly used probes in numerics to signal thermalization and its breakdown. Since our exact diagonalization utilizes the full $SU(3)$ symmetry of the model, we describe the construction of a $SU(N)$ symmetric Hamiltonian in an orthogonal basis of Young tableau. The use of this non-abelian symmetry results in a constrained Hilbert space, making connection with the general theme of the thesis. Finally, we present our exact diagonalization results for the model. We show that the model exhibits a non-ergodic regime over a broad range of system sizes for strong enough disorder, contrasting with the rapid thermalization observed at weak disorder. This chapter is based on the pre-print : **Bhupen Dabholkar, Fabien Alet. "Ergodic and non-ergodic properties of disordered $SU(3)$ chains". *arXiv.2403.00442***

Chapter 2

Quantum Dimer model on the square lattice

In this chapter we briefly review some aspects of the Rokhsar-Kivelson Quantum dimer model (QDM), focusing on its construction on the square lattice. Since our main objective is to study its finite temperature phase diagram we also review in this chapter some important results on the classical interacting dimer model (CIDM).

2.1 Quantum dimer model on the square lattice

The Quantum Dimer model was originally introduced by Rokhsar and Kivelson as a minimal model in the study of high-Tc superconductivity [8]. In the original paper the dimers represent $SU(2)$ singlets of spins ($\frac{|\uparrow_i\downarrow_j\rangle - |\downarrow_i\uparrow_j\rangle}{\sqrt{2}}$) sitting at two (neighbouring) sites i and j . Hence these dimers represent singlet Cooper pairs and the Hamiltonian describes quantum dynamics of a Cooper pair dominated phase. However, RK type Hamiltonians have found their use much beyond their original motivation, they are shown to host various exotic phases with topological order, unusual excitations and deconfined critical points [27].

The Hilbert space consists of closed packed dimer coverings of a lattice (fig. 2.1). We will enforce by construction an orthonormal basis $\{|\psi_i\rangle\}_{\mathcal{N}}$ such that each $|\psi_i\rangle$ represents a dimer covering and \mathcal{N} is the total number of dimer coverings of the lattice. One must note that the dimers here do **not** represent $SU(2)$ spin singlets, in such a case the dimer coverings are not orthonormal (see section 1.10 in [28]). The RK Hamiltonian is defined on a square lattice as :

$$H_{QDM} = \sum_{\square} -t (|\square\rangle\langle\square| + |\square\rangle\langle\square|) + V (|\square\rangle\langle\square| + |\square\rangle\langle\square|) \quad (2.1)$$

where the summation is over all plaquettes of the square lattice. The Hamiltonian consists of the following two terms,

- *Kinetic term* : this is the *off-diagonal* part of H_{QDM} with coupling t which flips two parallel dimers on a plaquette.
- *Potential term* : this is the *diagonal* part of H_{QDM} with coupling V which counts the number of flippable plaquettes.

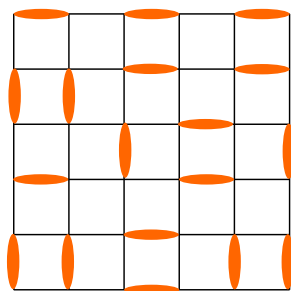


Figure 2.1: A fully packed dimer covering of the square lattice.

2.1.1 Topological invariants

If we put the dimer configurations of the square lattice on a torus, we can construct quantities which are invariant under the action of H_{QDM} . Consider a reference line in the x (y) direction crossing vertical (horizontal) dimers. Due to the bipartite nature of the lattice we can assign a direction on each link of the square lattice such that it points from sites of sublattice A to those of sublattice B (or vice-versa), see Fig. 2.3a. We then count N_A as the number of dimers on links pointing upwards (right) in the positive y (x) direction and N_B the number of dimers on links pointing downwards (left) in the negative y (x) direction, crossing the reference line. Then one can observe that any local rearrangements of dimers (such as the plaquette flip kinetic term of H_{QDM}) leaves $N_A - N_B$ unchanged. The only way to change this quantity is by making a *non-local* move, this involves rearranging dimers along a closed loop which winds around the toroidal directions, see Fig. 2.3a. As one can see, such invariant quantities heavily depend on the topology of the surface considered, namely here on periodic boundary conditions. Such *topological invariants* are called *Winding numbers*. For a square lattice (or any bipartite lattice) on a torus, we can define two such winding numbers (W_x, W_y) by measuring $N_A - N_B$ in the two directions. Note that this invariant does not depend on where the reference line

is chosen. By *labelling* each dimer covering or state $|\psi_i\rangle$ by such winding numbers we can divide all the configurations in *topological sectors* with each sector labelled by two winding numbers (W_x, W_y) . Since H_{QDM} only has local dimer rearranging terms (kinetic term), $\langle\psi_i|H_{QDM}|\psi_j\rangle = 0$ for any $|\psi_i\rangle, |\psi_j\rangle$ belonging to different topological sectors. We can therefore view H_{QDM} in a block-diagonal form with every block labelled by its winding numbers, see Fig. 2.3b.

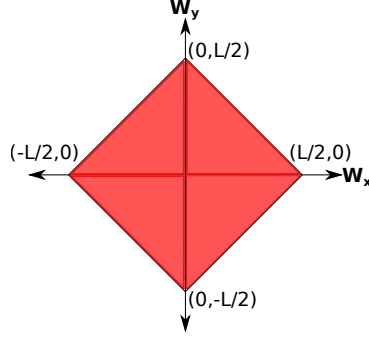


Figure 2.2: The values of the winding numbers lie within a Rhombus - $|W_x| + |W_y| = L/2$, where L is the linear length of the square lattice.

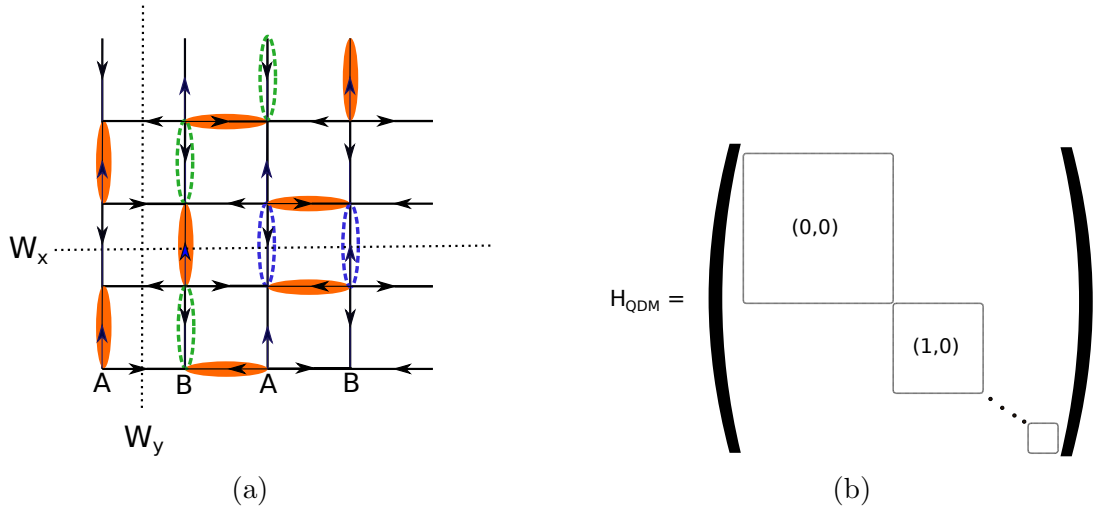


Figure 2.3: (a) shows an example of assigning winding numbers (W_x, W_y) on the square lattice. In this particular example, the configuration formed by the orange coloured dimers belongs to the winding sector $(1, 0)$. The figure also demonstrates the action of a local and a non-local move. As one can see, the dimer configuration after the local move (shown by the blue dashed dimers) has the same winding sector while that after a non-local move (shown by the green dashed dimers) changes the winding sector to $(0, 0)$. (b) shows the structure of H_{QDM} in its block-diagonal form, with each block labelled by its two winding numbers.

2.1.2 Monomers

We define a *monomer* at a lattice site when the site is not touched by a dimer, this implies that we have broken the hardcore constraint on that particular site. Removing a dimer on a bond leaves behind two monomers on the neighbouring sites, see Fig. 2.4. By moving the neighbouring dimers one can also separate the two monomers. What do these monomers physically mean? If we consider the picture where the dimers represent $SU(2)$ spin singlets, these monomers represent *fractionalized* spin-1/2 excitations (spinons) which may propagate independently. For some other effective models, one can also consider a case where the fractionalization [29] occurs such that one of the electrons carries spin 1/2 (spinon) leaving the other monomer representing a charged spinless quasiparticle called a holon, this is known as spin-charge separation [30]. The above two examples show how abstract objects like dimers and monomers could capture a real physical phenomenon of fractionalization.

Note that the Hilbert space of the QDM does not allow for monomers directly, but for the sake of understanding the phases of matter, we can insert two test monomers and test their confinement properties in the sea of dimers. Indeed, an important property of the QDM is whether it allows two monomers to be *deconfined*, i.e they could be separated to large distances with a finite energy cost. On the square lattice, this is the case only when $V = t$ in Eq. 2.1, we will come back to this point in the next section when discussing the ground state phase diagram.

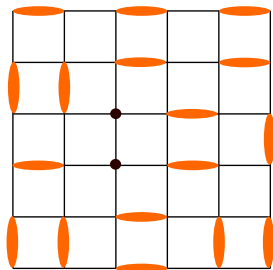


Figure 2.4: Removing a dimer creates two *monomers* shown by black dots

2.1.3 Ground state phase diagram on the square lattice

In this subsection we will review the possible ground state phases permitted by H_{QDM} on the square lattice. Since these phases arise as a competition between the potential and the kinetic term in H_{QDM} , we will explore the different phases by varying the ratio

V/t in Eq. 2.1.

Columnar Phase

In the limit $V/t \rightarrow -\infty$, it becomes energetically favourable from Eq. 2.1 to form dimer configurations of plaquettes with parallel dimers, as shown in Fig. 2.5. This is called the columnar phase. This phase breaks the $\pi/2$ rotation symmetry and the translation symmetry by one lattice spacing along the direction of the dimers. Even though the columnar state is an eigenstate of Eq. 2.1 only in the classical limit ($V/t \rightarrow -\infty$), it will survive quantum fluctuations and persist as a ground state order up to some $V/t = (V/t)_c < 1$. The 4 columnar configurations lie in the $(0, 0)$ winding sector.

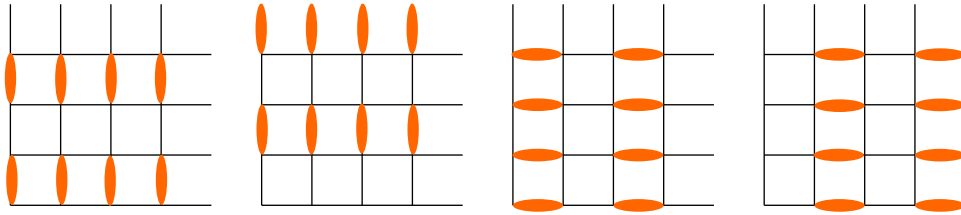


Figure 2.5: 4 degenerate columnar configurations

Staggered Phase

In the opposite limit of $V/t \rightarrow \infty$, it is energetically favourable for the system to have no *flippable* plaquettes, as shown in Fig. 2.6. We call this the staggered phase. It is easy to see that the staggered states would be ground states of H_{QDM} for any $V/t > 1$ since they are zero energy eigenstates and Eq. 2.1 is positive semi-definite for $V/t > 1$. All the staggered states have maximal winding numbers. As opposed to the columnar phase, at least on the square lattice, the degeneracy of the staggered configurations is subextensive (the number of configurations go like $2^{L/2}$ [31]).

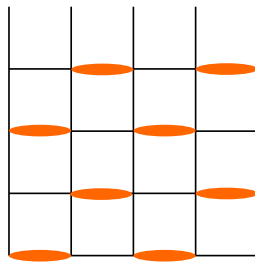


Figure 2.6: Example of a staggered configuration with no parallel dimers

Plaquette and Mixed phases

Consider the cartoon shown in Fig. 2.7, here the coloured bonds indicate a higher probability of dimer occupancy than the uncoloured bonds. We call this the *Plaquette* state.

One way to represent such a state is

$$|\psi_{plaq}\rangle = \bigotimes_{i \in \mathcal{A}} \frac{1}{\sqrt{2}} (|\text{horizontal dimer}\rangle_i + |\text{vertical dimer}\rangle_i) \quad (2.2)$$

where we have a resonating dimer state on every plaquette of one of the sublattices. The plaquette state is symmetric under $\pi/2$ rotations and has a translation symmetry of two lattice spacings in both directions. One can also see that it is 4-fold degenerate.

An additional possible phase was proposed to exist [32], called the *mixed phase*. We can represent such a mixed state by considering Eq. 2.2 but with different probabilities for the vertical and horizontal bonds. This phase could be viewed as a mixture of columnar and plaquette phases, since it breaks the $\pi/2$ rotation symmetry like the columnar phase and also breaks the translation symmetry to two lattice spacings in both directions like the plaquette phase. Note that both the plaquette and mixed phases correspond to the $(0, 0)$ winding sector.

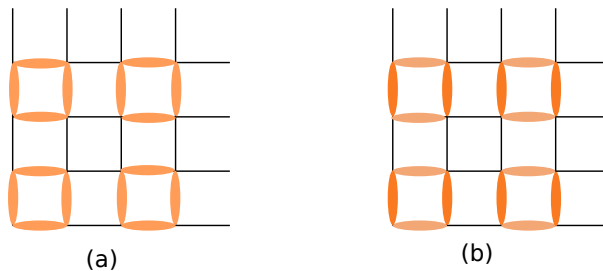


Figure 2.7: (a) shows a plaquette state with equal probabilities for horizontal and vertical dimers. (b) shows a mixed state where the probabilities are different.

The Rokhsar-Kivelson point

When $V = t$ in Eq. 2.1, and fixing the winding sector, the ground state of H_{QDM} is exactly given by

$$|\psi_{GS}\rangle = \frac{1}{\sqrt{\mathcal{N}}} \sum_{c \in \{(W_x, W_y)\}} |c\rangle \quad (2.3)$$

here the summation is over all the dimer coverings c within a particular winding sector and \mathcal{N} is the number of such coverings. Eq. 2.3 shows that the ground state is an equal amplitude superposition of all possible dimer coverings within a topological sector. Due to the block-diagonal structure of Eq. 2.1, every topological sector has a unique ground state given by Eq. 2.3 and all of them are degenerate with zero energy. For the staggered states, there is an anomaly degeneracy for configurations lying on the edges of the rhombus shown in Fig. 2.2. Unlike the four vertices of the rhombus where there is only one staggered configuration corresponding to each corner, there are multiple staggered configurations corresponding to each winding sector on the edge of the rhombus [33].

The physics at the RK point depends on the nature of the lattice. For the square lattice (and most bipartite lattices) the RK point is a quantum critical point separating two crystalline phases. For non-bipartite lattices in two dimensions and higher, for example the triangular lattice and the fcc lattice, the RK point is part of a Z_2 *RVB Liquid phase* which has topological order [34].

To understand the nature of monomer excitations at the RK point, imagine first that we insert two monomers in a fully columnar state. We can see that as one separates the monomers along a line it breaks more and more columnar plaquettes costing us more energy. Hence one can say that in the columnar phase the monomers are linearly confined. However, this is not the case at the RK point because it is a superposition of all the dimer coverings, which is not a long range ordered state. Hence at the RK point, separating two monomers to large distances only costs a finite energy and they are algebraically deconfined. Because of this the RK point is called a *deconfined critical point*. As for its critical nature, this will be explained in later sections on the Classical dimer model.

The ground state phase diagram of the QDM on the square lattice has gone through many revisions over the years. The model has proved to be a numerical challenge with each revision tackling the problem with new and improved numerical techniques to push the system sizes further. We will briefly recap the proposed phase diagrams over the years and its present status.

The earliest studies which went beyond the lattice sizes accessible to exact diagonalization [35] used projection based Quantum Monte Carlo [36]. From their simulations up to lattice sizes of $L = 48$ they concluded on a phase transition from the columnar phase to a plaquette phase for some $V/t \simeq 0.6$. A further study based on the energy spectrum analysis using Green's function Monte Carlo and ED [32] concluded that there exists an intervening mixed phase starting at $V \simeq 0$ which continuously interpolates between the columnar phase and the RK point. Due to the difficulty in resolving the energy spectrum gaps near the RK point (due to its highly degenerate nature) one cannot absolutely rule out a transition out of the mixed to the plaquette phase very close to the RK point. The authors therefore propose an interesting scenario where the mixed phase interpolates continuously between the columnar and plaquette states. Another study [37] highlights the existence of a (pseudo) $U(1)$ symmetry near $V \lesssim t$, rendering the finite-size analysis difficult near the RK point. The most recent numerics performed on this model using the Sweeping Cluster quantum Monte Carlo [38] puts forward a different picture where the mixed phase extends much beyond the RK point for $V < 0$. In this study the authors rely on an analysis of the distribution of the columnar order parameter but the signals for a mixed phase are very weak.

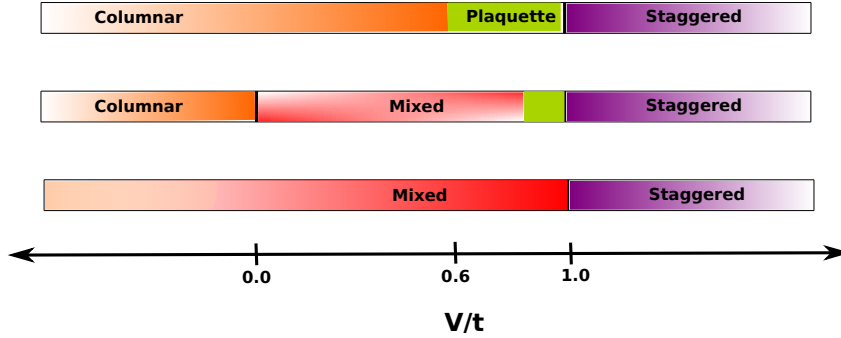




Figure 2.8: Various revisions of the ground state phase diagram of the QDM over the years. Top : [36], middle : [32], bottom : [38]

2.1.4 Perspectives on other phases

H_{QDM} could be formulated on various other lattices and geometries, giving rise to a plethora of exotic phases. Similar to the phase diagram presented above for the square lattice, other 2d bipartite lattices like the honeycomb lattice [39] are also shown to host similar columnar (called the "star" phase for the honeycomb lattice), plaquette and staggered phases. The RK point is also a quantum critical point separating two crystalline orders - the plaquette phase and the staggered phase. The situation for bipartite lattices in 3 dimensions (for example cubic and diamond lattice) and higher is however different. Here the RK point is part of an extended $U(1)$ liquid phase (also called the *Coulomb phase*) [6, 40, 41, 42, 43]. This phase is gapless with dipolar dimer correlations. For 2d non-bipartite lattices like the triangular [44, 34] and the Kagome lattice [45, 46], the RK point is part of a Z_2 RVB liquid phase. The Z_2 RVB liquid is gapped and has exponentially correlated dimers. This phase could be extended for non-bipartite lattices in 3d and higher, for example the fcc lattice.

2.2 Brief review of the Classical Interacting Dimer Model on the square lattice

Our objective in this chapter is to understand how the previously described crystalline ground states of the QDM on the square lattice melt when we introduce thermal fluctuations. In light of the equivalence between quantum models at finite temperature and its classical equivalent, we review in this section some important results of the Classical Interacting Dimer Model (CIDM) [47, 48, 49, 50, 31].

Let us begin by defining the partition function for the CIDM. To every plaquette of the square lattice we assign an energy V if it has two parallel dimers ( or ) and the

energy is zero otherwise. The partition function is given by

$$Z = \sum_c e^{-\beta E_c} \tag{2.4}$$

$$E_c = V(N(\text{⏏}) + N(\text{⏏}))$$

where $N(\text{⏏}) + N(\text{⏏})$ counts the total number of parallel plaquettes in a dimer covering c and the summation is taken over all such dimer coverings. The sign of V determines the different ordered states. If $V < 0$, it is energetically favourable to have parallel dimers on a plaquette hence at low temperature it will lead to a **columnar** ordering (Fig. 2.5). This 4 fold degenerate ordered state spontaneously breaks translation and $\pi/2$ rotation symmetries. If $V > 0$, it now costs energy to have parallel plaquettes which at low temperature leads to **staggered** like ordering (Fig. 2.6) where there are no parallel dimers on any plaquette. The smallest excitations out of the columnar phase are plaquette flips of parallel dimers which cost an energy of $2V$ (they break two neighbouring plaquettes), while the excitations out of the staggered phase involve switching dimers along a loop which winds in one of the toroidal directions and this excitation costs an energy of LV . Since excitations out of both these states are gapped we expect them to persist to some finite temperature.

In the non interacting limit $T = \infty$ ($\beta = 0$), the above partition function Eq. 2.4 is the unweighted sum of all the dimer coverings on the square lattice which is exactly solvable [51, 52]. In this case it was shown that the dimers are **critical**, meaning the dimer-dimer correlations decay algebraically with distance. Specifically for the square lattice it can be shown exactly that the leading term in the correlation function decays as $1/r^2$. This is in contrast with interacting spin models where at $T = \infty$ it is always a paramagnet i.e completely uncorrelated spin configurations.

2.2.1 Phase Diagram of CIDM

The phase diagram of CIDM is quite well studied and understood [47, 48], we will briefly recount it here. At high temperature there is a critical phase where the leading term of the dimer-dimer correlation function decays algebraically with distance as $1/r^\alpha$ and the exponent α varies with temperature. We know from exact results that $\alpha(T = \infty) = 2$. For *attractive* interactions ($V < 0$) set to $V = -1$ without loss of generality, there is a Kosterlitz Thouless phase transition to the 4 fold degenerate columnar states at $T \sim 0.65$. As we will see in the next subsections, this phase transition can be well understood by a Sine-Gordon type action which also explains the variation of the exponent α with temperature. We will see in particular that $\alpha(T = T_{KT}) = 1/4$. For *repulsive* interactions

($V > 0$), there is a continuous phase transition to staggered orderings [31]. This has only been shown through numerics and so far there is no theoretical account of this phase transition.

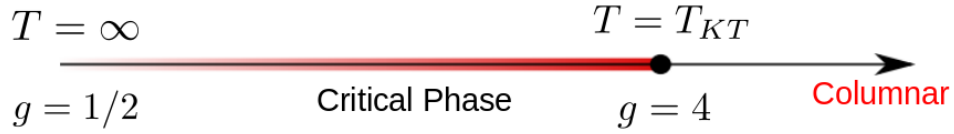


Figure 2.9: Phase diagram of the CIDM for attractive interactions $V < 0$. Here $g = 1/\alpha$ is called the Coulomb Gas constant. The phase diagram shows the limiting values of g at $T = \infty$ and $T_{KT} \sim 0.65$ where there is a Kosterlitz-Thouless phase transition from the critical phase to a columnar phase.

2.2.2 Height Mapping

We begin by constructing a continuum description of the dimer coverings using a procedure called height mapping [53]. We focus on the case of a square lattice but such a construction is quite general for bipartite lattices. Let us assign a real valued *height* z to each plaquette of the square lattice according to the following rule - going counterclockwise around sublattice A (for sublattice B), the height z changes by $+3/4$ if it encounters a dimer and by $-1/4$ if it encounters an empty link ($-3/4$ and $+1/4$ respectively). By choosing a reference plaquette with $z = 0$ one can assign a unique height configuration to every dimer configuration. In the thermodynamic limit one can assign a continuous height function $h(r)$ by averaging the heights z from all the dimer coverings.

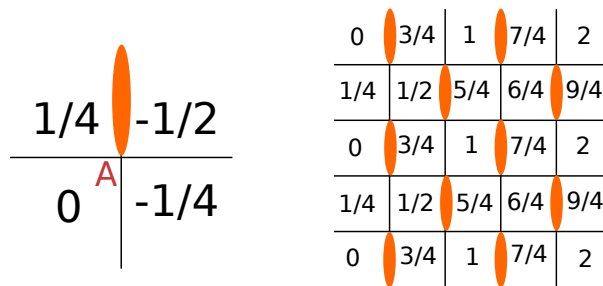


Figure 2.10: Example of height mapping. Figure on the left illustrates the height rule around sublattice A. The heights are assigned with the bottom left plaquette set as reference with height $z = 0$ and assigning the heights counterclockwise with the rule $-1/4$ for no dimer and $+3/4$ if a dimer is encountered. The figure on the right illustrates a height mapping for a staggered dimer covering.

2.2.3 Action for the high temperature phase

The next task is to construct an action $S[h(r)]$ for the height field we described in the previous subsection. One can show (see [47] for a detailed argument) that a translation by one lattice spacing of a dimer configuration makes $h(r) \rightarrow h(r) + 1/4$ and a rotation by $\pi/2$ makes $h(r) \rightarrow -h(r)$ for all r . We want our action to be invariant under rotation and translation hence we must ensure that $S[h(r)] = S[h(r) + 1/4]$ and $S[h(r)] = S[-h(r)]$. The simplest action one can construct with these symmetries is

$$S = \int d^2r [\pi g (\nabla h(r))^2 + \sum_{p=4,8,\dots} V_p \cos(2\pi p h(r))] \quad (2.5)$$

where g is called the Coulomb gas constant. For $p = 4$ the cosine term has 4 minima $h = 1/8, 3/8, 5/8, 7/8$ which correspond to the 4 columnar dimer configurations and $V_4 > 0$. The gradient term favours dimer configurations with 'flat' heights and the cosine term is responsible for selecting from these 'flat' configurations the 4 columnar states. The above action therefore describes the interplay between energy and entropic selection. The above action is quite well known as the 2D Sine-Gordon model which describes a KT transition between two phases. Renormalization Group arguments [54] shows that when $g < p^2/4$ the cosine term is irrelevant and the action is now given only by the gaussian term which describes the critical phase on the other hand when $g > p^2/4$ the cosine term becomes relevant and it describes the 'height locked' columnar ordered phase.

We briefly digress here back to the RK point of the QDM. One can notice from Eq. 2.3 that the normalization factor \mathcal{N} which counts the total number of dimer coverings on the square lattice is nothing but the partition function of the **non-interacting** classical dimer model (or the CIDM at $T = \infty$). This 'classical' nature of the RK point is what makes it critical as we just saw how the dimers in the non-interacting limit have power law correlations.

2.2.4 Coulomb Gas Construction

Coulomb gas methods form a general framework to extract critical exponents in such constrained models which are amenable to the height mapping [12, 55]. The vertex operators $\exp(2\pi i e h(r))$ correspond to an electric charge e in the Coulomb Gas picture. From the continuum description of the dimer density operator (see Eq. 2.6 below) we can see that it corresponds to an electric charge $e = 1$ while the cosine term in the Sine Gordon action Eq. 2.5 corresponds to an electric charge $e = 4$. The monomers in our model would correspond to a dual magnetic charge $m = 1$. In the Coulomb

Gas description the exponent of an electromagnetic charge is $\alpha(e, m) = e^2/g + gm^2$ with the scaling dimension $\alpha(e, m)/2$. From this we could infer that, the dimer-dimer correlations would decay with the exponent $\alpha(1, 0) = 1/g$ while the monomer-monomer correlations would decay with the exponent $\alpha(0, 1) = g$. Since the cosine term has the scaling dimension $\alpha(4, 0)/2 = 8/g$, it will become relevant when $g \geq 4$.

2.2.5 The Dimer Correlators

As we saw in the previous section the Coulomb gas constant g is the characteristic quantity for describing the critical dimer phase at high temperature. One of the ways of measuring g is to directly calculate the dimer-dimer correlators $\langle n(\mathbf{0})n(\mathbf{r}) \rangle$ here $\mathbf{r} = (\mathbf{x}, \mathbf{y})$. One can build two kinds of such correlators : *Longitudinal* correlators, $\langle n_{\mathbf{-}}(\mathbf{0})n_{\mathbf{-}}(x, 0) \rangle$ and $\langle n_{\mathbf{I}}(\mathbf{0})n_{\mathbf{I}}(0, y) \rangle$ and *Transverse* correlators, $\langle n_{\mathbf{-}}(\mathbf{0})n_{\mathbf{-}}(0, y) \rangle$ and $\langle n_{\mathbf{I}}(\mathbf{0})n_{\mathbf{I}}(x, 0) \rangle$. Here $n_{\mathbf{-}}(\mathbf{r}) = 1$ if there is a horizontal dimer at site \mathbf{r} and 0 if there is no dimer present, it follows similarly for the vertical dimers.

To get an idea of the forms of the leading terms in the above correlators, one needs a continuum description of the above dimer number operators. These are given by [49, 56]:

$$\begin{aligned} n_{\mathbf{-}} - 1/4 &= (-1)^{x+y} \nabla_y h + \frac{1}{2} [(-1)^x \exp(2\pi i h) + h.c] \\ n_{\mathbf{I}} - 1/4 &= (-1)^{x+y+1} \nabla_x h + \frac{1}{2} [i(-1)^y \exp(2\pi i h) + h.c] \end{aligned} \quad (2.6)$$

Since in the critical phase the action S in Eq. 2.5 is just the *free boson* conformal field theory with only the gradient term, there are two kinds of leading contributions to the above correlators - a *dipolar* contribution which comes from the correlator of the derivatives of the height field, for example $\langle \nabla_x h(0) \nabla_x h(r) \rangle \sim 1/r^2$ and a contribution from the correlator of the vertex operators $\langle e^{2\pi i h(0)} e^{-2\pi i h(r)} \rangle \sim 1/r^{1/g}$. We will take a closer look at these correlations later in the Quantum dimer model.

2.2.6 Fluctuations of Winding Numbers

In our statistical ensemble of dimer coverings let us denote $P(W_x, W_y)$ as the probability of a dimer covering to have winding numbers W_x, W_y . By relating the winding numbers to the height field, $h(x, y) = x \frac{W_x}{L_x} + y \frac{W_y}{L_y}$, one can find $P(W_x, W_y)$ in the critical phase is given by [48]

$$P(W_x, W_y) = \frac{e^{-\pi g((W_x/L_x)^2 + (W_y/L_y)^2)L_x L_y}}{\sum_{n, m \in \mathbb{Z}} e^{-\pi g((n/L_x)^2 + (m/L_y)^2)L_x L_y}} \quad (2.7)$$

The quadratic fluctuations of the winding number, say along x are given by

$$\langle W_x^2 \rangle = \frac{\sum_{n \in \mathbb{Z}} n^2 e^{-\pi g n^2 (L_y/L_x)}}{\sum_{n \in \mathbb{Z}} e^{-\pi g n^2 (L_y/L_x)}} \quad (2.8)$$

This is an important relation as it relates the Coulomb Gas constant g to the fluctuations of winding number - an observable which we can easily measure in a simulation.

Chapter 3

Monte Carlo methods for Constrained models

This chapter focuses on the classical and quantum Monte Carlo simulations to be used in chapter 4 and chapter 5. We begin in section 3.1 with basics of classical Monte Carlo, the goal here is to quickly introduce the terminology and concepts to be used later in the chapter when detailing the algorithms. Section 3.2 describes the directed loop Monte Carlo algorithm formulated for a dimer and loop constraint on the square lattice. We change gears in section 3.3 to Quantum Monte Carlo (QMC) simulations, more specifically we briefly review the basic framework of Stochastic Series Expansions (SSE). This is followed, in section 3.4, by a detailed description of the recently developed sweeping cluster algorithm (SCA) designed specifically to handle quantum constrained models. We end the chapter in section 3.5 with our own addition to the SCA which enables sampling different topological sectors of the QDM on the square lattice.

3.1 Classical Monte Carlo

A Monte Carlo simulation involves stochastically generating configurations which follow a certain probability distribution, for example the Boltzmann distribution in statistical physics. One is generally interested in thermodynamic averages of a physical observable \mathcal{O} given by

$$\langle \mathcal{O} \rangle = \frac{\sum_x \mathcal{O}(x) e^{-\beta E(x)}}{\sum_x e^{-\beta E(x)}} \quad (3.1)$$

where $\beta = 1/T$ is the inverse of temperature T and the sum is over all the possible configurations of the system. A naive sampling of the sum would involve randomly

generating say N configurations $\{x_1, x_2, \dots, x_N\}$ and estimating the average as

$$\langle O \rangle \simeq \frac{\sum_{i=1}^N \mathcal{O}(x_i) e^{-\beta E(x_i)}}{\sum_{i=1}^N e^{-\beta E(x_i)}} \quad (3.2)$$

$E(x)$ being an extensive quantity (growing proportionally to the volume of the system) will cause issues with numerical precision in evaluating Eq. 3.2. Furthermore, random sampling will generate configurations mostly at the tail end of the distribution with small Boltzmann weights, missing most of the configurations which do actually contribute significantly to the average.

A Monte Carlo simulation thus uses *importance sampling* instead, where the configurations x_i are generated with a probability $e^{-\beta E(x_i)}$ and now the average is estimated as

$$\langle O \rangle \simeq \frac{\sum_{i=1}^N \mathcal{O}(x_i)}{N} \quad (3.3)$$

To propose new configurations in accordance with a probability distribution a Monte Carlo simulation usually relies on a *Markov Chain* process.

A Markov process is a stochastic process in which new states generated will depend only on the previous state. A Markov chain is characterised by transition probabilities $P(\mu \rightarrow \nu)$, which denotes the probability of transition from state μ to state ν . A MC simulation will generate a sequence of such states starting from some state μ such that if run long enough the states will appear with probabilities given by the Boltzmann distribution. In a Markov process time ordered sequence of configurations is generated with the probabilities governed by the following master equation

$$\frac{dW_\mu}{dt} = \sum_\nu [W_\nu(t)P(\nu \rightarrow \mu) - W_\mu(t)P(\mu \rightarrow \nu)] \quad (3.4)$$

W_μ is the probability the the system is in state μ , these are referred to as **weights**. The time t here is the 'Monte Carlo time' and the sequence of generated configurations is called a Monte Carlo time series. At equilibrium, setting the derivative in Eq. 3.4 to zero we get the condition

$$\sum_\nu W_\nu P(\nu \rightarrow \mu) = \sum_\nu W_\mu P(\mu \rightarrow \nu) \quad (3.5)$$

where we have replaced $W(t)$ with their respective equilibrium distributions. This is called a **balance condition**. One way to satisfy Eq. 3.5 is to locally satisfy the balance equations

$$W_\nu P(\nu \rightarrow \mu) = W_\mu P(\mu \rightarrow \nu) \quad (3.6)$$

This is called the condition of **detailed balance**.

As we will see later there is a lot of freedom in setting the transition probabilities. The

simplest and the most common is the Metropolis algorithm [57],

$$P(\mu \rightarrow \nu) = \min \left(1, \frac{W(\nu)}{W(\mu)} \right). \quad (3.7)$$

Another common way is the heat-bath algorithm,

$$P(\mu \rightarrow \nu) = \frac{W(\nu)}{W(\mu) + W(\nu)}. \quad (3.8)$$

Note that in both the above cases, if the equilibrium probabilities are given by the Boltzmann distribution, the transition probabilities depend only on the energy difference between the configurations μ and ν , $e^{-\beta\Delta E}$ with $\Delta E = E(\nu) - E(\mu)$.

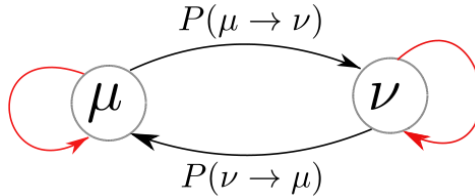


Figure 3.1: A Markov chain between two states

As will be important for the algorithm in the next section, let's say we want to reduce the processes which do not change the state, like $\mu \rightarrow \mu$ and $\nu \rightarrow \nu$ (shown in red in Fig. 3.1), called the *bounce back* processes (the name will become relevant in the context of the next section). Let us compare the average bounce back rate, $B = \frac{W(\mu)P(\mu \rightarrow \mu) + W(\nu)P(\nu \rightarrow \nu)}{W(\mu) + W(\nu)}$, between two states (μ and ν) for the Metropolis and the heat-bath algorithm. Without loss of generality, consider $W(\mu) > W(\nu)$ and define $0 < a = W(\nu)/W(\mu) < 1$. We have,

$$B = \begin{cases} \frac{1-a}{1+a}, & \text{for Metropolis algorithm} \\ \frac{1+a^2}{(1+a)^2}, & \text{for heat-bath algorithm} \end{cases} \quad (3.9)$$

which shows that between the two, the Metropolis algorithm has the lower bounce back rate.

It is common practice to split the transition probabilities into an *a priori* probability (using the terminology from [58]), $\mathcal{A}(\mu \rightarrow \nu)$ and an acceptance probability, $\mathcal{P}(\mu \rightarrow \nu)$ as

$$P(\mu \rightarrow \nu) = \mathcal{A}(\mu \rightarrow \nu)\mathcal{P}(\mu \rightarrow \nu) \quad (3.10)$$

the detailed balance condition Eq. 3.6 then becomes

$$W(\mu)\mathcal{A}(\mu \rightarrow \nu)\mathcal{P}(\mu \rightarrow \nu) = W(\nu)\mathcal{A}(\nu \rightarrow \mu)\mathcal{P}(\nu \rightarrow \mu). \quad (3.11)$$

The acceptance probability is then given by the Metropolis scheme as,

$$\mathcal{P}(\mu \rightarrow \nu) = \min \left(1, \frac{\mathcal{A}(\nu \rightarrow \mu)W(\nu)}{\mathcal{A}(\mu \rightarrow \nu)W(\mu)} \right) \quad (3.12)$$

This construction gives us more algorithmic freedom in the Monte Carlo algorithm as any bias introduced by the a priori probabilities $\mathcal{A}(\mu \rightarrow \nu)$ could be corrected in the acceptance probabilities.

In a typical MCMC new configurations are proposed by making changes in the present configuration, we call this a *move*. As we will see quite often below, such moves could be *local*, where the new configuration is generated by changing a single degree of freedom or *non-local*, which involves a change over multiple degrees of freedom.

The algorithms in the following sections all satisfy the detailed balance condition of Eq. 3.6. However, for a Markov chain with more than two states, it is sufficient to satisfy only the balance condition of Eq. 3.5 without locally satisfying detailed balance and this gives much more freedom in choosing the transition probabilities to make the sampling more efficient. Such a class of algorithms are referred to as *non-reversible* MCMC algorithms. Some recent advances in this class of algorithms include the *Event-Chain Monte Carlo* [59] introduced for models of hard spheres [60] and *Geometric allocation* [61, 62].

3.2 Directed Loop Monte Carlo

The simplest local move one could make in a dimer configuration is a *plaquette flip*, shown in Fig. 3.2. As we saw in the previous chapter the configuration space of all dimer coverings on a toroidal geometry have a topological nature, a plaquette flip could only generate new configurations only in a single topological sector and is therefore not ergodic. To make the MCMC ergodic we need non-local moves which could change topological sectors. One such non-local move is a closed loop on the square lattice which toggles the dimer occupancy along its path, shown in Fig. 3.2. If this loop winds around the periodic boundary it changes the topological sector of the dimer configuration.

A commonly used algorithm which proposes new configurations through such non-local loops called the *directed loop algorithm* [63, 64, 65, 66, 67] which aims at minimizing the bounce back probability at every step of the construction of the non-local loop. We describe it for a close-packed dimer and loop constraint on the square lattice (see Fig. 3.3 for a graphic illustration of some of the steps), but the algorithm is quite general and

could be easily formulated for any constraint and lattice structure.

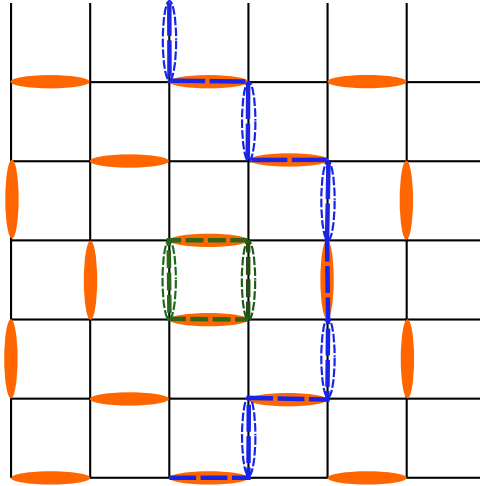


Figure 3.2: A local move shown in green involves a plaquette flip vs a non-local loop move shown in blue. The new configuration is generated such that if the loop passes on an empty bond it creates a dimer (shown in dashed) and when it passes over a dimer it is deleted.

1. We start with a fully packed dimer or loop configuration \mathcal{C} . A lattice site S is chosen randomly to start the directed loop. Now with a probability $p_0 = \min(1, \exp\{\beta(E(\mathcal{C}) - E(\mathcal{C}'))\})$ we break the constraint on site S by replacing the bond with a half dimer, see Fig. 3.3(a). Note that, in the case of loops we have an additional choice between two bonds since there are always two dimers touching a site S . This generates a new configuration \mathcal{C}' with a monomer on site S and another *mobile* monomer M at the end of the half dimer. Let us give this monomer M a binary valued 'momentum' internal degree of freedom which points into a half-dimer or away from it, in this case it is pointing into the half-dimer and away from site S . If we are interested in interacting models, when calculating the energy E of a configuration the interaction between a half-dimer and parallel dimer is considered as half that of two full parallel dimers. With a probability $1 - p_0$ we reject this move.
2. If the monomer M is moving into a dimer annihilating it in the process, it will subsequently create a dimer on the next empty bond keeping in line with the constraint. For a close packed dimer configuration the monomer has four choices - create a dimer on one of the three empty bonds or reverse its direction (momentum). Similarly for a close-packed loop configuration the monomer has three choices - create a dimer on one of the two empty bonds or reverse its direction. We will call the

reverse (see Fig. 3.3(b)) move the *bounce back* process. The transition probabilities for these moves are chosen so as to satisfy detailed balance, we will describe them further below.

3. If the monomer M is moving away from a dimer creating in the process, it will subsequently annihilate the dimer on the next occupied bond(s) in accordance with the constraint. For a close-packed dimer configuration the monomer only has two choices - annihilate the next occupied bond or reverse direction (bounce back). For a close-packed loop configuration it has three choices - annihilate the dimer on one of the two occupied bonds or bounce back. This is illustrated in Fig. 3.3(c). The transition probabilities are again chosen to satisfy detailed balance, they are described further below.
4. We repeat steps (2) and (3) until the loop closes. If in the current configuration \mathcal{C}' the monomer M sees the starting site S the loop can terminate and generate a new configuration C with probability $p_{term} = \min(1, \exp\{\beta(E(\mathcal{C}') - E(C))\})$ and with probability $1 - p_{term}$ it reverses direction. Notice how this move is just the reverse move of 1).

Now let us look at how we set the transition probabilities. Let us consider a general case where we have n states each with a weight $W_i (i = 1, \dots, n)$. Let $p(i \rightarrow j)$ be the transition probabilities between two states i and j . We set the transition probabilities in the following way [68, 69], keeping in mind that they satisfy the detailed balance condition of Eq. 3.6

$$p(i \rightarrow j) = \begin{cases} \frac{W_i - c}{\sum_{i=1}^n W_i - c}, \text{ for } i = j \\ \frac{W_j}{\sum_{i=1}^n W_i - c}, \text{ for } i \neq j \end{cases} \quad (3.13)$$

where $c = \min(W_1, W_2, \dots, W_n)$. One can check that for $n = 2$ the above transition probabilities reduce to those given by the Metropolis algorithm in Eq. 3.7. Setting $c = 0$ reduces to the heat-bath algorithm, but as we argued in the previous section (albeit for only two states) we use the Metropolis scheme given its lower bounce back rate.

Having more transition states ($n > 2$), gives more freedom of choosing the transition probabilities and possibly getting even lower bounce back rates than Eq. 3.13, sometimes even making the algorithm bounce back free (although this heavily depends on the weights). Interested readers are referred to [61, 62].

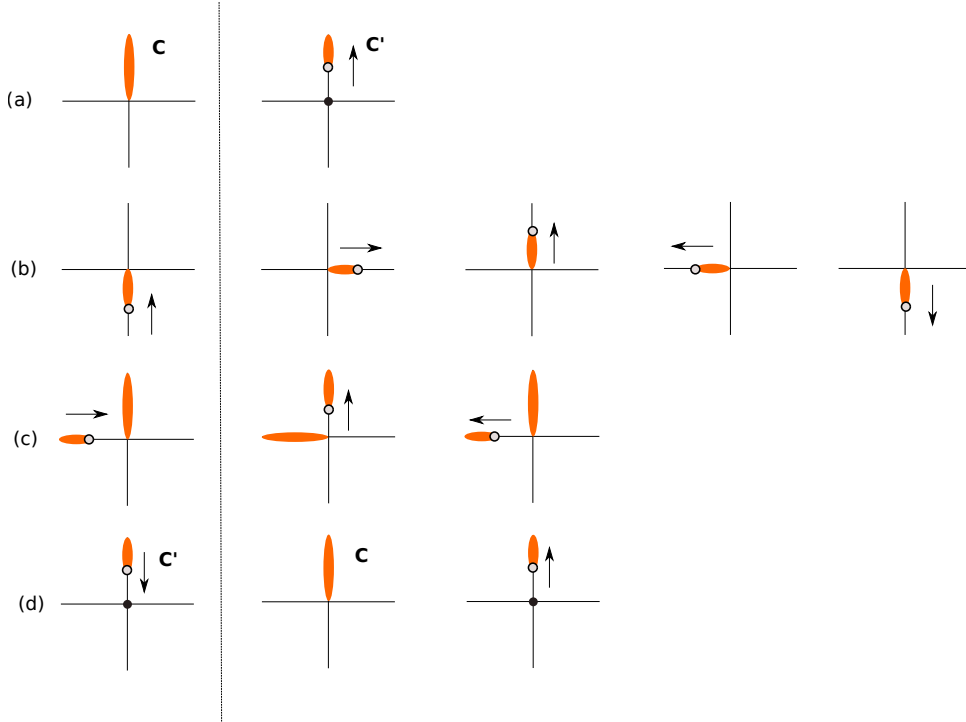


Figure 3.3: (a) Starting move (move 1) which generates the broken dimer (or loop segment) configuration C' with the static monomer (filled black circle) and a moving monomer (unfilled circle) having momentum pointing into a dimer. (b) On the left is shown the configuration C' from the previous step. On the right are four possible transition configurations with the monomer now creating a new dimer. (c) The left shows the configuration with the monomer creating a dimer and on the right are the two possible transition configurations. (d) Termination move where the loop closes.

3.3 Stochastic Series Expansion

In this section we move to Monte Carlo simulations of quantum problems and in particular we review the Stochastic Series Expansion (SSE) method, which has been applied over the years to many quantum lattice models.

Suppose we want to estimate the thermal expectation value of an observable \hat{O} given by

$$\langle \hat{O} \rangle = \frac{1}{Z} \text{Tr} \left(e^{-\beta H} \hat{O} \right) \quad (3.14)$$

where $Z = \text{Tr} e^{-\beta H}$ is the partition function. The idea behind SSE [70] is to construct a finite configuration space by Taylor expanding the Boltzmann operator and perform Monte Carlo sampling in this configuration space to evaluate the averages of observables. We expand the trace and the Boltzmann operator -

$$\langle \hat{O} \rangle = \frac{1}{Z} \sum_{n=0}^{\infty} \sum_{\psi} \frac{(\beta)^n}{n!} \langle \psi | (-H)^n \hat{O} | \psi \rangle \quad (3.15)$$

Let us assume for simplicity that \hat{O} is diagonal in the basis $|\psi\rangle$ and $\hat{O}|\psi\rangle = O_\psi|\psi\rangle$. Let us add $n - 1$ resolution of identities $I = \sum_\psi |\psi\rangle\langle\psi|$ in Eq. 3.15

$$\langle\hat{O}\rangle = \frac{1}{Z} \sum_{n=0}^{\infty} \sum_{\psi_i} \frac{(\beta)^n}{n!} \langle\psi_0| - H|\psi_{n-1}\rangle \langle\psi_{n-1}| - H|\psi_{n-2}\rangle \cdots \langle\psi_1| - H|\psi_0\rangle O_\psi \quad (3.16)$$

where $\psi_i \in [\psi_0, \psi_1 \cdots \psi_{n-1}]$

One can now write the Hamiltonian as a sum of elementary lattice operators

$$H = - \sum_a \sum_t H_{t,a} \quad (3.17)$$

where the index t denotes the type of operator (diagonal or off-diagonal, with respect to the computational basis $\{|\psi\rangle\}$) and a denotes its position on the lattice - for example a plaquette or a bond. We now rewrite Eq. 3.16 as -

$$\langle\hat{O}\rangle = \frac{1}{Z} \sum_{n=0}^{\infty} \sum_{\psi_i} \sum_{S_n} \frac{(\beta)^n}{n!} \langle\psi_0| H_{t_n, i_n} |\psi_{n-1}\rangle \langle\psi_{n-1}| H_{t_{n-1}, i_{n-1}} |\psi_{n-2}\rangle \cdots \langle\psi_1| H_{t_1, i_1} |\psi_0\rangle O_\psi \quad (3.18)$$

where $S_n = [H_{t_n, i_n}, H_{t_{n-1}, i_{n-1}}, \cdots, H_{t_1, i_1}]$ is called an **operator string** which contains the locations and the types of operators $H_{t,i}$ and the summation S_n is over all possible types and locations of the operators $H_{t,i}$ in the string of length n .

In order to construct a finite sampling configuration space we truncate the second summation in Eq. 3.18 to some value $n = L$. This L is chosen such that it is greater than the largest value of n occurring in the simulation. In the second summation, for any $n < L$ we enlarge the configuration space by adding $L - n$ identity operators I in the operator string S . We must therefore divide the partition function Z by a factor $\binom{L}{n}$, which is the number of ways of placing the $L - n$ identities in the operator string, to account for this degeneracy. Taking all of this into account we can write Eq. 3.18 as

$$\langle\hat{O}\rangle = \frac{1}{Z} \sum_{\psi_i} \sum_{S_L} \frac{(\beta)^n (L - n)!}{L!} \langle\psi_0| H_{t_L, i_L} |\psi_{L-1}\rangle \langle\psi_{L-1}| H_{t_{L-1}, i_{L-1}} |\psi_{L-2}\rangle \cdots \langle\psi_1| H_{t_1, i_1} |\psi_0\rangle O_\psi \quad (3.19)$$

where the second summation in Eq. 3.18 has been absorbed in the summation over the operator string and n now denotes the number of **non-identity** operators in the operator string S_L .

3.3.1 Monte Carlo updates

In order to describe the MC update protocols, let us take a specific example for the Hamiltonian, although the **local** update scheme is model independent. We will focus from now on the previously described Hamiltonian for the quantum dimer model on the square lattice.

$$H_{\text{QDM}} = \sum_{\square} -t (|\square\rangle\langle\square| + |\square\rangle\langle\square|) + V (|\square\rangle\langle\square| + |\square\rangle\langle\square|) \quad (3.20)$$

Let us slightly modify the Hamiltonian H to be $H = H_{\text{QDM}} - (C + V)N_p$ where C is a constant, V is the coupling of the diagonal term in Eq. 3.20 and N_p is total number of plaquettes on the square lattice. The reason for expressing the Hamiltonian in this way will be clear later. Let us now write H in the form of Eq. 3.17

$$-H = \sum_{i \in P} (K_i + V_i) \quad (3.21)$$

where the summation is over all plaquettes P of the square lattice. We can make a comparison with Eq. 3.17: the index i in Eq. 3.3.1 corresponds to the index a which tells us the location of the operator on the lattice and index t in Eq. 3.17 now denotes the two kinds of operator types - K (off-diagonal) and V (diagonal) with the identity operators I in addition to these. To make the correspondence clearer - $H_{0,0} \equiv I$, $H_{1,a} \equiv V_i$ and $H_{2,a} \equiv K_i$.

One can now view Eq. 3.19 in the form

$$\langle \hat{O} \rangle = \frac{\sum_x W(x) O_x}{\sum_x W(x)} \quad (3.22)$$

here $x \equiv [S_L, \psi_i]$ denotes a state in the configuration space made up of the operator string of a fixed length S_L and the intermediate states ψ_i which are nothing but 2D dimer configurations on the square lattice. This is represented in a pictorial form in Fig. 3.4. The weight of a configuration x is given by

$$W(x) = \frac{\beta^n (L - n)!}{L!} \prod_{i=1}^L \langle \psi_{i-1} | H_{t_i, a_i} | \psi_i \rangle \quad (3.23)$$

We can now perform importance sampling for Eq. 3.22 by a Markov Chain Monte Carlo scheme.

In order to avoid the **sign problem** one must ensure that the weight $W(x) > 0$ and

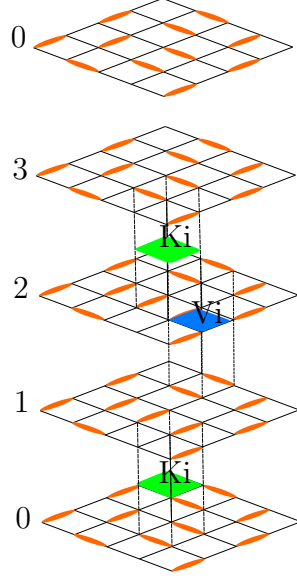


Figure 3.4: Pictorial representation of an operator string $S = [K_i, V_i, K_i, I]$ of length $M = 4$. It must be noted that due to periodicity on the imaginary time axis of the path integral at finite β , $|\psi_4\rangle = |\psi_0\rangle$.

hence ensure the positivity of the matrix elements $\langle \psi_{i-1} | H_{t_i, a_i} | \psi_i \rangle$ in Eq. 3.23. Generally one needs to worry only about the off-diagonal matrix elements since the diagonal ones could be made positive by adding a constant shift as we have done in our case of H_{QDM} . Let us write all the matrix elements for the Hamiltonian $H = H_{QDM} - (C + V)N_p$. We have :

$$\begin{aligned} \langle \square | K_i | \square \rangle &= \langle \square | K_i | \square \rangle = 1. \\ \langle \square | V_i | \square \rangle &= \langle \square | V_i | \square \rangle = C \end{aligned} \quad (3.24)$$

$$\langle \square | V_i | \square \rangle = \langle \square | V_i | \square \rangle = \langle \square | V_i | \square \rangle = \langle \square | V_i | \square \rangle = \langle \square | V_i | \square \rangle = C + V. \quad (3.25)$$

Here we have set $t = 1$ for simplicity. We adjust C so as to keep all the matrix elements positive.

Let us now discuss the simplest **local** MC update one could make, we will also refer to this as a **diagonal** update. This update will only touch the diagonal operators V_i in the operator string. It amounts to 1) removing a diagonal operator on a plaquette, i.e replacing it with an identity operator ($V_i \rightarrow I$) or 2) adding a diagonal operator on a random plaquette if there was an identity before ($I \rightarrow V_i$). We can get the transition probabilities from the detailed balance equation Eq. 3.6. Move 1) changes $n \rightarrow n - 1$, the transition probability is given by

$$P(V_i \rightarrow I) = \min\left(1, \frac{L - n + 1}{N_p \beta \langle \psi | H_{1,i} | \psi \rangle}\right) \quad (3.26)$$

Move 2) changes $n \rightarrow n + 1$, its transition probability is given by

$$P(I \rightarrow V_i) = \min\left(1, \frac{N_p \beta \langle \psi | H_{1,i} | \psi \rangle}{L - n}\right) \quad (3.27)$$

Here $\langle \psi | H_{1,i} | \psi \rangle = C$ or $C + V$ depending on the type of diagonal plaquette as shown in Eq. 3.24 and Eq. 3.25. We also have a factor of N_p i.e the total number of plaquettes in the square lattice since one has a random choice of plaquette when adding a diagonal operator in move 2).

3.4 Sweeping Cluster Algorithm

The diagonal update by itself is not ergodic as it does not create or modify the off-diagonal operators in the operator string. To make the sampling ergodic one usually relies on certain non local update schemes like the worm/directed loop algorithms in SSE. The presence of constraints in our model makes finding such a non local move non-trivial as one has to ensure that the proposed update does not violate this constraint.

The recently developed Sweeping Cluster Algorithm (SCA) [71] ensures to do just that. In SCA we construct a cluster of operators in the operator string following probabilistic rules which depend on the weights of these operators. Once the cluster is built, we update the operator type of the operators involved in the cluster and also update the dimer configurations simultaneously without violating the hard core constraint.

In the SSE operator string, every operator resides between two consecutive imaginary time slices say t_i and t_{i+1} . We represent these operators pictorially as shown in Fig. 3.5, the dimer configuration below shows the configuration for the plaquette on time slice t_i while the one on top for time slice t_{i+1} . Every operator has *legs*, in this case eight legs, which link to other operators in the operator string.

In order to track the cluster building we introduce *update lines* which live on the legs of the plaquette operators in the SSE linked vertex structure shown in Fig. 3.4. The presence of an update line on a leg tells us to toggle the dimer occupancy of the link where that leg points to (Fig. 3.6). Due to the linked vertex structure of the SSE, the cluster construction involves rules on propagating these update lines to the next operator in the linked vertex structure.

We can look at the algorithm as a Markov chain between the following different operator types

- *Off-Diagonal flippable* : denoted by K_i in Eq. 3.24 with weight 1

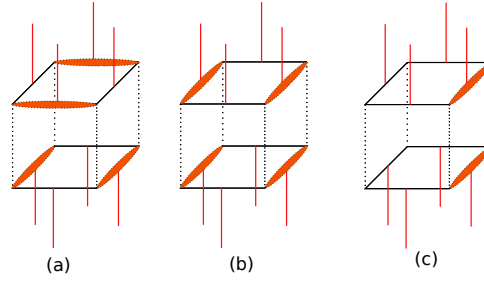


Figure 3.5: Pictorial illustration of an operator in the operator string with four incoming legs and four outgoing legs. The three different operator types are - (a) Off-diagonal flippable operator, (b) Diagonal flippable operator and (c) Diagonal non-flippable operator.

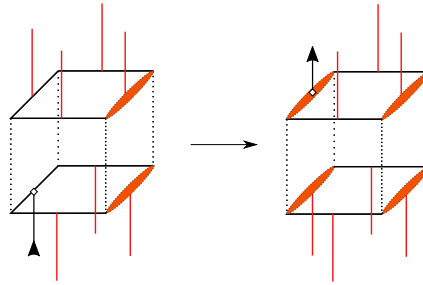


Figure 3.6: Demonstration of an update line (shown in black) propagating in forward imaginary time direction.

- *Diagonal flippable* : denoted by V_i in Eq. 3.24 with weight C
- *Diagonal non-flippable* : denoted by V_i in Eq. 3.25 with weight $C + V$

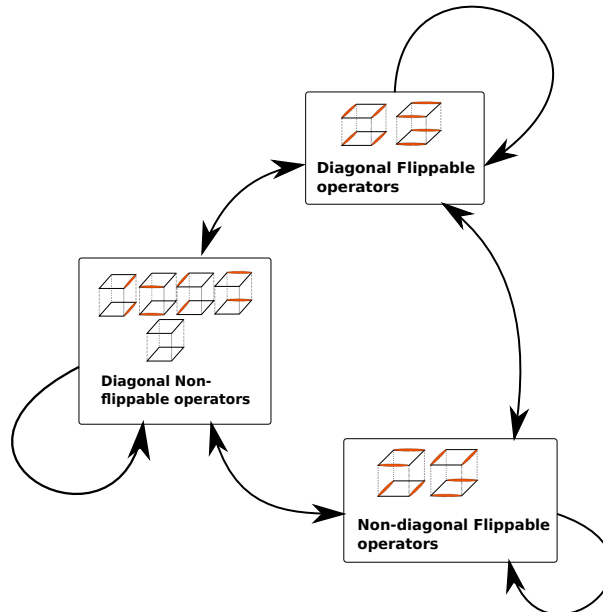


Figure 3.7: The cluster building process in the Sweeping cluster algorithm could be thought of as a Markov chain between different operator types.

3.4.1 Rules for building the Cluster

Table (3.1) summarizes all the different possible local moves which form the cluster. Since these local moves can change the type of operators, we have categorized them as transitions between the operator types as described in Fig. 3.7. The pictorial representation of each move shows how to propagate the incoming update lines to the next operator in the operator string, in the same spirit as shown in Fig. 3.6. Each local move is also assigned an a priori probability $\mathcal{A}(\mu \rightarrow \nu)$.

Algorithm for constructing the cluster

- Choose a flippable operator randomly to start the cluster. Note that we always start the cluster with a flippable operator.
 If the operator is diagonal : perform move (1)a shown in Table(3.1) with probability $\min(1, 1/C)$, otherwise don't start the cluster
 If the operator is off-diagonal : perform move (2)a shown in Table(3.1) with probability $\min(1, C)$, otherwise don't start the cluster
- Continue building the cluster with moves (3)-(7) in Table(3.1). We set an a priori probability P for move (3) and $1 - P$ for move (4) which is nothing but the complementary choice for (3). P here is a free parameter of the simulation, which for most cases we set to $1/2$. Moves (5) and (6), which are reverse moves of (3) and (4) respectively, are always accepted. This breaks detailed balance locally but will be restored by a global acceptance probability for the cluster later. Moves (6) and (7) are always accepted since they do not change the weight of the operator string.
- If the plaquette is flippable and the **total** update lines left are 4, we have two possibilities.
 If the operator is diagonal : stop the cluster with move (1)b with probability $\min(1, 1/C)$, otherwise continue the update lines with move (7)a
 If the operator is off-diagonal : stop the cluster with move (2)b with probability $\min(1, C)$, otherwise continue the update lines with move (7)b
 Notice the above two are exactly the reverse of (2)a and (1)a respectively, and therefore satisfy detailed balance.

3.4.2 Cluster acceptance probability

To satisfy detailed balance, we assign an acceptance probability to *flip* the cluster. Let us derive this acceptance probability here.

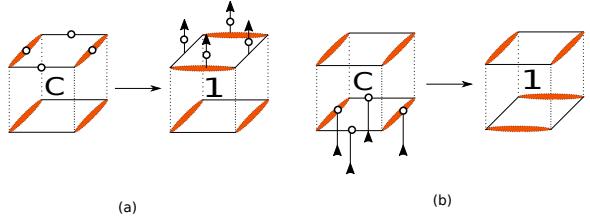
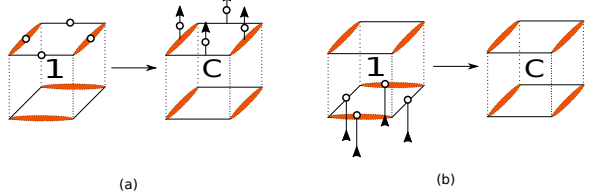
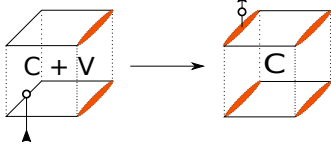
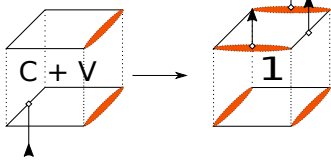
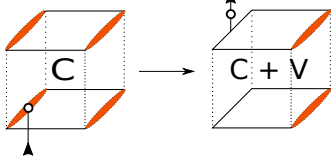
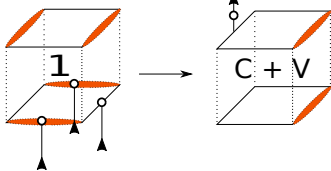
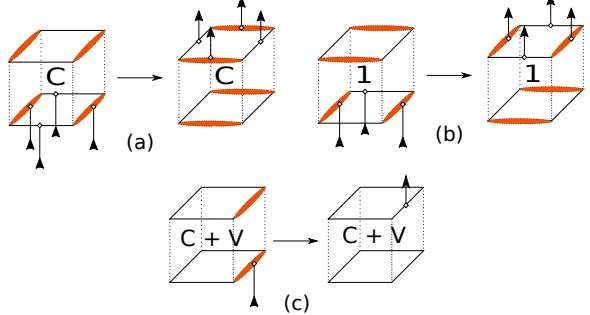
Transition type	An example
(1) Transitions from diagonal flippable to off-diagonal flippable. (a) shows start of the cluster. (b) shows the end of the cluster.	
(2) Transitions from off-diagonal flippable to diagonal flippable. (a) shows start of the cluster. (b) shows the end of the cluster	
(3) Transitions from diagonal non-flippable to diagonal flippable. A priori probability is $\mathcal{A}(C + V \rightarrow C) = P$	
(4) Transitions from diagonal non-flippable to non-diagonal flippable. A priori probability is $\mathcal{A}(C + V \rightarrow 1) = 1 - P$	
(5) Transitions from diagonal flippable to diagonal non-flippable	
(6) Transitions from non-diagonal flippable to diagonal non-flippable	
(7) Transitions which do not change the weight	

Table 3.1: Illustration of all the possible transitions between different operator types. The table also shows how to propagate the update lines.

Before starting a cluster let us consider an operator string A which has $\mathcal{N}^A(1)$ off-diagonal flippable operators, $\mathcal{N}^A(C)$ diagonal flippable operators and $\mathcal{N}^A(C + V)$ diagonal non-

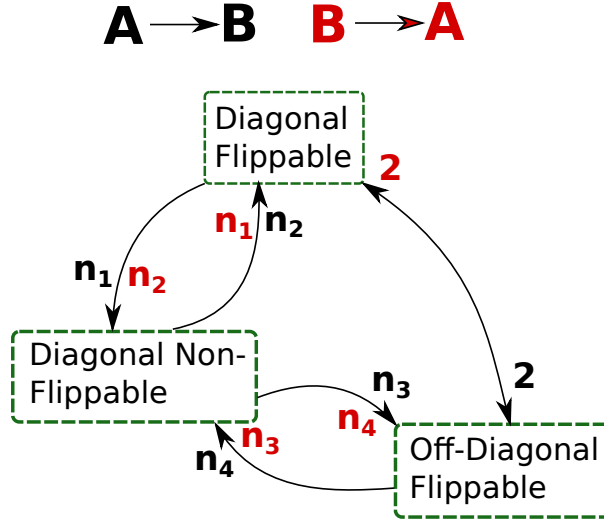


Figure 3.8: The figure illustrates the number of transitions (n_1, n_2, n_3, n_4) between operators of different types during the cluster construction and the cluster construction in reverse (shown in red). The 2 denotes the two transitions between diagonal and off-diagonal flippable operators occurring at the start and end of the cluster construction.

flippable operators. The weight of operator string A therefore is,

$$w(A) = C^{\mathcal{N}^A(C)}(C + V)^{\mathcal{N}^A(C+V)}(1)^{\mathcal{N}^A(1)}. \quad (3.28)$$

A new operator string B is *proposed* by constructing a cluster using the rules we saw in the previous subsection. This cluster involves certain number of transitions between various operator types, say n_1 transitions of type $C \rightarrow C + V$, n_2 of type $C + V \rightarrow C$, n_3 of type $C + V \rightarrow 1$ and n_4 of type $1 \rightarrow C + V$. In addition, there are always 2 transitions of type $C \rightarrow 1$ or $1 \rightarrow C$ which are the start and end of the cluster. We only need to keep track of the transitions which change the weight. Fig. 3.8 shows a picture of the above transitions.

From the above numbers of transitions the weight of the new operator string B is,

$$w(B) = C^{\mathcal{N}^A(C)-n_1+n_2}(C + V)^{\mathcal{N}^A(C+V)+n_1+n_4-n_2-n_3}(1)^{\mathcal{N}^A(1)-n_4+n_3}. \quad (3.29)$$

Notice we have not considered the weight change occurring from the 2 transitions at the start and end of the cluster, since these moves already satisfy detailed balance. Before writing out the detailed balance equation, we also need to look at the *reverse cluster* move which takes us from B back to A . These transitions are again shown in Fig. 3.8. The accumulated a priori probabilities for the cluster and the reverse cluster are,

$$\begin{aligned} \mathcal{A}(A \rightarrow B) &= \frac{1}{\mathcal{N}_{FP}^A} P^{n_2} (1 - P)^{n_3} \\ \mathcal{A}(B \rightarrow A) &= \frac{1}{\mathcal{N}_{FP}^B} P^{n_1} (1 - P)^{n_4} \end{aligned} \quad (3.30)$$

where \mathcal{N}_{FP}^A and \mathcal{N}_{FP}^B denote the number of flippable operators in operator string A and B respectively. The factors $\frac{1}{\mathcal{N}_{FP}^A}$ and $\frac{1}{\mathcal{N}_{FP}^B}$ stand for the random choice of flippable operator at the start of the cluster. From Eq(3.12), the acceptance probability to flip the cluster is given by

$$\mathcal{P}(A \rightarrow B) = \min \left\{ 1, \frac{\mathcal{N}_{FP}^A}{\mathcal{N}_{FP}^B} \left(\frac{P(C+V)}{C} \right)^{n_1-n_2} [(1-P)(C+V)]^{n_4-n_3} \right\} \quad (3.31)$$

The above equation shows that one need only keep track of the *flux* of transitions between flippable and non-flippable operators when building the cluster. Notice that unlike the directed loop algorithms used in SSE, SCA is not rejection free by construction. Since in an SSE the average number of flippable operators is given by $\langle \mathcal{N}_{FP} \rangle = |\beta \langle H_{QDM} \rangle|$, the ratio $\mathcal{N}_{FP}^A/\mathcal{N}_{FP}^B \simeq 1$ in Eq. 3.31. By choosing $P = C/(C+V)$, one could see that $\mathcal{P}(A \rightarrow B) \simeq 1$ at the RK point i.e $V = 1$ and the algorithm could be regarded as rejection free. However, away from the RK point SCA has a finite rejection rate. The above choice of P is not feasible anywhere other than the RK point (for example at $V = 0$, with this choice of P the acceptance probability is zero).

3.5 Classical Loop Move

As we saw in the previous chapter, fluctuations of winding numbers are crucial to studying the critical phase in the dimer model on the square lattice. The SCA as described in the last section is ergodic only in the topological sector it was initiated in. We describe below a simple modification to the SCA which enables us to change winding sectors during the simulation. The basic idea involves performing a classical directed loop move described in the beginning of the chapter, by constructing an equivalent classical interacting dimer model of the SSE operator string. This classical loop move is performed on all time slices of the operator string.

To begin with, one can see that, for any plaquette which has a non-diagonal flippable operator in any imaginary time slice of the operator string, a directed loop which passes through any of the corresponding dimers of this plaquette will not preserve the flippability of this plaquette. To circumvent this problem we will perform directed loops in a restricted region within a particular dimer configuration state ψ .

Given an operator string, we identify the set of plaquettes \mathcal{P}_K which have an off-diagonal operator in any imaginary time slice. We now create a new state ψ' with dimers occupying all the edges of those plaquettes in \mathcal{P}_K (shown by green dimers in Fig. 3.9(b,d)). We now associate infinite fugacity for the dimers on these edges such that the directed loop never passes through these edges, essentially freezing them (the dimer configuration on these

edges is never modified).

On any other plaquette with a diagonal operator in the operator string will contribute a weight of C , if the operator is flippable and a weight of $C + V$, if the operator is non-flippable. Therefore, a directed loop passing through the edges of these plaquettes must take into account these weights in order to satisfy detailed balance. We do this by associating a pseudo-energy E for the state ψ' by adding some interaction between parallel dimers for these plaquettes as described below.

1. If the plaquette i has no diagonal operators in any imaginary time slice, there is no pseudo-energy associated with this plaquette ($e_i = 0$).
2. Now we consider a plaquette i which is *not adjacent* to a plaquette in \mathcal{P}_K . If there are n diagonal operators at various imaginary time slices on i , we associate a pseudo-energy of $e_i = n \ln\left(\frac{C+V}{C}\right)$ between any two parallel dimers in i . This is illustrated in Fig. 3.9 (a,b).
3. Now consider the case where a plaquette i with diagonal operators is *adjacent* to a plaquette k in \mathcal{P}_K . There is one edge which is shared by k and i . Notice that the occupancy of this edge is different in different imaginary time slices. Let n_2 be the number of times this shared edge is occupied. The pseudo-energy associated with parallel dimers in i is $e_i = n_2 \ln\left(\frac{C+V}{C}\right)$. This is illustrated in Fig. 3.9 (c,d).
4. If the plaquette i is adjacent to more than one plaquettes from \mathcal{P}_K , then none of the edges in i can change their occupancy as they are frozen due to infinite fugacity as explained before.

Hence for a dimer configuration on any imaginary time slice, we can define an energy $E = \sum_{i \in \mathcal{P}} e_i x_i$ where $x_i = 1$ if there is a pair of parallel dimers in the i -th plaquette and $x_i = 0$ otherwise. What we have now is a classical interacting dimer model (as discussed in section 2.2) on which we can perform the directed loop algorithm discussed in section 3.2. One should note that the directed loop does not touch any of the off-diagonal operators but it does make transitions between flippable and non-flippable diagonal operators. Finally, the state ψ_1 is constructed by copying the configurations of \mathcal{P}_K in ψ into ψ'_1 . Indeed the directed loop move is always accepted with probability one.

Notice that the directed loop moves are performed on a depleted square lattice since some of the bonds are blocked off due to the presence of off-diagonal operators on the corresponding plaquette, which brings us to the drawback of this method. Having many off-diagonal operators in the operator string leads to a highly depleted square lattice and makes it harder for the directed loop algorithm to make long closed loops which wind around the toroidal boundaries to change the topological sectors. As we will see in the

next chapter, this leads to severe hinderance at low temperature as the number of off-diagonal operators is proportional to $|\beta\langle K \rangle|$ where $\langle K \rangle$ is extensive.

To summarize, one Monte Carlo step in the simulation therefore involves N_d diagonal moves, N_{sca} sweeping cluster moves and N_c classical moves.

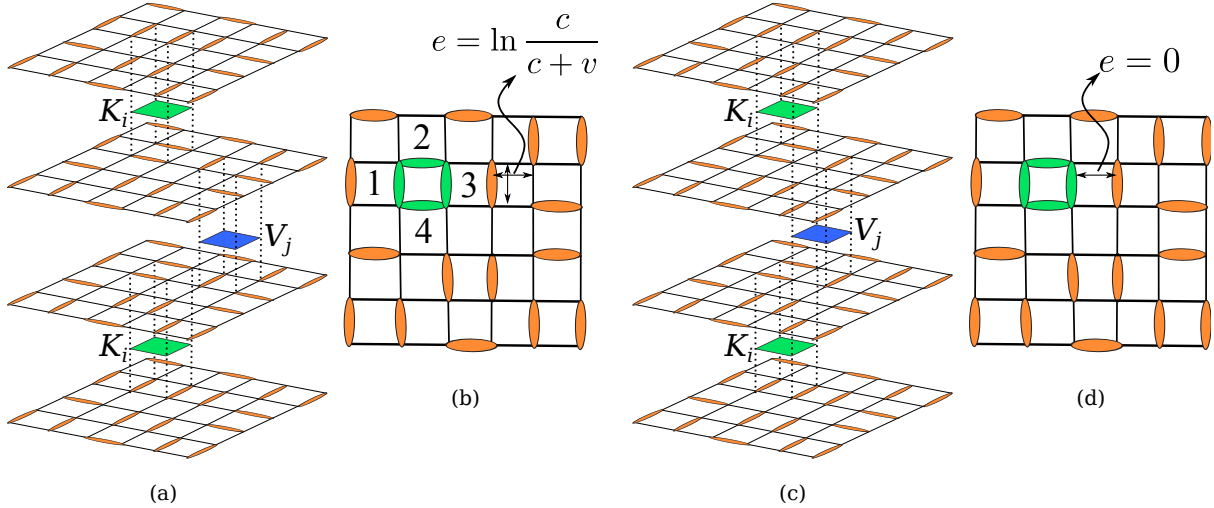


Figure 3.9: Illustration of the construction of the classical directed loop update in SSE. The green and blue squares in the panels (a) and (c) represent K_i and V_j vertices respectively. Panel (a) illustrates an operator string in which the diagonal V_j vertex is located in a plaquette not adjacent to the plaquettes containing the K_i vertex. In the effective model, there is a pseudo-energy $e = \ln \frac{c}{c+v}$ associated to parallel dimers inside the plaquette j . Dimers in other plaquettes do not interact. The effective model is shown in panel (b). The edges around plaquette containing K_i are fully filled and frozen. In the plaquettes nearest to it, labelled 1,2,3,4 in panel (b), the edges touching the plaquette containing K_i are always empty and will also not be allowed to contain a dimer. Panel (c) illustrates an operator string which has plaquettes containing V_j and K_i adjacent to each other. The rules giving the effective model is similar to that in panels (a,b) except that the blue squares (V_j) contribute to the pseudo-energy e in j only if the edge shared by the two plaquettes is occupied in the time slice containing V_j . In the illustration the edge is unoccupied, so $e = 0$.

Chapter 4

Finite temperature phase diagram of the QDM on square lattice

4.1 Quantum Dimer Model at finite temperature

From standard arguments, we expect that the classical theory given by Eq. 2.5 in chapter 2 should capture the finite temperature phases and phase transitions of the QDM as well. We verify our above expectation in this chapter using the SCA described in the previous chapter. We begin by defining the order parameters which capture the low temperature ordered phases. We then study the phase transitions out of these ordered phases by monitoring their order parameters and obtain the phase boundary from the Binder cumulants. This is followed by a closer study of the critical phase by observing the variation of the Coulomb gas constant with temperature and V during the course of which we will also probe the dimer-dimer and monomer-monomer correlation functions. We end the chapter by a high temperature expansion argument to understand the variation of g we found from the simulations.

Reference [48] conjectured a specific form for the phase diagram (see Fig. 32 in Ref. [48]) with **monotonous** behavior of the “iso- g ” lines. We show in this chapter that the actual constant $g(T, V)$ lines exhibit a **non-monotonous re-entrant** behavior as a function of T below the RK point. Additionally, we investigate the phase transitions (starting from the high-temperature critical phase) deep in the columnar ($V/t < 1$) and staggered-like ($V/t > 1$) regimes, and conclude that they are similar to the ones observed in the CIDM obtained in the large potential limits ($|V/t| \rightarrow \infty$). These results are summarized in the phase diagram of Fig. 4.1.

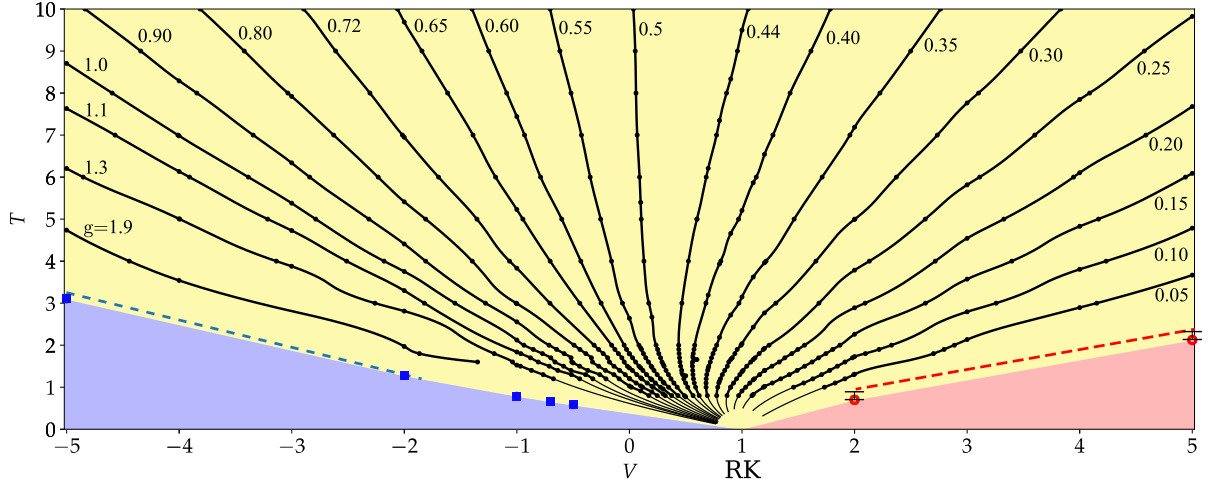


Figure 4.1: Finite-temperature phase diagram of the quantum dimer model on the square lattice, in the $(V/t, T/t)$ plane ($t = 1$ is assumed here). The yellow, blue and red shades indicate the critical (disordered) phase, the columnar phase and the staggered phase respectively. The black solid lines show constant g lines. The black dots were obtained by linear interpolation of g values calculated using Eq. 2.8 from numerically obtained $\langle W^2 \rangle$ values on a large grid of (V, T) values. The thick solid lines joining them are quadratic interpolations of the dots with same g . Thin solid lines are extrapolations towards the RK point $V/t = 1$; they cover regions inaccessible to the QMC simulations. To map out the entire high-temperature phase, we used simulations for systems of linear size $L = 24$ (we checked on selected points that increasing system size up to $L = 64$ did not change the phase diagram significantly). The blue (square) and red (empty circle) symbols denote the finite-temperature phase transitions to a columnar phase and staggered phase. These are determined using, respectively, the Binder cumulants of the dimer symmetry breaking order parameter B_D (Eq. 4.5) and the absolute winding $B_{|W|}$ (Eq. 4.6). The dotted lines represent the classical asymptotic behavior obtained for the CIDM where $T_c = 0.65|V|$ (for $V < 0$, attractive CIDM [47]) and $T_c = 0.475V$ (for $V > 0$, repulsive CIDM [31]). The transition to columnar (respectively staggered) order are expected to occur at $g_c = 4$ (respectively $g = 0$).

4.1.1 Order parameters

As we saw in the previous sections, for $V/t < 1$ there is a possibility of three phases which break different symmetries. The simplest order parameter which could capture the $\pi/2$ rotation symmetry breaking is the *dimer rotation symmetry breaking* order parameter

$$D = 2/L^2 \langle |N(\ominus) - N(\circ)| \rangle \quad (4.1)$$

which measures the absolute value of the difference between the number of horizontal and vertical dimers. This order parameter will not be able to distinguish between columnar and mixed phases as they both break $\pi/2$ rotation symmetry but it will be zero for the plaquette phase. It is quite clear that $D = 1$ for all of the 4 columnar configurations and that it takes some non-zero value for the mixed phase.

In order to distinguish all three phases, one needs an order parameter sensitive to both translation and rotation symmetry breaking. For this we define a *complex columnar order parameter* [35] Ψ_{col} which is defined on every lattice site $\mathbf{r} = (x, y)$ as

$$\Psi_{\text{col}}(\mathbf{r}) = (-1)^x [d^{\bullet\leftarrow}(\mathbf{r}) - d^{\leftarrow\bullet}(\mathbf{r})] + i(-1)^y [d^{\bullet\downarrow}(\mathbf{r}) - d^{\downarrow\bullet}(\mathbf{r})] \quad (4.2)$$

where the dot \bullet and the line \leftarrow denotes the relative positions of the lattice site \mathbf{r} and an adjoining edge. The dimer operator $d^{\bullet\leftarrow}(\mathbf{r})$ is 1 if there is a horizontal dimer on the right horizontal bond touching lattice site \mathbf{r} , and 0 otherwise (other operators are defined similarly). The total order parameter is averaged over all sites belonging to one sublattice:

$$\Psi_{\text{col}} = \frac{2}{L^2} \sum_{\mathbf{r} \in A} \Psi_{\text{col}}(\mathbf{r}). \quad (4.3)$$

The magnitude of this complex order parameter is 1 in all three ordered states hence it can only be used to distinguish the disordered phase. The phase θ of Ψ_{col} gives us much more information. The 4 columnar states correspond to $\theta = (0, \pi/2, \pi, 3\pi/2)$. It is easy to see that the 4 plaquette states correspond to $\theta = (\pi/4, 3\pi/4, 5\pi/4, 7\pi/4)$ and the 8 mixed states correspond to 8 values of θ depending on their superposition amplitudes (see [38] for a nice pictorial illustration).

For the staggered states, one can build an order parameter based on the winding numbers. Each winding number W_x and W_y can take values between $-L/2$ and $L/2$. Since all configurations belonging to the staggered phase have maximal tilt, the winding numbers of these configurations lie on a rhombus of equation $|W_x| + |W_y| = L/2$ [31, 33] (shown previously in Fig. 2.2). Using this we can cook up a simple order parameter

$$|W| = \frac{2}{L} (|W_x| + |W_y|) \quad (4.4)$$

4.1.2 Columnar side $V/t < 1$

For $V/t < 1$, similar to the CIDM we expect a Kosterlitz Thouless type phase transition to the low temperature ordered states. To monitor this phase transition we resort to the Binder cumulant of the dimer rotation symmetry breaking order parameter D given by

$$B_D = \frac{\langle D^4 \rangle}{\langle D^2 \rangle^2} \quad (4.5)$$

Unlike for a second order phase transition, it is still not clear how a Binder cumulant should behave near a KT type phase transition [72]. For studies related to dimer models for example the Binder ratio does not show a crossing for the complex columnar order

parameter of Eq. 4.2 [47, 49]. However, the Binder ratio for the dimer symmetry breaking order parameter D does show a clear crossing [47, 49, 31, 73]. We show in Fig. 4.2 B_D for various system sizes $L = 12, 16, 20, 24$ and estimate the transition temperature $T_c \sim 3.1t$. Performing similar analysis for other values of V , we estimate the phase boundary of the columnar ordering, shown by blue points in Fig. 4.1. Our QMC simulations fail to equilibrate in $V/t \in]-0.5, 1[$ where the transition temperatures are lower but we expect the same picture to hold.

We cannot rule out the possibility of a transition to a mixed phase since D is also non-zero for this phase. We therefore also look at $\langle \cos(4\theta) \rangle$ which should be 1 only for the 4 columnar states and 0 in the disordered phase. In Fig. 4.2 we show $\langle \cos(4\theta) \rangle$ for different system sizes at $V/t = -5$ and we indeed observe that it reaches 1 at low temperature. We therefore conclude that in the range $V \leq -0.5$, to the lowest temperature accessible by our simulations the ordered phase is columnar.

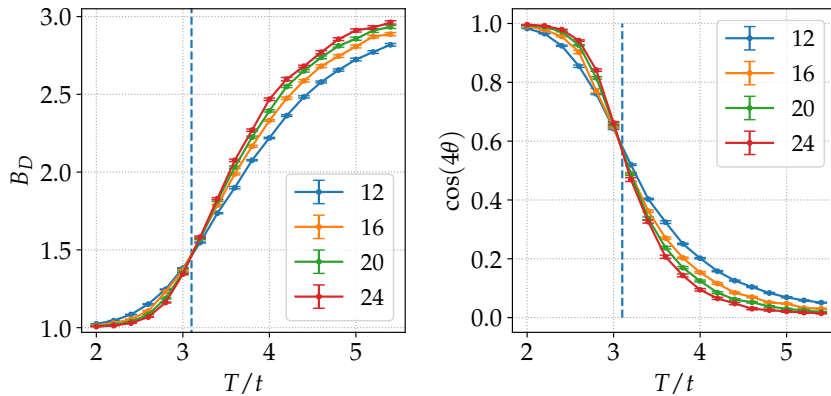


Figure 4.2: The plot on the left shows the Binder ratio B_D at $V/t = -5$ for system sizes $L = 12, 16, 20, 24$. The plot of the right shows $\langle \cos(4\theta) \rangle$ at the same $V/t = -5$ for various system sizes. Interestingly, $\langle \cos(4\theta) \rangle$ also shows a crossing like in B_D at the same $T \sim 3.1t$ which is marked by a vertical dashed line.

4.1.3 Staggered side $V/t > 1$

We follow a similar analysis for $V/t > 1$ where we expect a staggered ordering at low temperature. We monitor the Binder cumulant of $|W|$:

$$B_{|W|} = \frac{\langle |W|^4 \rangle}{\langle |W|^2 \rangle^2} \quad (4.6)$$

to estimate the transition temperature. Fig. 4.3 shows $B_{|W|}$ for system sizes $L = 12, 16, 20, 24, 32$ at $V/t = 2$ and $V/t = 5$. We note that there is a single crossing point for

sizes $L = 12, 16, 20$, the crossing however shifts toward lower temperature for $L = 24, 32$. As we argue below, this likely due to finite size effects which would disappear at larger system sizes which are currently not accessible to our QMC simulations. In Fig. 4.4 we show the behaviour of $B_{|W|}$ for the CIDM where we can reach much larger system sizes. We observe that the critical temperature is slightly higher (by about 10%) than that obtained from the system sizes $L = 12...32$. We expect a similar finite size effect in the QDM which is why we put an increased error bar for the phase boundary in Fig. 4.1. Finally, we note that the value of $B_{|W|}$ (the y axis value) at the crossing is in the same vertical range for both values of V/t in the QDM and also for the CIDM. This suggests that the finite temperature transitions on the staggered side in QDM and the CIDM lie in the same universality class, which was shown to be continuous and possibly of Ising type in Ref. [31].

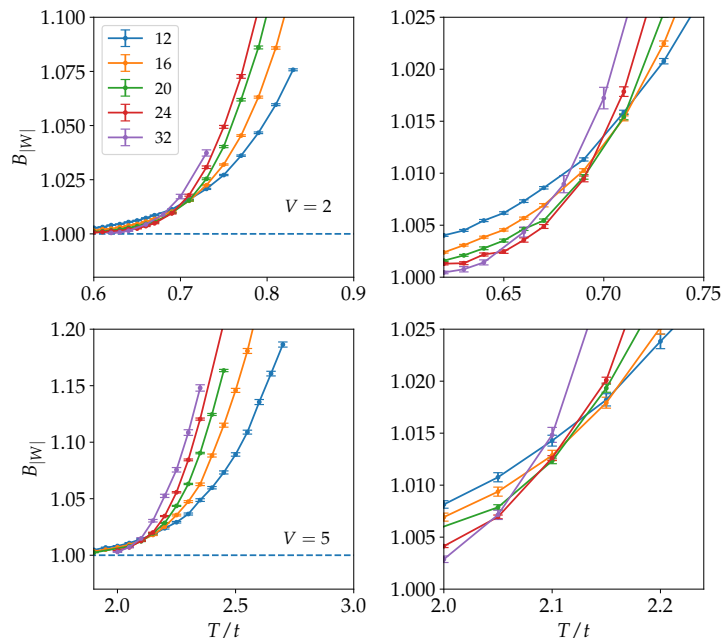


Figure 4.3: The two panels on the left show $B_{|W|} \rightarrow 1$ at low temperature for $V/t = 2, 5$. The panels on the right zoom in near the crossing point demonstrating the shift in the crossing to lower temperature for $L = 32$.

4.1.4 Critical phase

To study the high temperature critical phase we will look closely at the variation of the Coulomb gas constant $g(T, V)$ obtained from two different methods: i) by measuring the fluctuations of the square of winding numbers $\langle W^2 \rangle = \frac{1}{2}(\langle W_x^2 \rangle + \langle W_y^2 \rangle)$ as defined in

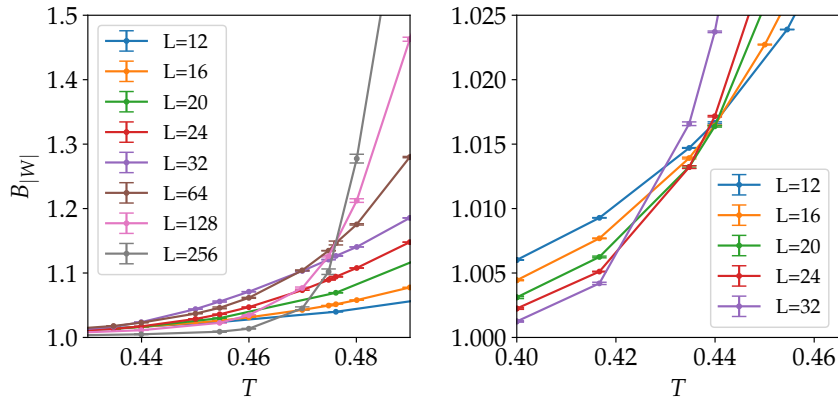


Figure 4.4: The panel on the left shows $B_{|W|}$ for CIDM reaching to system sizes of $L = 256$. The right panel shows a zoom in near the crossing for the same system sizes as the QDM. The panel on the right displays the same finite size behaviour as the QDM.

Eq. 2.8 and ii) by directly probing the dimer-dimer and monomer-monomer correlations.

Fluctuations of winding number : Let us look at the variation of $\langle W^2 \rangle$ and consequently g with temperature T for different values of V . Before moving to the results let us recall the limiting values of g which we already know from the CIDM. In the non interacting limit (free fermion point) we know from exact results that $g(T = \infty) = 1/2$. We also know from the mapping to the coarse grained action Eq. 2.5 that at the KT phase transition to the columnar phase $g(T = T_c) = 4$. From Eq. 2.8, we can also estimate the limiting values of $\langle W^2 \rangle$ at $g(T = \infty)$ and $g(T = T_c)$. For $g(T = \infty) = 1/2$, $\langle W^2 \rangle \sim 0.30343$ and for $g(T = T_c)$ the fluctuations of $\langle W^2 \rangle$ are extremely small, $\langle W^2 \rangle \sim O(10^{-6})$. It is not feasible to reach such accuracy in Monte Carlo simulations to be able to distinguish from the ordered phases (columnar/mixed) where $\langle W^2 \rangle = 0$. Already at $g = 2$, $\langle W^2 \rangle \simeq O(10^{-3})$. Because of this, we are not able to accurately estimate g near the columnar phase boundary in Fig. 4.1.

Fig. 4.5 shows the variation of $\langle W^2 \rangle$ and g vs temperature T for different values of V . We will divide this analysis in three regions. Let us begin with the range $V/t < 0$, shown in blue curves in Fig. 4.5. In this range the winding fluctuations decrease monotonically from their high temperature value $\langle W^2 \rangle \simeq 0.30343$ to the low temperature ordered phase where $\langle W^2 \rangle = 0$. Consequently, the Coulomb gas constant g varies from $g = 1/2$ to $g = 4$. In the range $V/t > 1$ shown in green, the winding fluctuations (Coulomb gas constant) increase (decrease) monotonically as we go to low temperature where there is a transition to the staggered ordering. At the RK point $V/t = 1$ we see a similar behaviour at finite temperature, even though we know that $g(T = 0) = 1/2$. Finally, in the intermediate range of $0 \leq V/t < 1$ (colour coded in red) we observe an interesting non-monotonic behaviour. We observe that the winding number fluctuations (Coulomb gas constant) start increasing (decreasing) as we lower the temperature but eventually show a downturn (upturn) after which they decrease (increase) to their limiting values

for the ordered states. This behaviour is most pronounced for $V/t = 0.3, 0.5, 0.6$ as seen in Fig. 4.5.

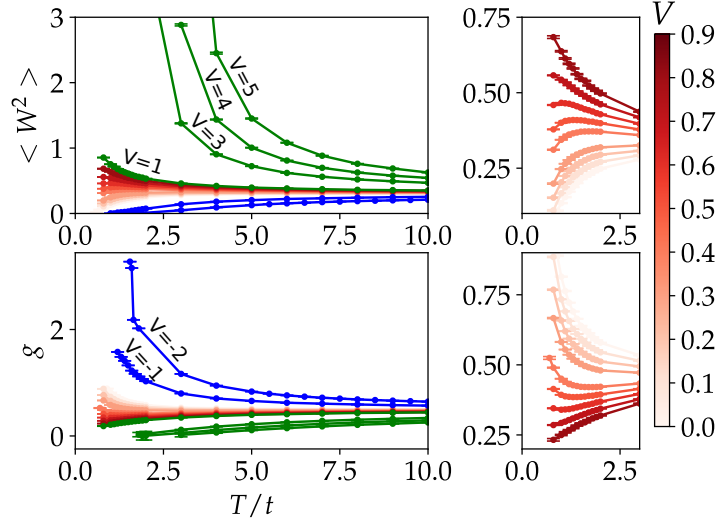


Figure 4.5: Variation of $\langle W^2 \rangle$ and g as a function of temperature T/t for different values of V/t . All the red curves show the values of $0 \leq V/t < 1$ where the reentrance effect is seen, the blue curves show $V/t < 0$ and the green curves show $V/t \geq 1$. The panels on the right emphasize the reentrance region where the Coulomb gas constant varies non-monotonically with temperature. This data was obtained from QMC simulations on system size $L = 24$.

Correlation functions : We can also measure the Coulomb gas constant by directly probing the equal time dimer-dimer and monomer-monomer correlators similar to what we saw in the case of CIDM. Let us begin by defining the three types of correlators we will be looking at

(i)The longitudinal dimer-dimer correlations:

$$G^l(x) = \langle d^{\bullet-}(\mathbf{r})d^{\bullet-}(\mathbf{r} + (x, 0)) \rangle - \langle d^{\bullet-} \rangle^2 \quad (4.7)$$

(ii)The transverse dimer-dimer correlations:

$$G^t(x) = \langle d^{\bullet-}(\mathbf{r})d^{\bullet-}(\mathbf{r} + (0, x)) \rangle - \langle d^{\bullet-} \rangle^2 \quad (4.8)$$

(iii)The monomer-monomer correlations:

$$M(x) = \langle m(\mathbf{r})m(\mathbf{r} + \mathbf{x}) \rangle \quad (4.9)$$

For the two dimer-dimer correlators we subtract the dimer density $\langle d^{\bullet-} \rangle^2 = 1/16$. For the monomer-monomer correlator, $m(\mathbf{r}) = 1$ if there is a monomer at site \mathbf{r} and 0 otherwise. As discussed in the case of CIDM the dimer-dimer correlations contain two leading contributions, a so called dipolar part which decays as $1/x^2$ and a vertex part which decays

as $1/x^{1/g}$. The long distance behaviour will thus be dominated by the smallest exponent, $\min(2, 1/g)$. On the other hand we expect the monomer-monomer correlator to have no dipolar part and the leading contribution to decay as $1/x^g$.

We summarize our calculations in Fig. 4.6, where we measure $G^l(x)$, $G^t(x)$ and $M(x)$ for various values of V/t . We set the temperature $T/t = 4$ and use $L = 64$ as our system size. Our correlators are symmetric about $L/2$ due to periodic boundary conditions. Since in the critical phase the action Eq. 2.5 is a free boson CFT we also perform conformal rescaling $x \rightarrow \frac{L}{\pi} \sin(\pi x/L)$ and fit our correlators in the range $x = [1, L/5]$. In the final panel of Fig. 4.6 we compare the exponents obtained by fitting the above three types of correlators. We plot the inverse of the exponent of the two dimer-dimer correlators as we can then compare them to the g obtained from the monomer correlations and fluctuations of the winding number. We see an overall good agreement between the estimates of g for $g > 1/2$ whereas for $g < 1/2$ the dimer-dimer correlators saturate around the value $1/2$ as the leading contribution now comes from the dipolar part.

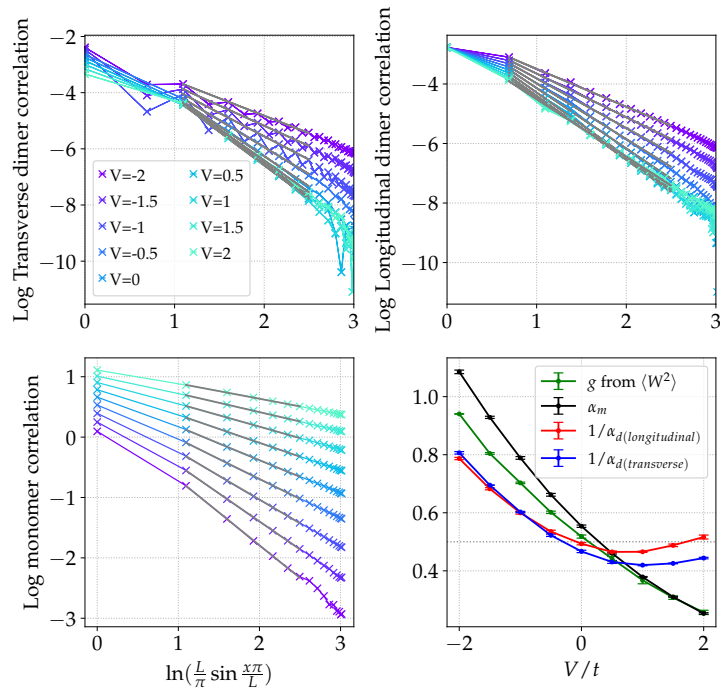


Figure 4.6: Top-left, top-right and bottom-left panels show the correlators $G^t(x)$, $G^l(x)$ and $M(x)$ respectively. The correlators are shown as a function of conformal distance $L/\pi \sin(\pi x/L)$ and in log-log scale to show the power-law behaviour. The grey lines show the power-law fits. The transverse correlator clearly shows an even-odd effect for short distances. The bottom-right panel shows a comparison of the Coulomb gas constant g obtained from fluctuations of the winding number with the exponents obtained by fitting the correlators. This data was obtained for $T/t = 4$ and system size $L = 64$.

The agreement is however not perfect and we expect this is due to finite size effects. To check our assumptions we perform the same analysis for the CIDM where we are able to reach much larger sizes. Fig. 4.7 shows a similar comparison of exponents at system

size $L = 64$ and $L = 256$ for the CIDM. The comparison shows that the values of g obtained from the fluctuations of winding number at $L = 64$ are closer to those obtained at $L = 256$ than the ones obtained from the different correlators. We can hence conclude that the fluctuations of winding number show much less finite size effects than the different correlators, for measuring g . This is why we rely on $\langle W^2 \rangle$ to show g in the phase diagram in Fig. 4.1.

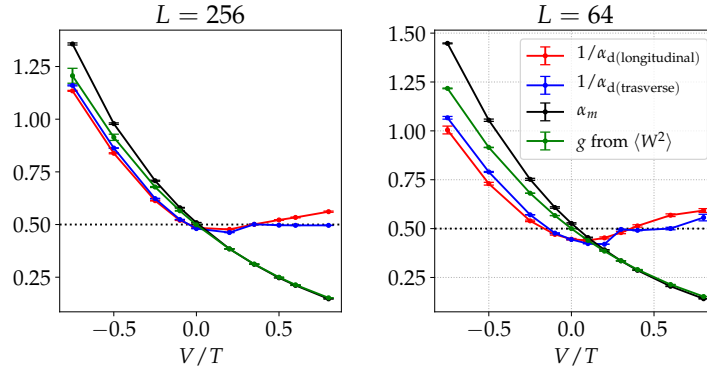


Figure 4.7: A comparison of exponents similar to Fig. 4.6 but now for the CIDM. The two panels show two different system sizes $L = 256$ and $L = 64$, demonstrating that the estimates of g obtained from the real space dimer-dimer and monomer-monomer correlators are more susceptible to finite size effects than those obtained from $\langle W^2 \rangle$.

4.2 High Temperature Expansion

In this section we will see how we can explain the variation of the Coulomb gas constant in the high temperature range that we observed through our simulations by a high temperature expansion argument. Since at high temperature the QDM is expected to be captured by classical effects, the crux of the argument is to find an equivalent CIDM for the QDM ¹.

Let us consider a CIDM where we associate an energy W to any plaquette with parallel dimers such that for a dimer configuration c the total energy $E_c = W N_c^f$, where $N_c^f = N(\text{horizontal dimer}) + N(\text{vertical dimer})$, similar to Eq. 2.4 with W instead of V to distinguish it from the QDM case.

Consider an operator O which is diagonal in the dimer configuration basis, $\langle c|O|c \rangle = O_c$. Expanding its unordered expectation value for the QDM in powers of $\beta = 1/T$, we have :

$$\text{Tr}[Oe^{-\beta H_{QDM}}] \sim \text{Tr}[O] - \beta \text{Tr}[OH_{QDM}] + \frac{\beta^2}{2} \text{Tr}[OH_{QDM}^2] - O(\beta^3) \quad (4.10)$$

¹We are grateful to G. Misguich for suggesting this argument

Since the observable is diagonal in the computational basis we have :

$$\begin{aligned}\text{Tr}[O] &= \sum_c O_c \\ \text{Tr}[OH_{QDM}] &= \sum_c \langle c|OH_{QDM}|c\rangle = \sum_c O_c V N_c^f \\ \text{Tr}[OH_{QDM}^2] &= \sum_c \langle c|OH_{QDM}^2|c\rangle = \sum_c O_c [V^2(N_c^f)^2 + t^2(N_c^f)^2]\end{aligned}\tag{4.11}$$

We can then rewrite Eq. 4.10 as :

$$\text{Tr}[Oe^{-\beta H_{QDM}}] \sim \sum_c O_c + \sum_c O_c N_c^f [-\beta V + \frac{\beta^2 t^2}{2} + \frac{\beta^2 V^2}{2} N_c^f] + O(\beta^3)\tag{4.12}$$

Performing a similar expansion for the CIDM we have :

$$\sum_c Oe^{-\beta E_c} \sim \sum_c O_c + \sum_c O_c N_c^f [-\beta W + \frac{\beta^2 W^2}{2} N_c^f] + O(\beta^3)\tag{4.13}$$

Comparing the terms in the above two expansions, we can identify W with $V - \beta t^2/2$ up to an error of $O(\beta^3)$. This implies that the physics of the QDM (which includes the Coulomb gas constant g) at high temperature is the same as that of a CIDM with the interaction strength $W = V - 1/2T$, where we have set $t = 1$. To sum up, we expect

$$g_{QDM}(V, T) = g_{CIDM}(W = V - \frac{1}{2T}, T)\tag{4.14}$$

We can verify this by performing simulations of CIDM for a range of parameters (V, T) and calculate $g_{CIDM}(W, T)$. We show this in Fig. 4.8 for system size $L = 24$, to be consistent with the system size used in the phase diagram of the QDM. We then use Eq. 4.14 to infer g_{QDM} as is shown by the cyan lines in Fig. 4.8.

These contours in cyan shown an excellent match with the black contours obtained from the QMC simulations to temperatures down to $T \sim 1.5$. It also shows why the asymptotic $g = 1/2$ line is to the right of $V = 0$. As $g = 1/2$ corresponds to the non interacting limit of the CIDM where $W = 0$, the $g = 1/2$ contour should follow the equation $T = 1/2V$. Overall, this argument provides a good account of the high temperature behaviour and also hints at the reentrance effect which we observe in the QDM for $V > 0$.

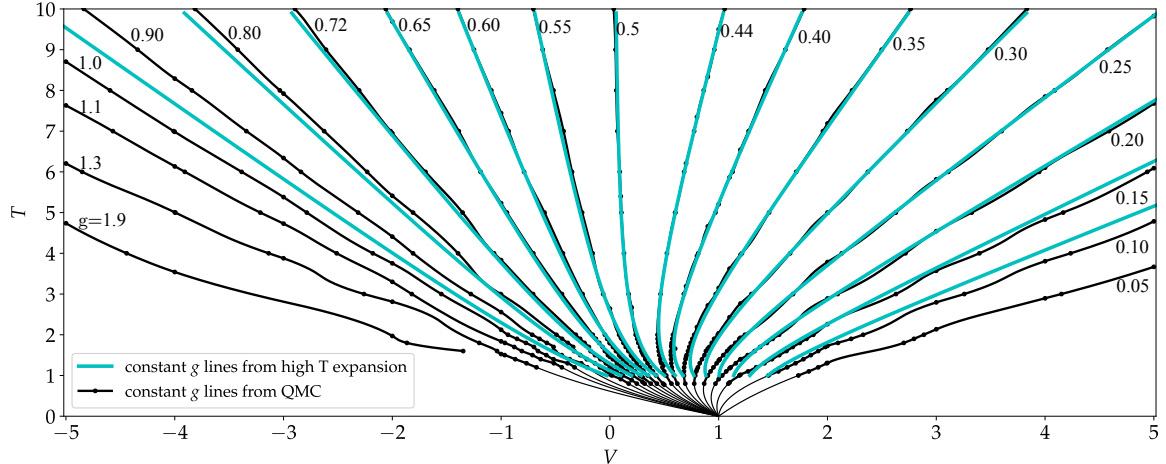


Figure 4.8: Comparison between the constant- g lines obtained from QMC simulations (shown by black lines with dots) and those obtained by simulating an equivalent CIDM from the high temperature expansion (shown in cyan lines).

4.3 Discussion and Perspectives

This work opens up the possibilities of exploring the finite temperature melting of ordered phases in other constrained quantum models. For example, it would be interesting to understand the melting of the 'devil's staircase' [56] of commensurate and incommensurate phases which is argued to be present in the zero temperature phase diagram of the QDM on the honeycomb lattice [74]. Also exploring the finite temperature phase diagrams of the QDM on cubic and diamond lattices which are shown to host a Coulomb phase, is an interesting path [41, 42, 43].

A non trivial task on the algorithmic side, would be to reach even lower temperature while keeping the Monte Carlo simulation ergodic.

As discussed in the beginning of the chapter the ground state phase diagram of the QDM on the square lattice is still not fully settled. The problem in drawing a fair conclusion seems to be the very faint signals in the order parameters used to distinguish the mixed and plaquette phases. A possible probe to distinguish the two phases could be - *Fidelity Susceptibility*. The divergence of this quantity has been used successfully to capture quantum phase transitions in various models amenable to Quantum Monte Carlo methods [75, 76]. Since it was shown that fidelity susceptibility has an easy to implement estimator in an SSE setup, it could be easily incorporated in our Sweeping cluster algorithm.

Chapter 5

Interacting loop model on the square lattice

The previous chapter sets up a precedent to study classical equivalents of quantum models to explore their finite temperature phases and phase transitions. Especially for RK type Hamiltonians, study of a classical model is important because of the 'classical' nature of the RK point.

In this chapter, we study a two-dimensional classical statistical mechanics model of fully-packed loops which attract locally. With the help of a directed-loop Monte Carlo algorithm (introduced in Chapter 3) [67, 48, 64, 65, 66, 77] and a Coulomb gas construction [12] formulated in terms of a height-field description of the loop constraint [78, 79], we obtain evidence for the existence of a finite temperature Kosterlitz-Thouless transition separating a high-temperature critical phase from a low-temperature nematic phase.

Besides their interest in two-dimensional statistical mechanics in extending previous works on loop models [80, 12, 81, 82, 83], the results presented in this chapter are also relevant for quantum-constrained models. First, the ground-state wave function at a Rokhsar-Kivelson point [8] (or its generalizations [84, 85]) in the phase diagram of quantum loop models (QLM) maps to the partition function of a classical loop model. In addition, the phase diagram of the classical model and the methods we use in its inference can serve to guide us in mapping out the finite-temperature phase diagram [86] and transitions of the quantum loop model [87, 88, 89] (as we studied in the previous chapter). Such quantum-constrained models host a rich set of phases [38, 90, 91, 92, 93] and have recently been shown to be relevant in the context of Rydberg atom arrays [94, 21, 20], where the Rydberg blockade effectively implements the loop or dimer constraint (as described in the introduction of the thesis).

We will begin the chapter by defining the partition function and the low temperature

ordered states of the model in section (5.1). In section (5.2), we will describe the model from a field-theoretic point of view. This is followed in section (5.3) by verifying the predictions for the phase transition from field theory through Monte Carlo simulations. Finally, we conclude in section (5.4) by giving some future directions and open questions.

5.1 The model

Let us begin by defining the configuration space for the model. Similar to the dimer model we looked at in the previous chapter, we again consider a constrained configuration space which consists of **closed packed non-intersecting loops** on the square lattice with periodic boundary conditions. As shown in Fig. 5.1, if we assign an outgoing arrow to every loop segment connecting sublattice A to B and an incoming arrow to every empty link connecting sublattice A to B (or vice-versa), the configurations map exactly to the configurations of the six-vertex model [15, 95, 14, 96, 97, 98].

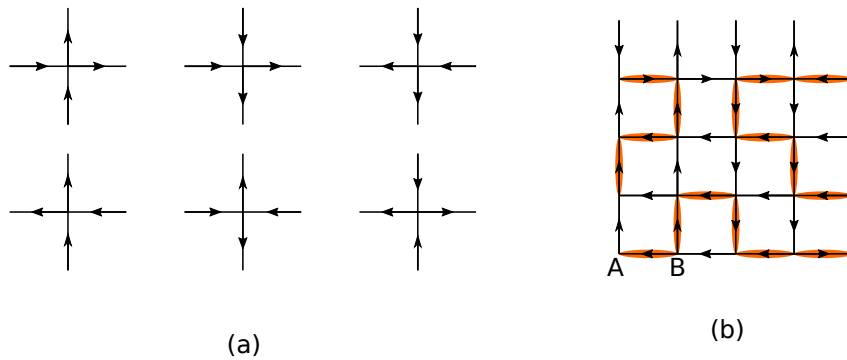


Figure 5.1: (a) shows the six possible configurations at each site of the square lattice for the six-vertex model - two arrows pointing in and two pointing out. In the non-interacting limit this mapping is exact with all the six configurations having equal fugacities(ice point). (b) shows the mapping between close packed loop segments and the six vertex configurations.

Loop or vertex models often associate a fugacity with each closed loop or to each type of vertex respectively, to define the corresponding partition function [80]. We are however interested in the interacting loop model where we associate an energy V to plaquettes with parallel loop segments. We define the following partition function

$$Z = \sum_c e^{-\beta E_c} \tag{5.1}$$

$$E_c = V(N(\text{⬢}) + N(\text{⬢}))$$

where the summation is over all closely packed loop configurations c and we assign an energy E_c which depends on the total number of plaquettes with parallel loop segments, here $N(\square)$ and $N(\blacksquare)$ denote the number of flippable plaquettes. There is no energy cost associated to plaquettes with more than two loop segments. We focus on the case of $V = -1$ which corresponds to attractive interactions between loop segments.

Similar to the dimer case [47, 48] we expect low temperature ordered states depending on the sign of V . For $V < 0$, the configurations which minimize the energy ($E_0 = -L^2$) are nematic ordered states, Fig. 5.2 which break $\pi/2$ rotation symmetry. For $V > 0$, the minimum energy configurations ($E_0 = 0$) are those with no parallel plaquettes which form the staggered ordered states, Fig. 5.15. In the non-interacting limit the loop configurations map to the six vertex model at ice-point with equal fugacities for all vertices which is **critical** with power-law correlators. We hence expect phase transitions out of this critical phase to the above ordered states at some finite temperature. We will show below for the *attractive* case ($V = -1$) that this phase transition is of Kosterlitz-Thouless type.

We study the finite temperature phase diagram of the model using directed loop Monte carlo simulations (described in Chapter 3) supplemented by some field theoretical arguments.

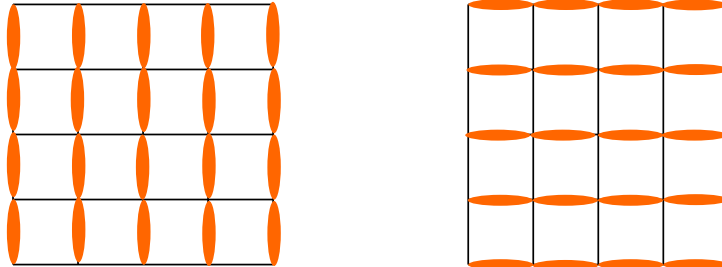


Figure 5.2: The two degenerate nematic orderings which break $\pi/2$ rotation symmetry.

5.2 Field theoretical description

In this section we will give our expectations for the finite temperature phase diagram of the model through field theoretical arguments. The analysis follows along the similar lines of the Classical Interacting Dimer Model [47, 48] with a few subtle changes because of different constraints and broken symmetries. We highlight these changes in our analysis.

5.2.1 Height Mapping

To construct a coarse grained theory out of the microscopic loop configurations we again resort to a height mapping, similar to the previous chapter. We assign a height z to every plaquette of the square lattice with the following rule: going clockwise around sublattice-A the height increases by $1/2$ ($z \rightarrow z + 1/2$) when crossing a link with a loop segment while the height decreases by $1/2$ ($z \rightarrow z - 1/2$) when crossing an empty link, see Fig. 5.3. In the thermodynamic limit, the loop configurations could be mapped to a continuous height field $h(\mathbf{r})$ obtained by averaging the heights z from neighbouring plaquettes.

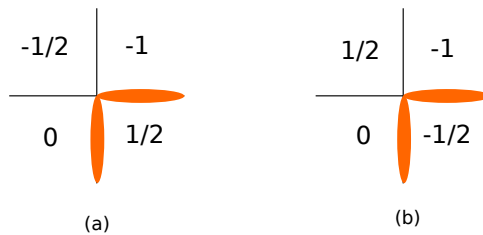


Figure 5.3: Example of height mapping around a site of the square lattice. (a) shows the mapping around the site belonging to sublattice A and (b) shows the mapping for sublattice B for the same loop configuration.

5.2.2 Sine-Gordon action revisited

Since our microscopic model is local, we must ensure this also holds for the effective coarse grained action to be constructed. Consider a continuum height field $h(\mathbf{r})$ within an enclosed area A . To ensure locality in our action, we need to make sure that any changes in the loop configurations outside A do not affect the height field $h(\mathbf{r})$ inside. At the microscopic level however, one can see that if we make any loop changes along a closed loop encircling the region A it changes the microscopic heights $z(\mathbf{r})$ inside A by 1, this is demonstrated with an example in Fig. 5.4. This indicates that the physical action should be invariant under $h \rightarrow h \pm 1$ (similar argument as for the dimer model [48]).

We expect the effective action to be of Sine-Gordon type similar to what we saw in the previous chapter for the dimer model.

$$S = \int d^2r [\pi g (\nabla h(\mathbf{r}))^2 + \mathcal{V} \cos(4\pi h(\mathbf{r}))] \quad (5.2)$$

with $\mathcal{V} > 0$. Here g is the Coulomb gas constant which will vary with temperature. $g(T = \infty) = 1/3$, because the ice point of the six vertex model corresponds to a XXZ spin

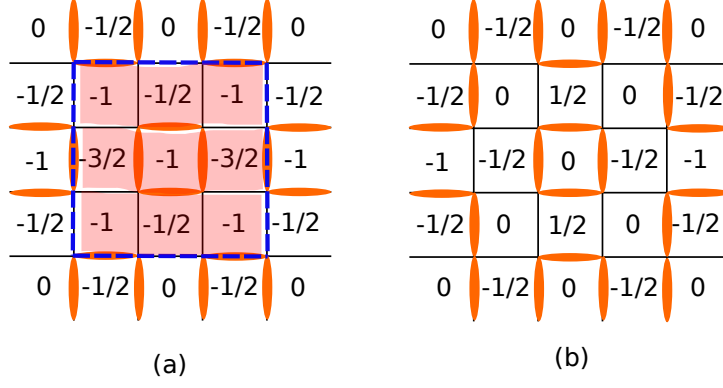


Figure 5.4: (a) shows a typical closed packed loop configuration with microscopic heights z assigned to every plaquette. The blue dashed loop shows a closed path along which the loop segment occupation is switched. As one can see in (b), the new configuration has microscopic heights z changed by 1 only for the region enclosed by the blue loop (shown by the red shaded area in (a)).

chain at $\Delta = 1/2$ in notations where $\Delta > 0$ corresponds to ferromagnetic interactions and the value of g is given by $\Delta = \cos(\pi g)$, see e.g. [99, 100]. The gradient term as usual favours flat height configurations while the cosine term now has two minima at $h(r) = \pm 1/4$ which correspond to the two nematic orderings. The \mathcal{V} can also depend on temperature but its exact dependence is not relevant as long as it stays positive such that the two nematic states are favoured.

Let us now look at the Coulomb gas description of this model. We identify the continuum description of the microscopic loop/dimer segment operators from [79] as:

$$n_{\mathbf{-}} - 1/2 = (-1)^{x+y+1} \nabla_y h - \frac{X}{2i} (\exp(2\pi i h) - h.c.) \quad (5.3)$$

$$n_{\mathbf{+}} - 1/2 = (-1)^{x+y} \nabla_x h + \frac{X}{2i} (\exp(2\pi i h) - h.c.) \quad (5.4)$$

The loop segment operators are thus composed of two parts, a gradient part and a vertex part. Due to the periodicity in heights ($h = h + 1$) the vertex part is expressed in harmonics of $2\pi h$ and the microscopic $\pi/2$ rotations of the model give $h \rightarrow -h$ and $h \rightarrow h + 1/2$. The loop segment operators hence correspond to electric charge $e = 1$. The cosine term in the action corresponds to an electric charge $e = 2$ and therefore has a scaling dimension $\alpha(2, 0)/2 = 2/g$. This indicates that the cosine term becomes relevant at $g \geq 1$.

The above identification of the loop segment operators in the continuum will enable us to construct the forms of the leading terms for the following three correlators:

$$C^L(\mathbf{r} = (x, y)) = \langle n_{\mathbf{-}}(0) n_{\mathbf{-}}(\mathbf{r}) \rangle - 1/4 = (-)^{x+y} A \frac{x^2 - y^2}{(x^2 + y^2)^2} + \frac{B}{(x^2 + y^2)^{1/2g}} \quad (5.5)$$

$$C^T(\mathbf{r} = (x, y)) = \langle n_{\mathbf{1}}(0)n_{\mathbf{1}}(\mathbf{r}) \rangle - 1/4 = (-)^{x+y} A \frac{y^2 - x^2}{(x^2 + y^2)^2} + \frac{B}{(x^2 + y^2)^{1/2g}} \quad (5.6)$$

$$C^C(\mathbf{r} = (x, y)) = \langle n_{-}(0)n_{\mathbf{1}}(\mathbf{r}) \rangle + \langle n_{\mathbf{1}}(0)n_{-}(\mathbf{r}) \rangle - 1/2 = (-)^{x+y} A \frac{2xy}{(x^2 + y^2)^2} - \frac{B}{(x^2 + y^2)^{1/2g}} \quad (5.7)$$

Here the coefficient $A = 1/(4g\pi^2)$ comes from the correlators of the gradient parts of Eqs. (5.3) and (5.4). This correlator ($\langle \nabla_{x/y} h(r) \nabla_{x/y} h(r') \rangle$) is exactly evaluated for a free compact boson conformal field theory [101]. We also have $B = X^2/2$, however, its dependence on g is not universal. At $T = \infty$, exact expressions for the XXZ spin chain [99] give $B \simeq 0.01795$, see Table 1 in Ref. [99] (see also Ref. [102]). Note that further subleading terms could be present [99].

We can also define monomers in our model by breaking only **one** loop segment at a lattice site. This creates dislocations of ± 1 in the height field. The monomers in our theory would correspond to a magnetic charge $m = 1$ and would decay as : $M(r) \sim r^{-g}$. We end this section with a comparison of the Coulomb gas construction between dimers and loops.

Comparison of Coulomb gas construction		
	Dimers	Loops
Electromagnetic charge $\alpha(e, m)$	$\alpha(1, 0)$	$\alpha(1, 0)$
Electromagnetic charge for the low temperature order parameter	$\alpha(4, 0)$	$\alpha(2, 0)$
$g(T = \infty)$	1/2	1/3
$g(T = T_{KT})$	4	1

5.3 Phase Diagram

Let us summarize our predictions of the phase diagram in Fig. 5.5. We expect a Kosterlitz Thouless type phase transition at some finite temperature out of the critical phase to a two fold degenerate nematic ordered state which spontaneously breaks $\pi/2$ rotation symmetry. We also expect the Coulomb gas constant g to vary with temperature. From the one to one mapping to the six vertex model at infinite temperature, we expect $g(T = \infty) = 1/3$ and from the field theory arguments of the previous section, we also predict $g(T = T_{KT}) = 1$.

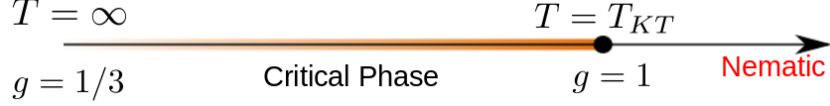


Figure 5.5: Phase diagram of the interacting loop model on the square lattice with attractive interactions $V = -1$. $T_{KT} = 1.425(1)$ is estimated by Monte Carlo simulations.

Let us now define the observables monitored to verify our above predictions.

Winding number fluctuations: Every closely packed loop configuration can be labelled by two integer winding numbers W_x and W_y (defined in the same way as in the previous chapter). Even though $\langle W_x \rangle$ and $\langle W_y \rangle$ vanish due to translation symmetry, their fluctuations, Eq. 5.8, are non zero

$$\langle W^2 \rangle = \frac{\langle W_x^2 \rangle + \langle W_y^2 \rangle}{2} \quad (5.8)$$

Let us reiterate the relation between $\langle W^2 \rangle$ and the Coulomb gas constant g .

$$\langle W^2 \rangle = \frac{\sum_{n \in \mathbb{Z}} n^2 e^{-\pi g n^2}}{\sum_{n \in \mathbb{Z}} e^{-\pi g n^2}} \quad (5.9)$$

Nematic order parameter: We can identify the low temperature phase through the rotational symmetry breaking, nematic order parameter

$$D = \frac{1}{N} |N_{\mathbf{-}} - N_{\mathbf{I}}|, \quad (5.10)$$

with $N_{\mathbf{-}} = \sum_{\mathbf{r}} n_{\mathbf{-}}(\mathbf{r})$ and $N_{\mathbf{I}} = \sum_{\mathbf{r}} n_{\mathbf{I}}(\mathbf{r})$, where $n_{\mathbf{-}}(\mathbf{r}) = 1$ if a horizontal loop segment occupies the edge between \mathbf{r} and $\mathbf{r} + (r, 0)$ and it is zero otherwise. Similarly, $n_{\mathbf{I}}(\mathbf{r}) = 1$ if a vertical loop segment occupies the edge between \mathbf{r} and $\mathbf{r} + (0, r)$ and it is zero otherwise. This order parameter is 1 for the two nematic states while it is 0 in the disordered phase.

Loop segment correlators: We also consider the connected correlators between loop segments $C_{\alpha, \beta}(\mathbf{r}) = \langle n_{\alpha}(0) n_{\beta}(\mathbf{r}) \rangle - \langle n_{\alpha} \rangle \langle n_{\beta} \rangle$, where α and β can be $\mathbf{-}$, \mathbf{I} . Since there are two loop segments at each vertex, in the disordered phase $\langle n_{\alpha} \rangle = 1/2$ and $\langle n_{\alpha} \rangle \langle n_{\beta} \rangle = 1/4$. In Monte Carlo simulations, we average over all possible initial positions $\mathbf{0}$ of the first loop segment, as well as all equivalent pairs α, β . The three types of correlators we consider are shown in Eqs. 5.5, 5.6 and 5.7. We also consider the correlator associated to the nematic order parameter

$$\langle D(0)D(r) \rangle = \langle (n_{\mathbf{-}}(0) - n_{\mathbf{I}}(0))(n_{\mathbf{-}}(r) - n_{\mathbf{I}}(r)) \rangle = C^L(r) + C^T(r) - C^C(r) \quad (5.11)$$

5.3.1 Fluctuations of winding numbers

In Fig. 5.6a, we show the variation of $\langle W^2 \rangle$ with temperature T for different system sizes L . Field theory analysis predicts the KT transition to occur at $g = 1$. Using $g = 1$ in Eq. 5.8, we can show that the critical value of $\langle W^2 \rangle$ at the transition is exactly $\langle W^2 \rangle_c = 1/(4\pi)$ (see appendix A.1 for a derivation) which is shown by a grey dashed horizontal line in Fig. 5.6a.

We now estimate the value of the transition temperature $T_{KT}(L)$ for each system size as the temperature where the winding number fluctuations cross the above critical value. To determine the transition temperature T_{KT} in the thermodynamic limit we use the following finite size scaling relation for a KT transition [103, 104, 31]:

$$\frac{1}{T_{KT}(L)} = \frac{1}{T_{KT}} + \frac{C}{\log(L/L_0)^2}, \quad (5.12)$$

where C is a constant. By fitting the estimated $T_{KT}(L)$ in Fig. 5.6b with Eq. 5.12 we obtain $T_{KT} = 1.425(1)$.

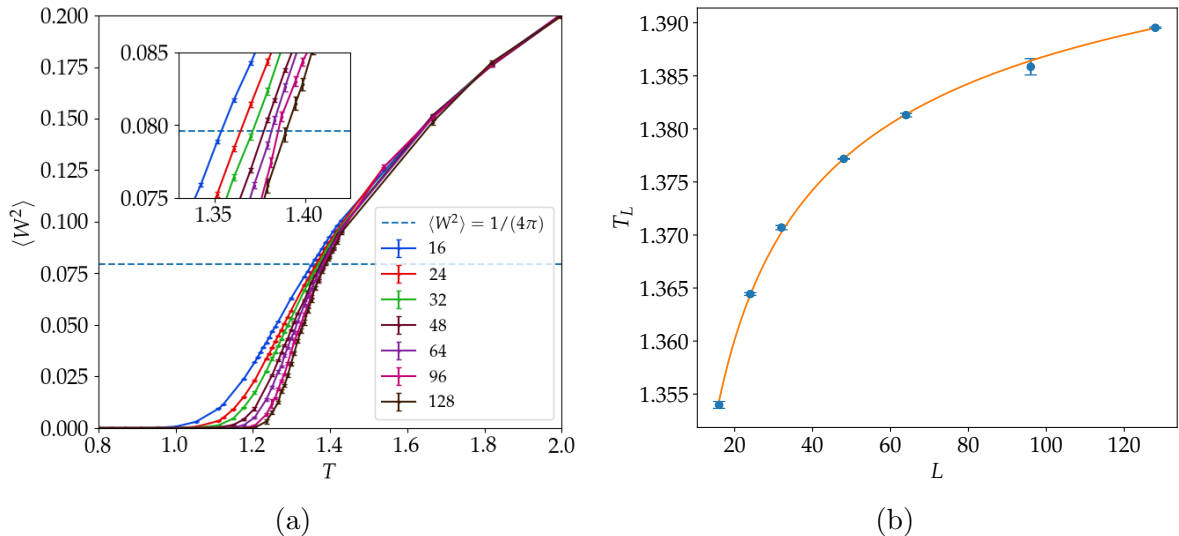


Figure 5.6: (a) shows the variation of $\langle W^2 \rangle$ with temperature for different system sizes. The blue dashed line shows the critical winding number fluctuations $\langle W^2 \rangle_c = 1/4\pi$, obtained exactly from Eq. 5.8 by setting $g = 1$. The inset is a zoom in where the curves cross the critical value. (b) shows the finite size scaling of the estimated transition temperature as a function of system size. The finite size data $T_{KT}(L)$ are obtained from (a) by noting the temperature where the $\langle W^2 \rangle$ curves intersect the critical value. The orange curve shows the fit to Eq. 5.12. The extrapolation to the thermodynamic limit gives $T_{KT} = 1.425(1)$.

5.3.2 Susceptibility of nematic order parameter

Fig. 5.7 shows the variation of the nematic order parameter $\langle D \rangle$ with temperature T for various system sizes. The finite value of $\langle D \rangle$ at low temperature clearly indicates a nematic ordering. $\langle D \rangle$ vanishes at high temperature in the thermodynamic limit.

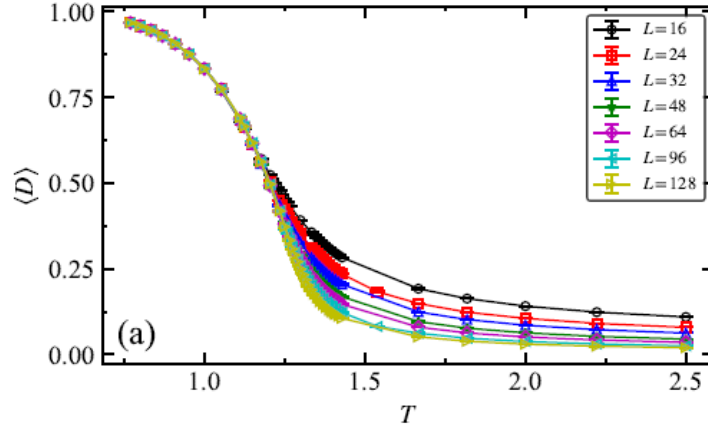


Figure 5.7: Variation of the nematic order parameter D , Eq. 5.10 with temperature for different system sizes.

We can also define the susceptibility for the nematic order parameter χ_D as:

$$\chi_D = N(\langle D^2 \rangle - \langle D \rangle^2) \quad (5.13)$$

Here N is the number of plaquettes in the square lattice. Fig. 5.8a shows a clear diverging peak (in system size) in the temperature range where we expect the phase transition to occur. The shift in temperature of the susceptibility peak with system size could be used to perform a data collapse in order to cross validate the transition temperature T_{KT} we estimated in the previous subsection. One can derive a finite scaling ansatz for χ_D (first used in [105]): using the fact that the nematic order parameter correlator, Eq. 5.11 goes as $\langle D(0)D(r) \rangle \sim r^{-\eta_D}$ with $\eta_D = 1/g$ (we verify this in later sections), we get

$$\chi_D = \int_0^L \langle D(0)D(r) \rangle d^2r \sim L^{2-\eta_D}. \quad (5.14)$$

Since near the KT transition the correlation length diverges as $\xi \sim \exp\left(\frac{K}{\sqrt{T-T_{KT}}}\right)$, in the vicinity of a KT transition, using the finite size scaling ansatz $\chi_D = L^{(2-\eta_D)} f(L/\xi)$ gives

$$\chi_D \sim L^{(2-\eta_D)} f\left[L \exp\left(\frac{-K}{\sqrt{T-T_{KT}}}\right)\right] \quad (5.15)$$

for $T > T_{KT}$. Here K is a constant and $\eta_D = 1/g_c = 1$ is the anomalous dimension [47]. To perform the collapse, we use the data in the region $T > T_{KT}$ and rescale the y axis as $\chi_D L^{-(2-\eta_D)}$ and the x axis as $L \exp\left(\frac{-K}{\sqrt{T-T_{KT}}}\right)$, as shown in Fig. 5.8b. Such data collapse has been used extensively before in the literature [103, 104, 106, 107, 108, 109, 110] to determine the Kosterlitz-Thouless transition temperature T_{KT} in many 2D systems. We see that the values $T_{KT} = 1.425$ and $\eta_D = 1$ provide a good data collapse, resulting in a good agreement with the T_{KT} obtained in the previous subsection.

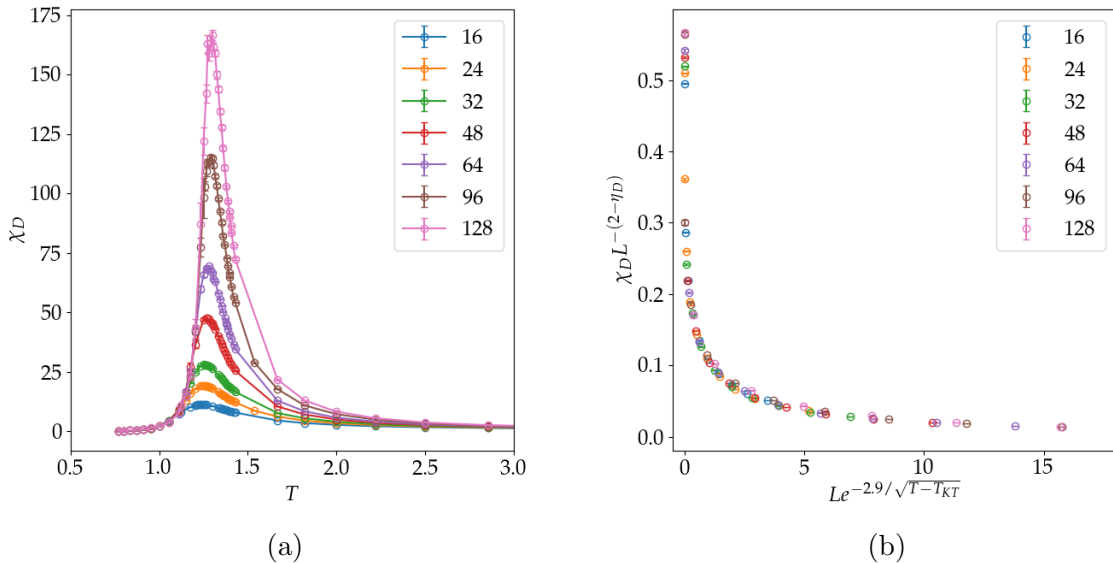


Figure 5.8: (a) shows the variation of the susceptibility χ_D of the nematic order parameter as a function of temperature for various system sizes. (b) shows the data collapse of the susceptibility in the critical phase with $T > T_{KT}$. We find a good collapse for the parameters $\eta_D = 1$ and $T_{KT} = 1.425$.

5.3.3 Correlation functions

In this subsection we verify the predictions for the correlation functions, whose leading terms were obtained from the field theoretic description in Eqs. 5.5, 5.6 and 5.7. Before directly fitting the correlators C^L and C^T , it is more instructive to consider their combinations which separate out the vertex and dipolar contributions. All the fits performed below are for Monte Carlo simulations on system size $L = 256$. These fits will be used to obtain the value of g later.

Let us first consider the sum $C^L + C^T = \langle n_{\mathbf{-}}(0)n_{\mathbf{-}}(\mathbf{r}) \rangle + \langle n_{\mathbf{1}}(0)n_{\mathbf{1}}(\mathbf{r}) \rangle - 1/2$ which should only contain the vertex contribution $2B/(x^2 + y^2)^{1/2g}$. We fit this combination for the direction $\mathbf{r} = (r, 0)$ in Fig. 5.9, shown in both linear (Fig. 5.9a) and log scales (Fig. 5.9b).

Consistent with the expected form, this combination shows a power-law scaling with distance r with an exponent which increases with temperature.

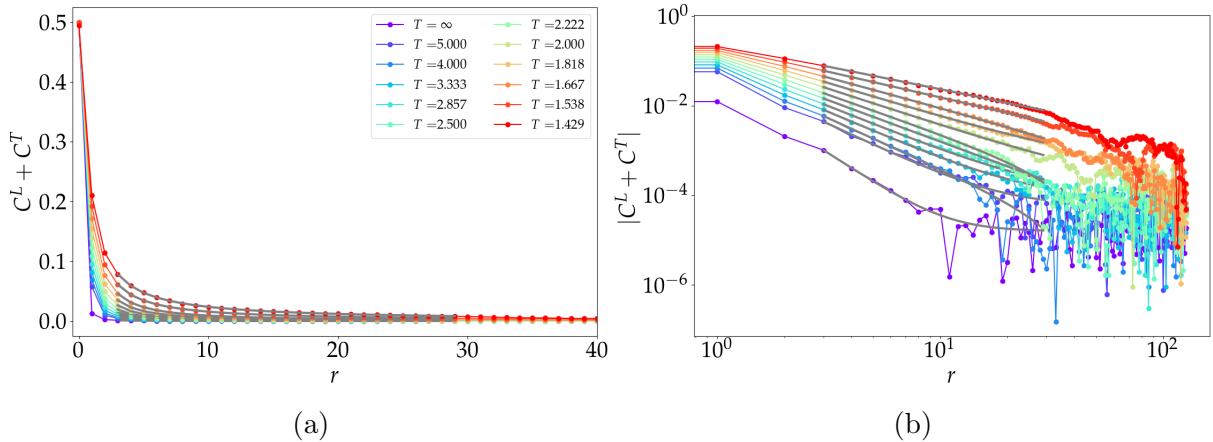


Figure 5.9: Equal time loop segment correlations (a) $C^L + C^T$ as a function of linear distance r , (b) log-log plot of $|C^L + C^T|$ (absolute value is used to correct for very small negative values occurring at large r , large T due to statistical fluctuations caused by Monte Carlo sampling). The system size used for both the correlators is $L = 256$. The grey curves are power-law fits to the scaling form $B'/r^{1/g}$.

Next, we consider the combinations $C^L - C^T = \langle n_{\mathbf{-}}(0)n_{\mathbf{-}}(\mathbf{r}) \rangle - \langle n_{\mathbf{+}}(0)n_{\mathbf{+}}(\mathbf{r}) \rangle$ which is expected to have only the staggered dipolar contribution $(-1)^r/r^2$. In Fig. 5.10 we plot $(-1)^r(C^L - C^T)$ in the direction $\mathbf{r} = (r, 0)$. From Fig. 5.10b, we can still see some staggered contribution which becomes more prominent as we approach the transition temperature. To account for this, instead of fitting just the staggered dipolar contribution we phenomenologically fit $C^L - C^T$ to the form $(-1)^r A'/r^{\alpha_S} + B'/r^{\alpha_U} + C$. The constant C accounts for the non-zero value of this correlator present at temperatures close to the phase transition, we attribute this effect to finite sizes in simulations. In Fig. 5.11a we show the variation of the exponents α_S and α_U over the temperature range. One can see that, as expected the staggered exponent α_S is close to 2 which corresponds to the dipolar contribution while the exponent $\alpha_U > \alpha_S$ throughout the temperature range considered confirming that the staggered effect we see is due to the subleading terms in the correlators, which did not cancel exactly. In Fig. 5.11b we also show the amplitudes A' and B' . As one can observe the amplitude of the dipolar component A' decreases which explains why we observe the prominent staggering effect of the subleading term as we approach the transition temperature.

Next, we consider the crossed correlators $C^C = \langle n_{\mathbf{-}}(0)n_{\mathbf{+}}(\mathbf{r}) \rangle + \langle n_{\mathbf{+}}(0)n_{\mathbf{-}}(\mathbf{r}) \rangle - 1/2$ along the direction $\mathbf{r} = (r, 0)$ which is expected to be dominated only by the vertex contribution according to Eq. 5.7. We show this for different temperatures in Fig. 5.12a. The crossed correlators show the expected power law scaling at large distances but with pos-

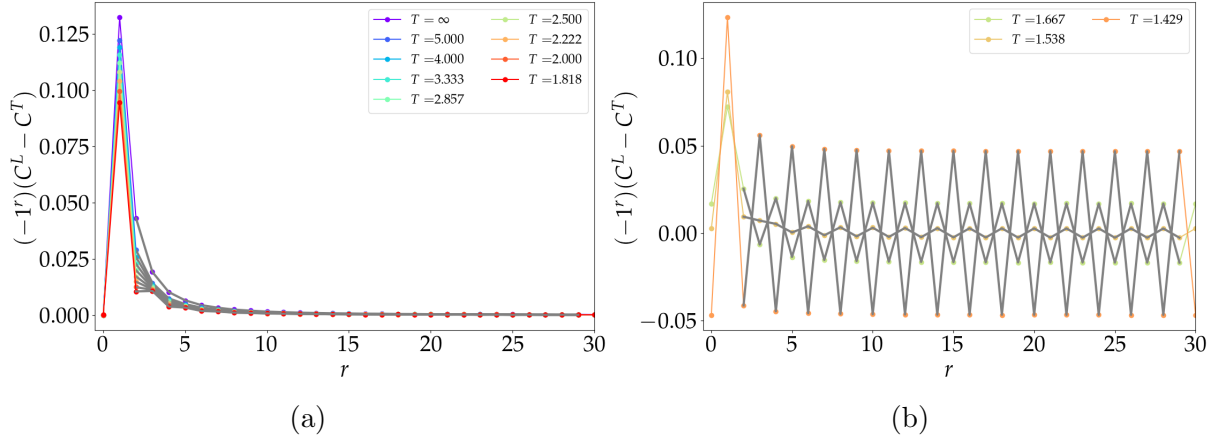


Figure 5.10: (a) $(-1)^r(C^L - C^T)$ as a function of linear distance r . (b) shows the same for temperatures near the transition to emphasise the prominent staggering effect. For the power-law fits shown in grey lines, we use the scaling form $(-1)^r A'/r^{\alpha_S} + B'/r^{\alpha_U} + C$. The constant C here is added to account for the finite value of the correlators at large distances due to finite sizes in our Monte Carlo simulations.

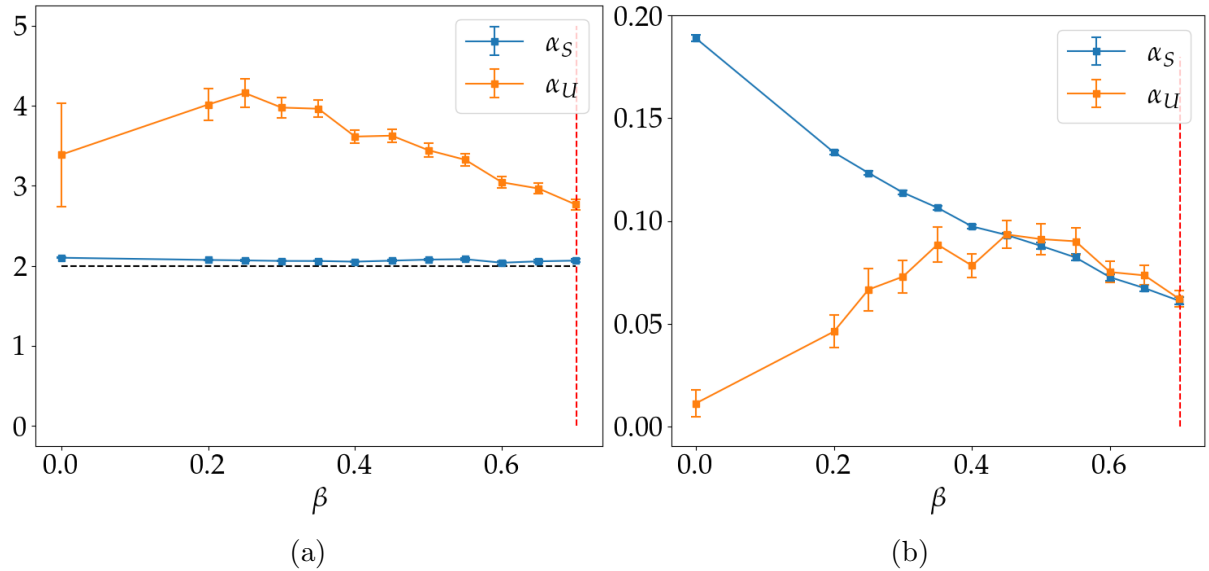


Figure 5.11: The variation of different parameters with inverse temperature β obtained from the fits of the correlator $(-1)^r(C^L - C^T)$. (a) shows the variation of exponents α_S and α_U . Since $\alpha_U > \alpha_S$ over the temperature range considered, we can safely conclude that it is a subleading correction to the correlator. (b) shows the absolute value of the amplitudes A' and B' of the leading and the subleading contributions for the correlator obtained by fitting. This explains why we observe the prominent staggering effect only near the transition temperature since the amplitude of the subleading correction becomes comparable to the amplitude of the leading term.

sible oscillatory sub-leading corrections that affect the short-distance correlations, which is visible at high temperature. Similar to the previous case of $C^L - C^T$, we attribute this to further subleading terms in Eq. 5.7 which do not cancel in the direction $y = 0$. We therefore fit the correlations to the form $(-1)^r A'/r^{\alpha_S} + B'/r^{\alpha_U} + C$ to obtain the

Coulomb gas constant g . Furthermore, we also consider the correlator associated to the order parameter $\langle D(0)D(r) \rangle$ in Fig. 5.12b which we fit to a single power-law as its leading contribution should decay as $1/r^{1/g}$.

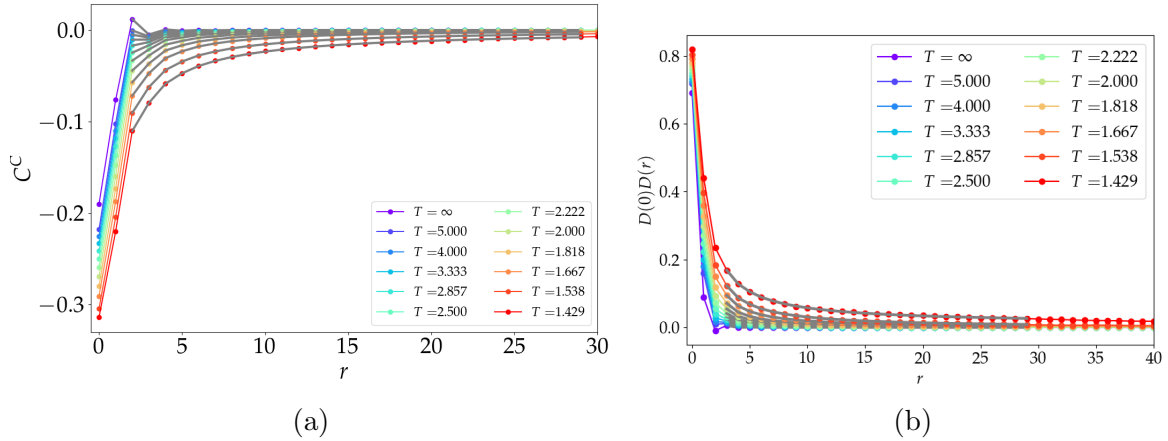


Figure 5.12: (a) Crossed correlators C^C as a function of linear distance r . We observe a subleading staggering contribution for small distances and large temperatures. The grey curves are power-law fits to the form $(-1)^r A'/r^{\alpha_S} + B'/r^{\alpha_U} + C$. (b) Correlator associated to the nematic order parameter defined in Eq. 5.11, as a function of distance. The grey curves are power-law fits to the scaling form $B'/r^{1/g}$. The above correlators are obtained for system size $L = 256$.

Finally, the monomer-monomer correlator $M(r)$ should decay only with the vertex contribution. In Fig. 5.13, we show $M(r)$ at different temperatures for system size $L = 400$ (within directed loop algorithm, we can get good statistics for $M(r)$ for larger system sizes than for loop-segment correlators). The log-log plot shows a clear power-law decay above the Kosterlitz-Thouless transition temperature.

We now collect, in Fig. 5.14 the value of Coulomb gas constant g obtained from the fits to the correlators $C^L + C^T$ (shown in Fig. 5.9), C^C (Fig. 5.12a), $\langle D(0)D(r) \rangle$ and $M(r)$ (Fig. 5.13) as well as from winding number fluctuations $\langle W^2 \rangle$. In Fig. 5.14, we show g as a function of inverse temperature $\beta = 1/T$. We find that as β increases (i.e temperature decreases), the Coulomb gas constant increases from its infinite temperature value $1/3$ to 1 near $T_{KT} \simeq 1.425$ ($\beta_{KT} \simeq 0.7$). The various estimates of g are in overall good agreement with each other and consistent with our predictions from field theory, except for C^C and $\langle D(0)D(r) \rangle$ which are less accurate due to presence of subleading oscillations at higher temperature.

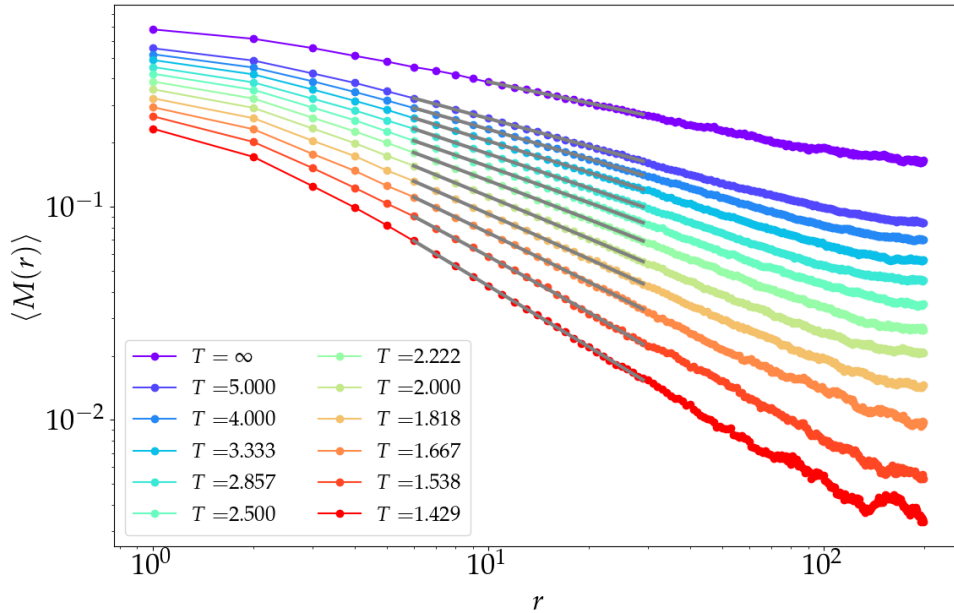


Figure 5.13: Log-log plot of the monomer correlations $M(r)$ for system size $L = 400$. The grey line shows a fit to a single power-law of the form $B/r^{1/g} + C$.

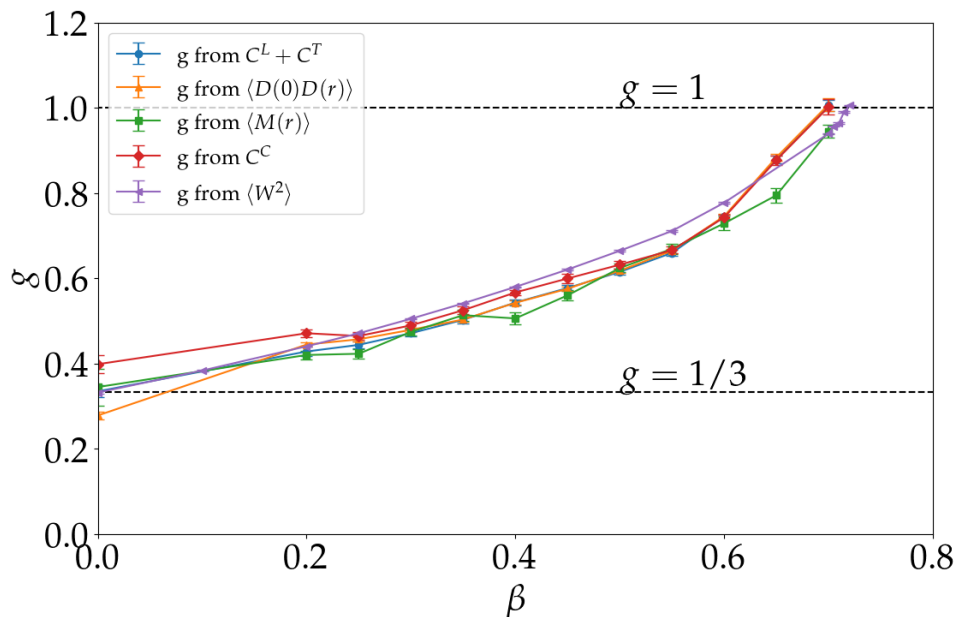


Figure 5.14: The estimates of the Coulomb gas constant g obtained by fitting the various correlators and from $\langle W^2 \rangle$. The two dashed lines denote the critical values of g at infinite temperature ($g_c = 1/3$) and at the Kosterlitz-Thouless transition ($g_c = 1$).

5.4 Discussion and outlook

A natural extension of the above study is to consider the case of *repulsive* interactions, with $V > 0$ in Eq. 5.1. Similar to the dimer case in the previous chapter, we expect the low temperature ordered states to be *staggered* configurations of loops such that there

are no flippable plaquettes, see Fig. 5.15.

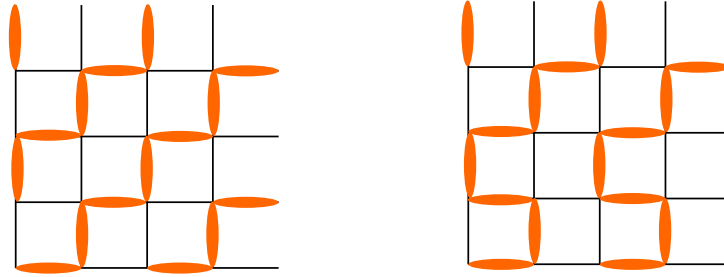


Figure 5.15: Two examples of staggered configurations of closed packed loops on a 4x4 square lattice.

One can define an order parameter to capture this ground state based on the observation that the winding numbers (W_x, W_y) for all the staggered states lie on a square as shown in fig. 5.16.

$$O_{staggered} = \frac{1}{L} (|W_x + W_y| + |W_x - W_y|) \quad (5.16)$$

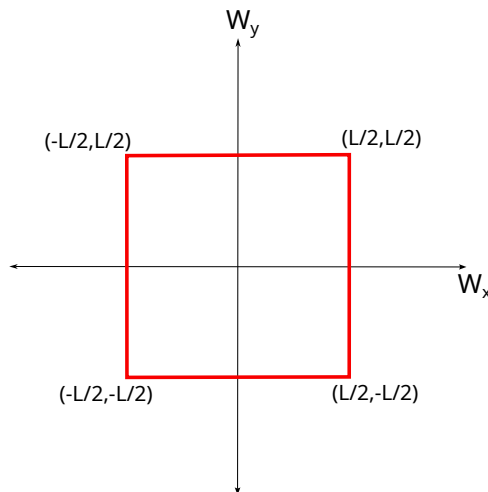


Figure 5.16: Winding numbers of all the loop configurations in the staggered phase lie on a square (red) following the equation $|W_x + W_y| + |W_x - W_y| = L$.

We recall here that for the case of the classical interacting dimer model this phase transition was shown to be continuous [31] and we arrived at the same conclusion for the quantum dimer model in the previous chapter. We show some preliminary data for the order parameter $O_{staggered}$ in Fig. 5.17. As expected the order parameter is 1 in the staggered phase while it is 0 on the disordered side. The transition looks continuous (similar to the case of dimers). However, inside the staggered phase, simulations are particularly hard owing to its sub-extensive degeneracy. We have checked that one needs to run the simulations over a large number of initial seeds to get reliable results. This requires further detailed investigation.

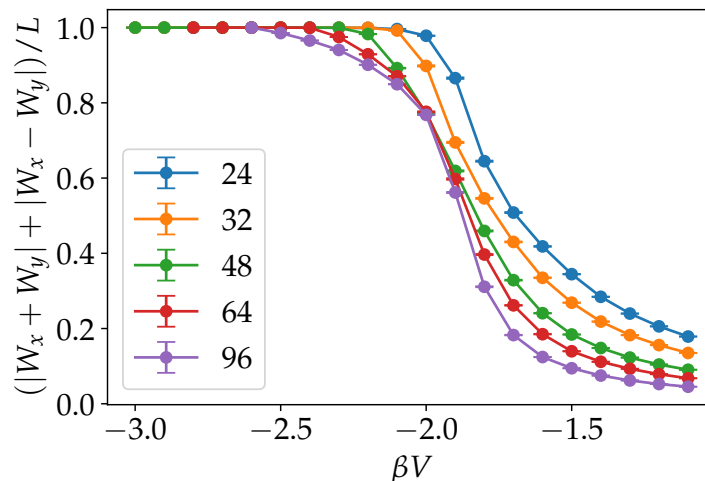


Figure 5.17: The variation of the order parameter on the staggered side, $O_{\text{staggered}}$ defined in Eq. 5.16, as a function of temperature for various system sizes.

Finally, an interesting variation of the loop model was recently proposed [111], where the authors consider a dimer-loop model. Instead of having only closely packed loops on a lattice, they consider configurations in which every vertex of the lattice can have one of the following 10 configurations, see Fig. 5.18.

Hence in addition to closely packed loops we also have hard core dimers with a fugac-

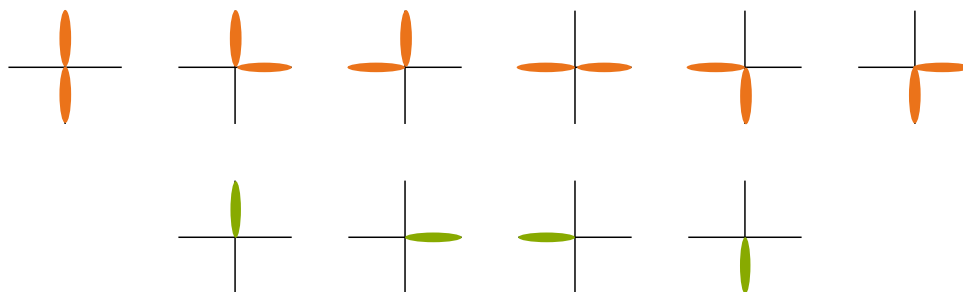


Figure 5.18: The 10 possible configurations at every site of the square lattice in the loop-dimer model.

ity w . Note that for $w = 0$, this is the fully packed loop model while for $w = \infty$ this becomes the classical non-interacting dimer model. Using Monte Carlo simulations and field theoretic arguments, the authors of Ref. [111] show an unusual *flux fractionalization* transition as the fugacity for dimers is varied. They show that the electric flux (winding numbers) are integer valued for $w > w_c$ while they are half integers for $w < w_c$. One can now extend the phase diagram further by adding interactions in this model. Consider the simplest case in which we have attractive interactions between loop segments (and no interactions between two dimer segments and dimer and a loop segment). From some preliminary calculations and basic considerations, we expect a rich phase diagram

to emerge, as shown in Fig. 5.19. Notice that for $w = 0$, the phase transition is nothing but the Kosterlitz Thouless transition to nematic loops studied in this chapter. This KT type phase transition extends as dimer fugacity w is increased and eventually becomes first order for higher fugacities. In a similar way, the flux-fractionalization transition line also extends with temperature. It is interesting to investigate if these lines meet in a way similar to a tricritical point.

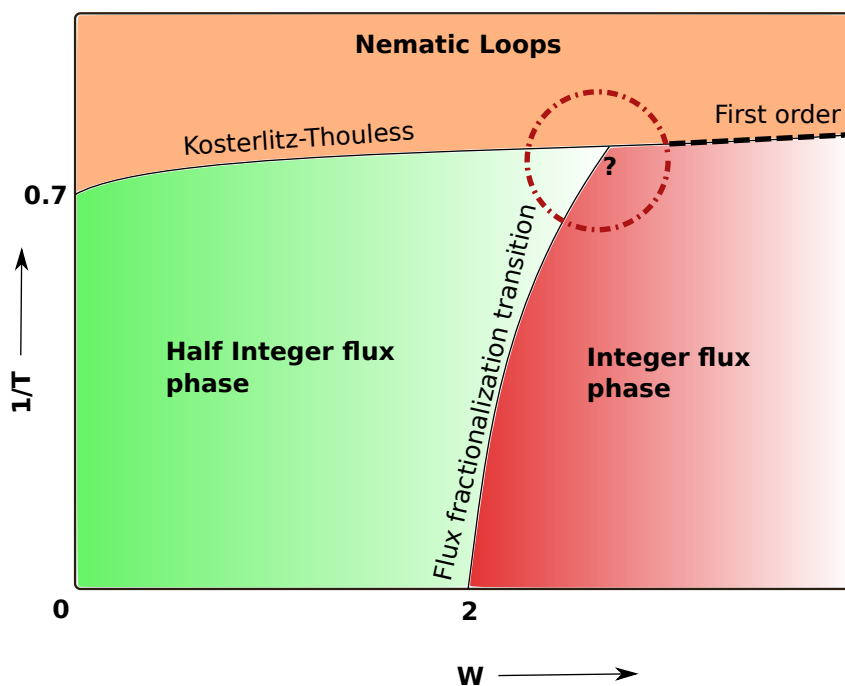


Figure 5.19: The proposed phase diagram of the loop-dimer model with interactions between parallel loop segments. The circular region needs further investigation to check if the phase transition lines meet at one point.

Chapter 6

Exact diagonalization of a disordered $SU(3)$ spin chain

In this chapter we study the thermalization properties of a disordered $SU(3)$ symmetric Heisenberg spin chain using exact diagonalization. The results we obtain add to the understanding of the role of non-Abelian symmetries in thermalization, and in particular how they prevent strict localization at strong disorder.

Localization induced by the presence of strong disorder is one way for interacting quantum many-body systems to escape the prevailing thermalization paradigm epitomized by the eigenstate thermalization hypothesis [112, 113, 114]. The resulting phenomenon of many-body localization [115, 116] has been the subject of many theoretical and experimental investigations and is the arena for a plethora of non-ergodic phenomena: absence of transport even at “infinite temperature” [115, 117], entanglement area law for highly-excited eigenstates [118, 119, 120], memory of the initial state [121], logarithmic growth of entanglement after a quench [119, 122, 123], to mention a few highlights. 1D quantum spin chains are the most popular playground to explore thermalization and MBL physics [124, 125, 119, 126, 127, 128]. We begin the chapter in section (6.1) by understanding what thermalization entails for an isolated quantum many-body system, to this extent we will define the eigenstate thermalization hypothesis (ETH). With a few words on the connection between ETH and random matrix theory, we proceed to review the commonly used indicators of ETH which include the statistics of eigenstates, behaviour of a local observable and the entanglement entropy (EE). We then briefly review in section (6.2) how a many-body system in presence of disorder could escape thermalization, a phenomenon now commonly referred as many body localization. After this general introduction, we specialize to the specific case of non-Abelian disordered spin chains.

Since our results build upon a previous work on disordered $SU(2)$ symmetric Heisenberg

spin chain, we briefly recall its main results in section(6.3). In section(6.4), we describe the general construction of a $SU(N)$ symmetric Heisenberg model in an orthogonal unit representation of Young tableau. Our ED results for the above mentioned indicators of ETH and its possible breakdown for the $SU(3)$ case are presented in section(6.5), and section(6.6) concludes the chapter with a summary of the comparison of our results with the $SU(2)$ case.

6.1 Thermalization in quantum systems

The *ergodic hypothesis* forms the foundations of classical statistical mechanics. It states that for an isolated system at energy E , given infinite time, the system would explore with equal probability, all of its configurations (phase space) compatible with energy E . We call the ensemble of these configurations the *microcanonical ensemble*. This tells us that for any observable $O(t)$, its infinite time average is the microcanonical ensemble average.

$$\lim_{T \rightarrow \infty} \frac{1}{T} \int_0^T O(t) dt = \langle O \rangle_{mc} \quad (6.1)$$

6.1.1 Eigenstate thermalization hypothesis

Consider an *isolated* quantum many body system with a Hamiltonian H . We prepare the system in a *generic* state (a physically realisable state) at $t = 0$, $|\psi(t = 0)\rangle$. We expand $|\psi(t = 0)\rangle$ on the energy eigenbasis $\{|\alpha\rangle\}$ as $|\psi(t = 0)\rangle = \sum_{\alpha} C_{\alpha} |\alpha\rangle$. Then at any time t , $|\psi(t)\rangle = \sum_{\alpha} C_{\alpha} e^{-iE_{\alpha}t} |\alpha\rangle$ where E_{α} s are the discrete energies of the corresponding eigenstates $|\alpha\rangle$. Now, the expectation value of an observable \hat{O} at time t is given by

$$\langle O \rangle_t = \sum_{\alpha} |C_{\alpha}|^2 \langle \alpha | O | \alpha \rangle + \sum_{\alpha \neq \beta} C_{\alpha} C_{\beta}^* e^{-it(E_{\alpha} - E_{\beta})} \langle \beta | O | \alpha \rangle. \quad (6.2)$$

Let us go back a few steps when we prepared our generic state at $t = 0$. Let us assume we prepare the state such that the initial probabilities $|C_{\alpha}|^2$ are peaked around the energy $E = \langle \psi(0) | H | \psi(0) \rangle$ within a small window $W = \{E - \delta E, E + \delta E\}$. Since our system is isolated we can define $\langle O \rangle$ in a microcanonical ensemble as

$$\langle O \rangle_{mc} = \frac{1}{N_W} \sum_{\alpha \in W} \langle \alpha | O | \alpha \rangle \quad (6.3)$$

where N_W is the number of eigenstates in the window W and the summation is over all the eigenstates $|\alpha\rangle$ falling in the window W . Our intuition from statistical mechanics

tells us that the infinite time average of Eq. 6.2 must be given by Eq. 6.3, i.e we expect an observable at long times to reach its expectation value as given by a microcanonical ensemble. The probability amplitudes C_α set by the initial state do not evolve in time, therefore the matrix elements $\langle\alpha|O|\beta\rangle$ dictate the behaviour at long times. The eigenstate thermalization hypothesis (ETH) [112, 113], proposes the following ansatz for the matrix elements of any local observable \hat{O}

$$\langle\alpha|O|\beta\rangle = O(\bar{E})\delta_{\alpha\beta} + e^{-S(\bar{E})/2}f_O(\bar{E},\omega)R_{\alpha\beta} \quad (6.4)$$

where $\bar{E} \equiv (E_\alpha + E_\beta)/2$, $\omega \equiv E_\alpha - E_\beta$, $R_{\alpha\beta}$ is a random real variable with zero mean and unit variance, $S(E)$ is the thermodynamic entropy of the system and $O(E)$ and $f_O(E, \omega)$ are smooth continuous functions of energy E .

One would expect the second term in Eq. 6.2 to average out in long times due to dephasing but there is a subtlety here. For a many-body spectrum, the energy gaps ($E_\alpha - E_\beta$) are exponentially small in system size which would imply the dephasing could take place in exponential long times contrary to what is observed in experiments where even large systems thermalize over fairly short time scales. The ETH ansatz reconciles this by giving the off-diagonal matrix elements $\langle\alpha|O|\beta\rangle$ ($\alpha \neq \beta$) weights which are exponentially small in system size (the thermal entropy $S(\bar{E})$ is extensive except for the ground state). The long time average of Eq. 6.2 is therefore given by the diagonal matrix elements

$$\lim_{T \rightarrow \infty} \frac{1}{T} \int_0^T \langle O \rangle_t dt = \sum_\alpha |C_\alpha|^2 \langle\alpha|O|\alpha\rangle \quad (6.5)$$

Eq. 6.4 states that $\langle\alpha|O|\alpha\rangle$ vary as a continuous function of eigenstate energy E_α ($\langle\alpha|O|\alpha\rangle = f(E_\alpha)$) and hence within the narrow energy window W , at least to the first order, they are almost constant. Notice that even though the eigenenergies E_α are discrete for a finite system, for a many body system they are so closely (exponentially) spaced that one could regard them as continuous. From the above arguments, we could regard the matrix elements in Eq. 6.5 and Eq. 6.3 are constant ($\langle\alpha|O|\alpha\rangle \approx C$), giving

$$\lim_{T \rightarrow \infty} \frac{1}{T} \int_0^T \langle O \rangle_t dt = \langle O \rangle_{mc}, \quad (6.6)$$

reconciling our expectations from statistical physics that a generic quantum many body system should thermalize [112, 113, 129].

We end our discussion on ETH with an important takeaway : the information of the *thermal equilibrium state* is in fact hidden in individual eigenstates of the Hamiltonian. This shows the *self-thermalizing* property of an isolated interacting quantum many body system where it can act as a heat bath for its own subsystems. Even though it allows to "justify" the ergodic behaviour observed in the vast majority of many body quantum

systems, it must be emphasized that ETH is only an hypothesis.

6.1.2 Connection to Random matrix theory

Let us now see how the matrix elements of \hat{O} would be if the Hamiltonian was a random Hermitian matrix. Random matrix theory tells us that the eigenvectors of such a matrix are random orthonormal vectors. The matrix element of \hat{O} in such a random eigenstate $|\alpha\rangle$ is

$$\langle\beta|\hat{O}|\alpha\rangle = \sum_i O_i \langle\beta|i\rangle \langle i|\alpha\rangle = \sum_i O_i (\psi_i^\beta)^* \psi_i^\alpha \quad (6.7)$$

where $\psi_i^\alpha = \langle i|\alpha\rangle$. Since ψ_i s are entries of a random orthonormal vectors in D dimensional space, where D is the dimension of the Hilbert space, we have

$$\overline{\psi_i^\alpha \psi_i^\beta} = \frac{1}{D} \delta_{ij} \delta_{\alpha\beta} \quad (6.8)$$

where the average is taken over an ensemble of random vectors. Using Eq. 6.8 in Eq. 6.7 we get

$$\overline{\langle\beta|O|\alpha\rangle} = \begin{cases} \frac{1}{D} \sum_i O_i = \bar{O}, \alpha = \beta \\ 0, \alpha \neq \beta \end{cases} \quad (6.9)$$

The fluctuations of the matrix elements can also be shown to satisfy [130]

$$\overline{\langle\beta|O^2|\alpha\rangle} - \overline{\langle\beta|O|\alpha\rangle}^2 = \begin{cases} \frac{3-\eta}{D^2} \sum_i O_i^2 = \frac{3-\eta}{D} \overline{O^2}, \alpha = \beta \\ \frac{1}{D^2} \sum_i O_i^2 = \frac{1}{D} \overline{O^2}, \alpha \neq \beta \end{cases} \quad (6.10)$$

where, $\eta = 1$ for a gaussian orthogonal ensemble (GOE) i.e all ψ_i s are real and $\eta = 2$ for a gaussian unitary ensemble (GUE) i.e ψ_i s are complex. Combining the above, one can write the individual matrix elements to the leading order in $1/D$ as,

$$\langle\alpha|O|\beta\rangle \approx \bar{O} \delta_{\alpha\beta} + \sqrt{\frac{\overline{O^2}}{D}} R_{\alpha\beta} \quad (6.11)$$

where $R_{\alpha\beta}$ is a real random variable with zero mean and unit variance (the variance is 2 for diagonal matrix elements for a GOE). One could clearly see the similarities between Eq. 6.11 and the ETH ansatz of Eq. 6.4, however the ETH ansatz is a much stronger statement on the variation of the matrix elements applicable to real physical systems at finite energy densities. In conclusion, this tells us that the thermal eigenstates behave like eigenvectors of a random matrix, which is quite remarkable since a many-body Hamil-

tonian is in general sparse and has deterministic elements, unlike a typical random matrix.

6.1.3 Probes of ETH

In this section we review, in the context of many-body systems, some commonly used indicators/tests for ETH which we will make use for our study in the latter sections. ETH has been verified numerically in several models [114].

Distribution of a local observable: This could be regarded as a direct test of ETH. We consider a local observable \hat{O} in our model, for example $\hat{O} \equiv \mathbf{S}_i \cdot \mathbf{S}_{i+1}$ for a disordered spin-1/2 Heisenberg chain [127]. By directly looking at the distribution of \hat{O} in an ensemble of excited eigenstates, we expect the distribution to be sharply (Gaussian) peaked around its value in the microcanonical ensemble if the eigenstates are thermal and obey ETH.

Level statistics: The RMT connection shown in the previous section makes way for using properties of random matrices to test ETH. One of the signature properties is the distribution of the eigenvalue gaps ($\Delta = E_n - E_{n-1}$) given famously by the Wigner surmise [131]. It was proposed in [117] that a better quantity to look at is the distribution of the ratio of two consecutive gaps, to reduce finite size effects. This quantity, now referred to as the *Gap ratio*, is defined as

$$r_n \equiv \frac{\min(\Delta_n, \Delta_{n+1})}{\max(\Delta_n, \Delta_{n+1})} \quad (6.12)$$

For a GOE ensemble, the gap ratio follows the distribution $P^{GOE}(r) = \frac{27(r+r^2)}{4(1+r+r^2)^{5/2}}$ with mean value $\langle r \rangle_{GOE} \simeq 0.5307$ [132]. As we will see later, the gap ratios are easily accessible to exact diagonalization based studies.

Scaling of entanglement: Another key observable in signaling ETH is the entanglement entropy. Let us quickly recall its definition. Consider the system to be in a pure state $|\psi\rangle$, and partition the system in real space in two parts A and B . Since we are concerned in this chapter with spin chains, we divide the chain of length L in a two subsystems of lengths L_A and L_B such that $L_A + L_B = L$. If we denote $\hat{\rho}_A = Tr_B(|\psi\rangle\langle\psi|)$ the reduced density matrix of subsystem A , the Von Neumann EE for subsystem A is given by $S_A = -\text{Tr}(\hat{\rho}_A \ln(\hat{\rho}_A))$.

If we take $|\psi\rangle$ to be one of the excited eigenstates which are thermal, one could argue that, assuming subsystem B is larger than A (essentially acting as a heat bath for A) the EE

for A (S_A) is very close to the thermodynamic entropy for A. Since the thermodynamic entropy is an extensive quantity, S_A must scale as the *volume* of subsystem A. Therefore thermal eigenstates obey the *volume law EE*. In a 1D system for example, $S_A \sim L_A$ for a thermal phase. As we saw in the previous section, thermal eigenstates are eigenvectors of a random matrix. One can therefore compute S_A taking $|\psi\rangle$ to be random vectors. For a random pure eigenstate the leading term of the average EE of a 2^{L_A} -dimensional subsystem is $L_A \ln(2)$ (and there is a small order $O(1)$ correction). This is called the Page law [133] (and the Page correction).

6.2 Breakdown of ETH

Are there systems which escape ETH? This is a topic of intense activity in the last few years. One can violate the ETH weakly where only a few eigenstates do not satisfy it. One of the signatures of this are quantum many-body scars, shown famously for the PXP model [134]. We are concerned here with a strong violation of ETH. This includes the class of models which are integrable, which possess an extensive number of integrals of motion (see section 8 in [130]). Another class of widely studied models which violate ETH are the ones which host localized eigenstates in the presence of disorder.

A well studied example of localization in presence of disorder is Anderson localization [135, 136]. This is a very simple case of single-particle localization nicely illustrated by considering a tight-binding Hamiltonian on a lattice,

$$H_{\text{Anderson}} = \sum_i \mu_i c_i^\dagger c_i + t \sum_{\langle ij \rangle} (c_i^\dagger c_j + c_j^\dagger c_i) \quad (6.13)$$

where the on-site potential μ_i is taken as random from a box distribution $[-W/2, W/2]$ due to the presence of disorder and t is the usual hopping strength between neighbouring sites. In one and two dimensions the above Hamiltonian has eigenstates which are all exponentially localized. Eigenstates nearby in energies have localization centers far apart in real space and hence they violate ETH. In three dimensions and higher, the model shows a metal-insulator transition [137]. One could easily extend Eq. 6.13 in a many particle but still non-interacting setting, where the full many body eigenstate is just a Slater determinant of the single particle eigenstates. If we initialize our particles as localized at different positions in real space, they would stay localized and hence evade thermalization. Note that in this setting all the eigenstates violate ETH.

6.2.1 Many body localization

The natural question to ask now is, what happens to such a localized/insulating phase in the presence of interactions. For example, Eq. 6.13 on a 1D chain with nearest neighbour interactions given by,

$$H_{\text{interaction}} = \sum_i \mu_i n_i + t \sum_i (c_i^\dagger c_{i+1} + c_{i+1}^\dagger c_i) + V \sum_i n_i n_{i+1} \quad (6.14)$$

where $n_i = c_i^\dagger c_i$. It was suggested early on that this localized phase could be stable to finite short range interactions even up to some finite critical temperature beyond which the system thermalizes [115, 116]. Such a localized phase, in presence of interactions, which exists even at high temperature (finite energy densities) is now commonly called the *Many Body Localized* (MBL) phase [138, 139].

On the numerical front, the work by Oganesyn and Huse [117] set precedence for exact diagonalization based studies of MBL. They study Eq. 6.14 for spinless fermions with added next nearest neighbour interactions. Although limited to small sizes, they conclude that for systems with finite local Hilbert space the MBL phase could survive up to infinite temperature. Many seminal works following this also focus on disordered spin chains [122, 124, 127, 125]. In section 6.2.4, we briefly comment on the current status of the MBL phase and its stability.

It is important to emphasize that MBL states occur at finite energy densities and are fundamentally different from localized ground state phases like Bose glass which also survive interactions. The connection between these is still an open question.

6.2.2 Probes of MBL

Let us now see how the probes of thermalization, which we saw earlier, now behave for MBL eigenstates.

Level statistics: Consider an ensemble of excited eigenstates with energies E_i generated for example for a given disorder realization, $\{E_1, E_2, \dots, E_n\}$. For Hamiltonian in Eq. 6.14, assuming disorder is very strong, the eigenstates will be close to a product state $|n_0, n_1, n_2, \dots, n_n\rangle$ and each E_i in the many body spectrum occurs independently of one another. Reformulating the above, we find that the probability that E_i occurs at spacing Δ after E_{i-1} is nothing but a *Poisson process*. The spacing Δ follows a Poisson distribution, $P(\Delta) = \rho e^{-\rho\Delta}$, here ρ is say the average number of energy levels in unit interval of energy. By considering the distribution of the ratio of two Poisson distributed

variables we can show that the probability distribution of the gap ratio r , as defined in Eq. 6.12 is $P(r) = 2/(1+r)^2$ which gives a mean gap ratio $\langle r \rangle_{\text{Poisson}} \sim 0.38$.

Entanglement entropy: MBL eigenstates have a lower entanglement than their thermal counterparts due to their localized nature. One therefore expects the EE to show an *area-law* scaling, something which is typical for ground states of gapped Hamiltonians [140]. Such a scaling was numerically confirmed in various studies [141, 118, 142]. For MBL eigenstates of 1D systems, we therefore expect $S_A(L_A) \sim c$ where c is a constant. This was shown for example in a Heisenberg spin chain with a random magnetic field [124].

In proceeding section we will also encounter systems which show *logarithmic EE* scaling, $S_A \sim \log(L_A)$. This classifies as a phase which is not fully MBL but not ergodic either since the EE is still sub-volumic.

Dynamical signatures of MBL: As expected for an insulating phase, MBL systems have vanishing DC conductivity. What sets apart an MBL phase from an Anderson insulator is the spreading of entanglement in a quench setup. Starting from an initial product state $|\psi(t=0)\rangle$, if one tracks the growth of EE of a subsystem with time, one finds that even in the absence of transport an MBL phase shows slow logarithmic spreading of EE, $S_A(t) \sim \ln(t)$ [143, 123, 122, 119]. For a typical Anderson insulator there is no spreading of EE, $S_A(t)$ is bounded. In an ETH phase, this spreading of EE is ballistic $S_A(t) \sim t$ [144].

In both the ETH and MBL phases the EE eventually saturates to some value in the long time limit. This value is different in the two phases and could serve as an indicator. For a 1D system, in the ETH phase the EE saturates to $S_A(t \rightarrow \infty) \sim s(E)L_A$, where $s(E)$ is the thermal entropy density at energy E . In an MBL phase, the EE saturates to $S_A(t \rightarrow \infty) \sim cL_A$, where the prefactor $c < s(E)$. This growth of EE and the saturation value is understood in 1D through the emergent integrability in the MBL phase, interested readers are referred to [138, 139].

Another important dynamical property of a MBL phase is the memory retention of the initial state post quench. This was first demonstrated in a cold-atom experiment on a 1D system of ultra-cold fermions in a quasi-periodic potential [145]. The experiment studies post quench dynamics with an initial state which is a charge density wave, where the atoms are located only on the even sites. They track the variation of a quantity called *imbalance* given simply by $\frac{|N_e - N_o|}{N_e + N_o}$, where N_e and N_o denote the number of atoms on even and odd sites respectively. They observe that the imbalance rapidly decays to zero which is its equilibrium value in the absence of a random potential. While for finite (strong

enough) disorder the imbalance saturates to a finite non-zero value in the experimentally accessible time frames.

6.2.3 Structure of MBL eigenstates : Local integrals of motion

The most extensively studied model for MBL in 1D is the spin-1/2 XXZ chain with on-site disorder (which is related to Eq. 6.14 through a Jordan-Wigner transformation), given by

$$H_{XXZ} = J \sum_i (S_i^x S_{i+1}^x + S_i^y S_{i+1}^y) + \Delta \sum_i S_i^z S_{i+1}^z + \sum_i h_i S_i^z. \quad (6.15)$$

Here $S_i^\alpha = \sigma_i^\alpha/2$ ($\alpha = x, y, z$) are the usual Pauli spin matrices and h_i is the random on-site disorder (taken again from a box distribution $[-W/2, W/2]$). In the limit $J = 0$, the eigenstates of Eq. 6.15 are trivially localized product states $|\alpha_0\rangle = |\dots\sigma_i^z\sigma_{i+1}^z\dots\rangle$, with $\sigma_i^z = \uparrow, \downarrow$. The Hamiltonian commutes with each σ_i^z and therefore they form a set of local integrals of motion (LIOM) with eigenvalues ± 1 .

It turns out one could construct a similar product state basis for MBL eigenstates, $|\alpha\rangle = |\dots\tau_i^z\tau_{i+1}^z\dots\rangle$, where the τ_i^z s called l-bits or LIOMs and they are related to σ_i^z s as

$$\tau_i^z = \sigma_i^z + \sum_{j,k} \sum_{a,b} c_{ijk}^{ab} \sigma_j^a \sigma_k^b + \dots \quad (6.16)$$

where the coefficients c exponentially decay with distance between site i and sites j, k , which is why the LIOMs are called *quasi-local* integrals of motion. The unitary transformation which relates τ_i^α s and σ_i^α s (Eq. 6.16 shows an example for τ_i^z) diagonalizes H_{XXZ} and is (quasi-) local, which is quite remarkable as such a scenario rarely occurs for a generic interacting many-body system. This hints at the emerging local integrability of the MBL phase.

All the properties we saw before for the MBL phase - Poisson statistics, area-law entanglement and the memory retention of the initial state in a quench setup now start to make sense in the LIOMs picture since the MBL eigenstates in this setting are product states of these quasi-local Pauli operators $|\alpha\rangle = |\dots\tau_i^z\tau_{i+1}^z\dots\rangle$ with $\tau_i^z = \pm 1$. For a complete review of the LIOM picture of MBL, see [146, 147].

6.2.4 Current status of MBL

For MBL to qualify as a genuine non-ergodic phase of matter it must be stable in the thermodynamic limit. The numerics so far are limited to very small system sizes since most of them are based on exact diagonalization and the numerics which study quench

dynamics are limited to short times. Quench experiments with ultra-cold atoms are also limited to short time scales. An interesting way forward which has recently been gaining attraction is to understand mechanisms which could destabilize MBL and study their effects in simpler phenomenological models.

One such mechanism is the so called *quantum avalanche* [148]. The avalanche theory proposes that in an infinite disordered landscape, one would always stumble upon rare regions where the disorder is weak and the system locally thermalizes, this region acts as a heat-bath, thermalizing the degrees of freedom in its immediate vicinity. Even though the bath starts out weak, it grows by thermalizing farther degrees of freedom creating an avalanche which thermalizes the whole system.

The original work proposing the theory shows that for higher dimensions ($d > 1$) MBL is always unstable to avalanches leading to thermalization but in 1D the avalanche could stop and a stable MBL phase could exist. The present consensus is that the widely studied MBL transition on the 1D Heisenberg spin chain in a random field [124, 125, 149] is in fact not a phase transition but a crossover from a *prethermal MBL regime* to a thermal phase [150, 151, 152, 153, 154, 155, 156]. This prethermal MBL regime shows properties of localization on small system sizes and time scales but will eventually thermalize in the thermodynamic limit. The full MBL phase seems to occur at much larger disorder strengths than that observed in previous numerical studies. For a recent review of the field, see [157].

6.3 Brief review of disordered SU(2) spin chain.

Existence of a stable MBL phase with a certain global symmetry is an interesting question [158]. We already have extensive numerical evidence of MBL phases or at least regimes (see subsection 6.2.4) with abelian symmetry (such as the U(1) symmetry in models of Eq. 6.15 and Eq. 6.14), at least in 1D. If we consider a MBL phase as characterized by local integrals of motion (LIOM), it was argued that certain symmetry protected topological orders and non-abelian symmetries are incompatible with MBL [159]. The key argument put forward is that, due to existence of exact degeneracies in the many-body spectrum localized eigenstates at finite energies would be unstable to interactions: loosely speaking, degeneracies offer too many thermalization channels for creation of resonances. As a result, the system must either thermalize (as we will see later for continuous non-abelian symmetries like SU(N)) or spontaneously break the non-Abelian symmetry to an Abelian subgroup, this was demonstrated for spin chains with non-Abelian symmetries with finite dimensional irreducible representations [160, 159].

One can therefore rule out a full MBL phase with non-Abelian symmetries. However, the

possibility of a partially localized phase remains. This could be a phase characterized by logarithmic entanglement scaling, which is not fully an area-law (for an MBL phase) but still *subthermal*. Example of phases with such scaling are quantum critical glasses [161, 162].

In this section we briefly recall the important results from a recent work on $SU(2)$ symmetric Heisenberg spin chain in presence of bond disorder [127]. The authors focus on a very simple Hamiltonian

$$H = \sum_{i=1}^L J_i \mathbf{S}_i \mathbf{S}_{i+1} \quad (6.17)$$

where the couplings J_i are drawn at random from a probability distribution given by $P(|J|) = \frac{\alpha \Theta(1-|J|)}{|J|^{1-\alpha}}$ where $\Theta(x)$ is the Heaviside function and \mathbf{S}_i are the usual spin-1/2 operators. Here half of the links are ferromagnetic and half anti-ferromagnetic. The existence of a non-ergodic regime was discussed in detail for the Hamiltonian in Eq. 6.17 in Ref. [127]. The main objective of this study is to investigate if this Hamiltonian could host a non-thermal/ergodic phase and if so, is such a phase stable in the thermodynamic limit.

6.3.1 Existence of a broad non-ergodic regime

The authors show that eigenstates of Eq. 6.17 have a tree like hierarchical structure due to which they show a logarithmic scaling of entanglement entropy ($S_A \sim \ln(L_A)$). Such tree states are only approximations to the eigenstates of Eq. 6.17 as they are built using a real space RG procedure called *Strong disorder renormalization group* (SDRG) [163, 164]. Hence it is imperative to check if such tree eigenstates are good approximations to the true eigenstates of Eq. 6.17 at finite disorder values. The authors of [127] perform this analysis at different length scales of the chain.

Exact Diagonalization on smaller system sizes: The authors perform ED up to system sizes of $L = 26$. By looking at the standard MBL probes mentioned above like the level statistics, test of ETH and entanglement entropy, they extract a length scale $L^*(\alpha)$ ($1/\alpha$ quantifies the disorder strength). For system sizes below this length scale, the tree eigenstates are in fact good approximations to Eq. 6.17 while for system sizes greater than $L^*(\alpha)$ the tree eigenstates become unstable. This length scale increases with disorder strength. For weak disorder even relatively small chains will thermalize. However, for strong disorder strengths the results indicate that the tree eigenstates are stable, up to the largest system size accessible by ED.

Thermodynamic limit: The question now arises, for strong disorder strengths does the tree eigenstate picture remain stable in the thermodynamic limit. The authors investigate this by identifying in the SDRG, *resonance* processes which would cause thermalization.

They are able to again extract a length scale $L^{SDRG}(\alpha)$ beyond which the resonance processes proliferate and lead to thermalization. These length scales are quite large for strong disorder strengths, for example $L^{SDRG}(\alpha = 0.3) \approx 300$. This shows that even for strong disorder strengths the Heisenberg spin-1/2 chain would eventually thermalize in the thermodynamic limit.

To conclude, even though the Hamiltonian in Eq. 6.17 thermalizes in the the thermodynamic limit, the length scales for this are very large for strong disorder. Therefore, for all practical and experimentally realisable purposes, Eq. 6.17 shows a non-ergodic sub-thermal region for a broad range of disorder strengths and system sizes. Moreover, and quite importantly this non-ergodic region shows logarithmic entanglement scaling and has eigenstates with a tree network structure, which makes it distinct from MBL which host area-law entanglement eigenstates.

Further evidence for existence of such a non-ergodic region comes from another recent computation [165] on dynamical behaviour of SU(2) and SU(3) chains after a quench.

6.4 SU(N) Heisenberg Hamiltonian

We are interested in the study of the SU(N) generalization (we will specialize to $N = 3$ in our actual numerical computations) of the usual spin-1/2 Heisenberg Hamiltonian

$$H_{SU(N)} = \sum_{\langle i,j \rangle} J_{ij} \sum_{\alpha,\beta=1}^N S_i^{\alpha\beta} S_j^{\beta\alpha} \quad (6.18)$$

here $S_i^{\alpha\beta}$ are the SU(N) symmetric counterparts of the Pauli matrices. This Hamiltonian emerges in the Mott insulating limit of the SU(N) symmetric Hubbard model which was realised in cold atom experiments where the optically trapped fermionic particles have N flavours/colours [166, 167, 168].

In the case of one particle per site Eq. 6.18 reduces to a very simple *permutation* Hamiltonian

$$H_P = \sum_{\langle i,j \rangle} J_{ij} P_{ij} \quad (6.19)$$

where P_{ij} swaps the colours of particles on site i and j .

Our exact diagonalization study in the proceeding sections follows the construction of the SU(N) Heisenberg Hamiltonian by Nataf et al [169] in the *Young tableau* basis.

6.4.1 Young tableau

A Young tableau is an arrangement of m boxes stacked in k partitions of length λ one below the other. A Young tableau of a particular *shape* could be denoted by an array of its partition lengths from top to bottom, $[\lambda_1, \lambda_2, \dots, \lambda_k]$. We call a Young tableau a *Standard Young tableau* (SYT) when the partition lengths are in decreasing order from top to bottom such that, $\lambda_1 \geq \lambda_2 \geq \dots \geq \lambda_k$. A SYT of a particular shape forms an irreducible representation (irrep) of the $SU(N)$ symmetry group.

$$[3, 2, 1] := \begin{array}{|c|c|c|} \hline & & \\ \hline & & \\ \hline & & \\ \hline \end{array}$$

Consider n lattice sites, if an individual box of a Young tableau acts as a fundamental irrep of $SU(N)$ then, for the case of one box per site, all SYT of total n boxes of shapes $[\lambda_1, \lambda_2, \dots, \lambda_k]$ with $k \leq N$ (tableau with at most N rows) form irreps for the complete lattice.

If we label each box of the Young tableau by a number from 1 to n with the rule that all numbers below a particular number and to the right of it must be increasing, then the total number of valid numberings gives the multiplicity of that particular irrep.

$$\text{Valid SYT} := \begin{array}{|c|c|c|} \hline 1 & 2 & 3 \\ \hline 4 & 5 & \\ \hline 6 & & \\ \hline \end{array} \quad \text{Invalid SYT} := \begin{array}{|c|c|c|} \hline 1 & 2 & 3 \\ \hline 5 & 4 & \\ \hline 6 & & \\ \hline \end{array}$$

For a given tableau shape, the total number of standard Young tableau are $n! / \prod_{i=1}^N l_i$ where l_i is called the *Hook length* of each box, defined as the total number of boxes to the right of it on that particular row and below it on that particular column plus 1. Shown below is an example of assignment of Hook lengths to each box of the tableau $[3, 2, 1]$. The total number of ways to label this tableau with the above rules is $6! / (5 \cdot 3 \cdot 3 \cdot 1 \cdot 1 \cdot 1) = 16$, which is also the multiplicity of the irrep it represents.

$$\begin{array}{|c|c|c|} \hline 5 & 3 & 1 \\ \hline 3 & 1 & \\ \hline 1 & & \\ \hline \end{array}$$

6.4.2 Matrix elements in tableau basis

We need to find how the permutation operator $P_{i,i+1}$ in Eq. 6.19, which permutes colours between sites i and $i + 1$, act on a SYT (where the boxes are labelled by site indices).

Without going into the derivation (see Appendix in [169]), we can sum up this operation in the following

- $P_{i,i+1}|SYT\rangle = |SYT\rangle$ if i and $i + 1$ lie on the same **row** of the SYT. For example

$$P_{1,2} \left| \begin{array}{|c|c|c|} \hline 1 & 2 & 3 \\ \hline 4 & 5 & \\ \hline 6 & & \\ \hline \end{array} \right\rangle = \left| \begin{array}{|c|c|c|} \hline 1 & 2 & 3 \\ \hline 4 & 5 & \\ \hline 6 & & \\ \hline \end{array} \right\rangle$$

- $P_{i,i+1}|SYT\rangle = -|SYT\rangle$ if i and $i + 1$ lie on the same **column** of the SYT. For example

$$P_{1,2} \left| \begin{array}{|c|c|c|} \hline 1 & 4 & 6 \\ \hline 2 & 5 & \\ \hline 3 & & \\ \hline \end{array} \right\rangle = - \left| \begin{array}{|c|c|c|} \hline 1 & 4 & 6 \\ \hline 2 & 5 & \\ \hline 3 & & \\ \hline \end{array} \right\rangle$$

- If i and $i + 1$ do not lie on the same row or column, then $P_{i,i+1}$ connects $|SYT\rangle$ and $|\overline{SYT}\rangle$, where $|\overline{SYT}\rangle$ denotes the SYT in which we have swapped the labels i and $i + 1$. The matrix elements connecting the two are given by, $\langle SYT|P_{i,i+1}|SYT\rangle = -\rho$, $\langle SYT|P_{i,i+1}|\overline{SYT}\rangle = \langle \overline{SYT}|P_{i,i+1}|SYT\rangle = \sqrt{1 - \rho^2}$ and $\langle \overline{SYT}|P_{i,i+1}|\overline{SYT}\rangle = \rho$.

Here $\rho = 1/d$ and d is called the *axial distance* between i and $i + 1$ in $|SYT\rangle$. The axial distance d is defined by counting $+1$ (respectively -1) for each step made downwards or to the left (respectively upwards and right) to reach $i + 1$ from i . For example for

$$|SYT\rangle = \left| \begin{array}{|c|c|c|} \hline 1 & 4 & 6 \\ \hline 2 & 5 & \\ \hline 3 & & \\ \hline \end{array} \right\rangle \text{ and } |\overline{SYT}\rangle = \left| \begin{array}{|c|c|c|} \hline 1 & 3 & 6 \\ \hline 2 & 5 & \\ \hline 4 & & \\ \hline \end{array} \right\rangle$$

where we have swapped 3 and 4, the axial distance $d = -3$. Which gives $\langle SYT|P_{3,4}|SYT\rangle = 1/3$, $\langle \overline{SYT}|P_{3,4}|\overline{SYT}\rangle = -1/3$ and $\langle SYT|P_{3,4}|\overline{SYT}\rangle = \langle \overline{SYT}|P_{3,4}|SYT\rangle = \frac{2\sqrt{2}}{3}$.

One can check that starting from a SYT of a particular shape, one could generate all the SYTs of that particular shape by performing the above permutation operation, with the constraint that one does not permute i and $i + 1$ if they lie on the same row or column.

6.5 Results on disordered SU(3) spin chains

In this section we present the exact diagonalization results for the disordered SU(3) spin chain. Without using any symmetries, matrices of spin chains of size L would scale as 3^L .

We however make full usage of the $SU(3)$ symmetry, following the construction described in the previous section. This allows us to reach system sizes up to $L = 21$ instead of at best $L = 15$ with computations in the standard $U(1)$ (S^z) basis.

We begin by defining the model and provide some technical details about the system sizes and tableau shapes considered. We then analyze the different indicators for thermalization introduced in the previous sections. These include spectral statistics, distribution of a local observable and the scaling of entanglement entropy. Along the way we compare with the similar indicators studied previously for the $SU(2)$ case [127].

6.5.1 Model and methods

The model we study is the Hamiltonian in Eq. 6.18 with $SU(3)$ symmetry and random couplings on a 1D chain of length L .

$$H_{SU(3)} = \sum_{i=1}^L J_i P_{i,i+1} \quad (6.20)$$

On each site of the chain, the local Hilbert space is 3 dimensional with a local basis $|c_i\rangle$, where $c_i = 1, 2, 3$ denoting the three possible colours of a particle on each site i . The operator $P_{i,i+1}$ permutes the colours between sites i and $i + 1$: $P_{i,i+1} | \dots c_i c'_{i+1} \dots \rangle = | \dots c'_i c_{i+1} \dots \rangle$.

The absolute value of the coupling constants J_i are random variables drawn from the probability distribution

$$P(|J|) = \frac{\alpha \Theta(1 - |J|)}{|J|^{1-\alpha}} \quad (6.21)$$

where α denotes the inverse strength of disorder (the system is more disordered as $\alpha \rightarrow 0$). Furthermore, the sign of J_i is taken to be positive/negative with equal probability, without loss of generality.

Following our arguments from the previous section, $H_{SU(3)}$ can be block-diagonalized in the irreps of $SU(3)$, with each block labelled by a SYT with at most 3 rows. Most of the calculations are carried out for the singlet irreps which correspond to a rectangular tableau of 3 rows. Since this limits us to chain sizes L which are multiples of 3, we also present some calculations for non-singlet tableaux. Table (6.1) provides a description of the chain sizes considered, with the number of sites L , the shape of the Young tableau corresponding to the irrep of $SU(3)$ and the size of the corresponding Hilbert space in this irrep.

We use shift-invert exact diagonalization [170] to obtain eigenstates of $H_{SU(3)}$ in the middle of the spectrum ($\epsilon = 0.5$ in standard notations where $(\epsilon = (E - E_{min}) / (E_{max} - E_{min}))$). The orthogonal unit representation of Ref. [169] is particularly convenient for permuta-

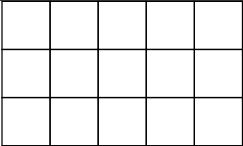

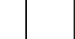

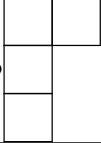
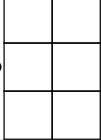
L	Young tableau	Degeneracy	Hilbert space size
15	$(5, 5, 5) = $  $= \bullet$	1	6006
16	$(6, 5, 5) = $  $= \bullet$	3	36,036
17	$(7, 5, 5) = $  $= \bullet$	6	136,136
18	$(6, 6, 6) = $  $= \bullet$	1	87,516
19	$(7, 6, 6) = $  $= \bullet$	3	554,268
21	$(7, 7, 7) = $  $= \bullet$	1	1,385,670

Table 6.1: Chain samples used in this work, with the number of sites L , the shape of the Young tableau corresponding to the irrep of $SU(3)$ (we use the simplified notation where the symbol \bullet stands for the first $(5, 5, 5)$ tableau), the degeneracy of this irrep in the spectrum of $H_{SU(3)}$, and the size of the Hilbert space in this sector.

tion operators $P_{i,i+1}$ as one obtains a sparse matrix representation of the Hamiltonian in Eq. 6.20 when open boundary conditions are used. This allows us to use efficient sparse linear algebra techniques in the shift-invert method. For periodic boundary conditions, the matrices are less sparse with roughly twice as many non-zero elements, which prevents us from reaching large sizes. We are able to simulate open chains with up to $L = 21$ sites (with singlet Hilbert space size of 1,386,670). For each irrep considered and for each disorder strength α , we use at least 1000 disorder realizations, except for the $L = 21$ singlet tableau where we could only use 300 disorder realizations due to the large simulation time required. For each disorder realization, we collect between 50 and 100 eigenstates near $\epsilon = 0.5$, which we refer to below as mid-spectrum eigenstates.

6.5.2 Spectral statistics

We begin our analysis with the gap ratio r as defined in Eq. 6.12. Finite-size dependence of the mean gap ratio shown in Fig. 6.1 clearly indicates that for large enough $\alpha \geq 0.8$, the system will become thermal as system size increases. For the largest size $L = 21$, we can clearly observe statistics very close to the GOE prediction for $\alpha \geq 1.6$. For the disorder values $\alpha = 0.45, 0.6$, the singlet tableaus strikingly show almost no system size

dependence with a mean value between the Poisson and thermal values ($\langle r \rangle_{GOE} \simeq 0.5307$ and $\langle r \rangle_{Poisson} = 2 \ln(2) - 1 \simeq 0.386$). The non-singlet tableaux however show a slight finite-size tendency toward thermal behaviour for $\alpha = 0.6$. Finally, the behaviour for the strongest disorder $\alpha = 0.3$ is marked by unusually low values, even below the Poisson limit, except for the largest system size $L = 21$. This behaviour was also found in the $SU(2)$ case for the same value of α and is attributed to cutting-bond effects (small J values tend to effectively cut the chain in two, resulting in almost degeneracies and low values of gap ratio). This effect should disappear with system size, which is what we indeed observe.

Similar data for the $SU(2)$ case [127] display a remarkable non-monotonous behaviour (a decrease with small system size, followed by an increase on larger sizes) of gap ratios for two intermediate values of disorder $\alpha = 0.8, 1.0$, with a minimum for chain sizes in the range $L \in [14, 18]$ which corresponds to Hilbert space sizes between 429 and 4862. We do not observe this behaviour, except possibly for $\alpha = 0.6$. We have also checked that it does not occur for smaller chain sizes than the smallest size $L = 15$ (Hilbert space size 6006) presented in Fig. 6.1, even though we are limited by the fact that there are not many possibilities available for this range of Hilbert space sizes for $SU(3)$. It is also possible that this non-monotonous effect could arise at a larger length scale $L > 21$ for $\alpha = 0.45$.

Fig. 6.2 offers a comparison of the probability distribution $P(r)$ for $L = 18$ singlet eigenstates for the various strengths of disorder α , to the limiting cases of the thermal distribution $P^{GOE}(r) = \frac{27(r+r^2)}{4(1+r+r^2)^{5/2}}$ and Poisson distribution $P^{Poisson}(r) = 2/(1+r)^2$. For the strongest disorder $\alpha = 0.3$, the distribution is very close to Poissonian except for low r where it exhibits a sub-Poissonian values $P(0) > 2$, corresponding to effective level attraction and low values of mean gap ratio, which can again be explained by the cut-chain effects. For larger disorder $\alpha = 0.45, 0.6$, the distributions display a maximum for finite small values of r , and are thus markedly different from Poisson, even though their large r behavior then closely joins the Poisson tail. For larger values, a crossover is observed towards the thermal distribution which is reasonably well reproduced for $\alpha = 1.6$ and $\alpha = 1.9$.

In the inset of Fig. 6.2, we analyze the level repulsion effect in more detail, by considering the finite-size dependence of $P(r \geq 0.04)$ (as a proxy to $P(0)$) for all values of α for singlet tableau ($L = 15, 18, 21$). The dependence is very similar to the one of mean gap ratio statistics: for $\alpha \geq 0.8$, there is clear evidence of level repulsion in the thermodynamic limit (as $P(0)$ decreases) whereas for $\alpha = 0.45, 0.6$, $P(0)$ seems approximately constant within the range of studied sizes. Finally the cutting-chain effects at very strong disorder $\alpha = 0.3$ manifest in values of $P(0)$ larger than the Poisson value $P(0) = 2$, but this effect disappears as the system size is increased.

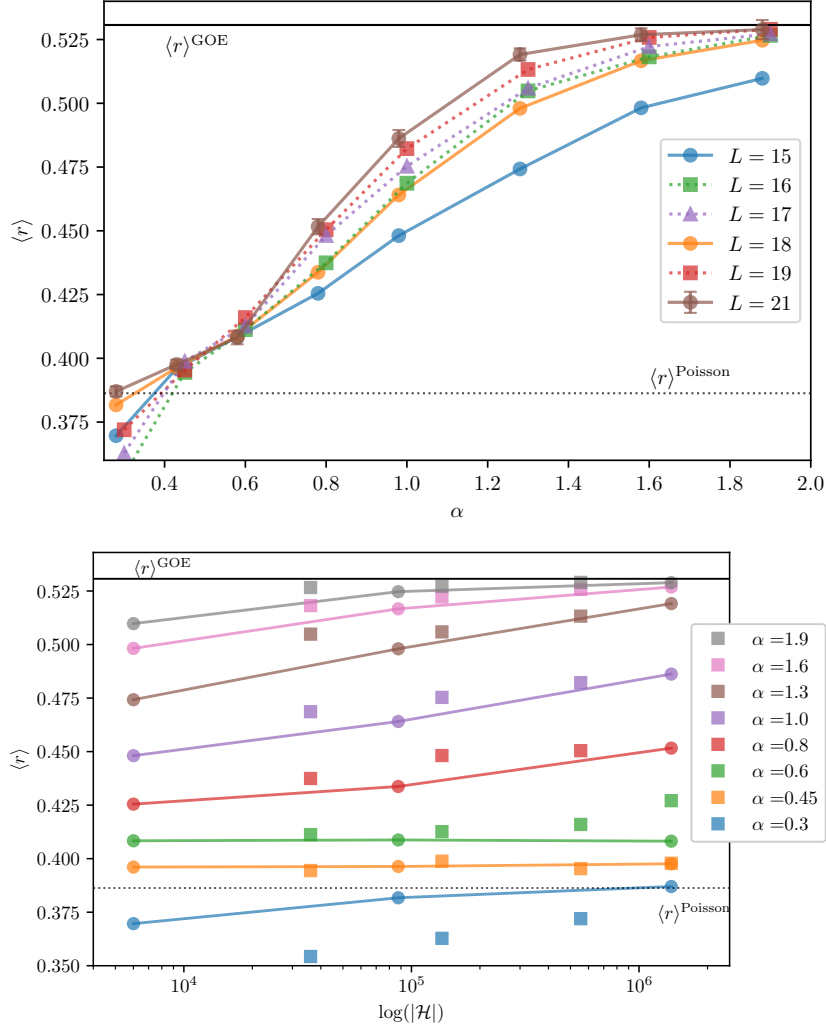


Figure 6.1: Top: Average gap ratio as a function of (inverse) disorder strength $\alpha \in \{0, 3.045, 0.6, 0.8, 1, 1.3, 1.6, 1.9\}$ for different chain lengths L . Solid lines represent data for singlet tableau (chains of size $L = 15, 18, 21$) and dashed lines are for non-rectangular tableau (see Table 6.1). Data for singlet tableaux have been slightly shifted to the left ($\alpha \rightarrow \alpha - 0.02$) for readability purposes. Error bars are smaller than symbol size, except for $L = 21$ where they are explicitly given. The two limiting values $\langle r \rangle^{\text{GOE}}$ and $\langle r \rangle^{\text{Poisson}}$ for respectively thermal and Poisson statistics are also given. Bottom: Similar data, but as a function of the size of the Hilbert space $|\mathcal{H}|$ (in logarithmic scale) for different disorder parameter α . Statistics for eigenstates in the singlet sector are joined by a solid line.

The conclusion of the gap ratio analysis is that systems with strong disorder ($\alpha \leq 0.6$) clearly manifest evidence of non-thermal behavior for the system sizes $L \leq 21$ studied, which cannot be attributed to very small values of bond coupling that will tend to artificially increase level repulsion, falsely mimicking Poisson statistics (this effect is observed for $\alpha = 0.3$ and its finite-size dependence understood). Indeed the distributions of $P(r)$ in this non-thermal regime are not Poissonian, especially at low values of r . The broad ex-

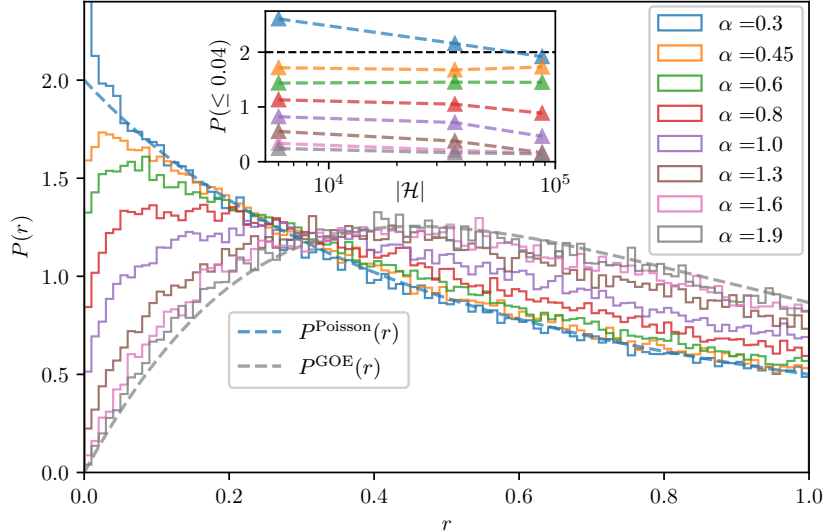


Figure 6.2: Probability distribution of gap ratio $P(r)$ for different disorder strengths for a $L = 18$ chain. The dashed lines present the reference Poisson and GOE (thermal) distributions for comparison. Inset: Hilbert space size dependence of the level repulsion effect $P(0)$ (as approximated by $P(r \geq 0.04)$) for the same values of disorder.

tent of Hilbert space sizes (from 10^3 to 10^6) for $\alpha = 0.45$ over which the spectral statistics do not show tendency to either thermalization or Poisson behavior is quite remarkable.

6.5.3 Distribution of local observable

We now proceed to results for the distribution of a local observable $\langle \alpha | \mathcal{O} | \alpha \rangle$ with $|\alpha\rangle$ mid-spectrum eigenstates. More specifically we consider the local permutation operator $\mathcal{O} = P_{i,i+1}$ between sites i and $i+1$, analogous to $S_i \cdot S_{i+1}$ in the $SU(2)$ case. The left panels of Fig. 6.3 show the distribution where $P_{i,i+1}$ is measured for $i = i_{\max}$ for the strongest coupling $J_{i,i+1} = J_{\max}$ in the chain, the middle panels for i the further away from this strongest coupling $(i_{\max} + L/2) \bmod L$ (which should correspond to a random coupling), and the right panels for the observable averaged over all possible values of $i, i+1$. The data are presented for three different representative disorder values $\alpha = 0.3, 0.8$ and 1.6 and for the largest system $L = 21$. In the limit of very large disorder $\alpha = 0.3$, we observe that the distribution of $\langle \mathcal{O}_{\max} \rangle$ is dominated by two sharp peaks at $\mathcal{O}_{\max} = +1$ and $\mathcal{O}_{\max} = -1$, the latter being approximately half the size of the largest peak. This can be understood by adapting the argument put forward in the RSRG computation for the $SU(2)$ case: in the limit of infinite disorder, the strongest bond is decimated first, and the two fundamental representations of $SU(3)$ are coupled to form either a 2-box symmetric

$\begin{array}{|c|c|} \hline & \\ \hline \end{array}$ (with degeneracy 6 and for which $O = +1$) or antisymmetric $\begin{array}{|c|} \hline \\ \hline \end{array}$ (with degeneracy

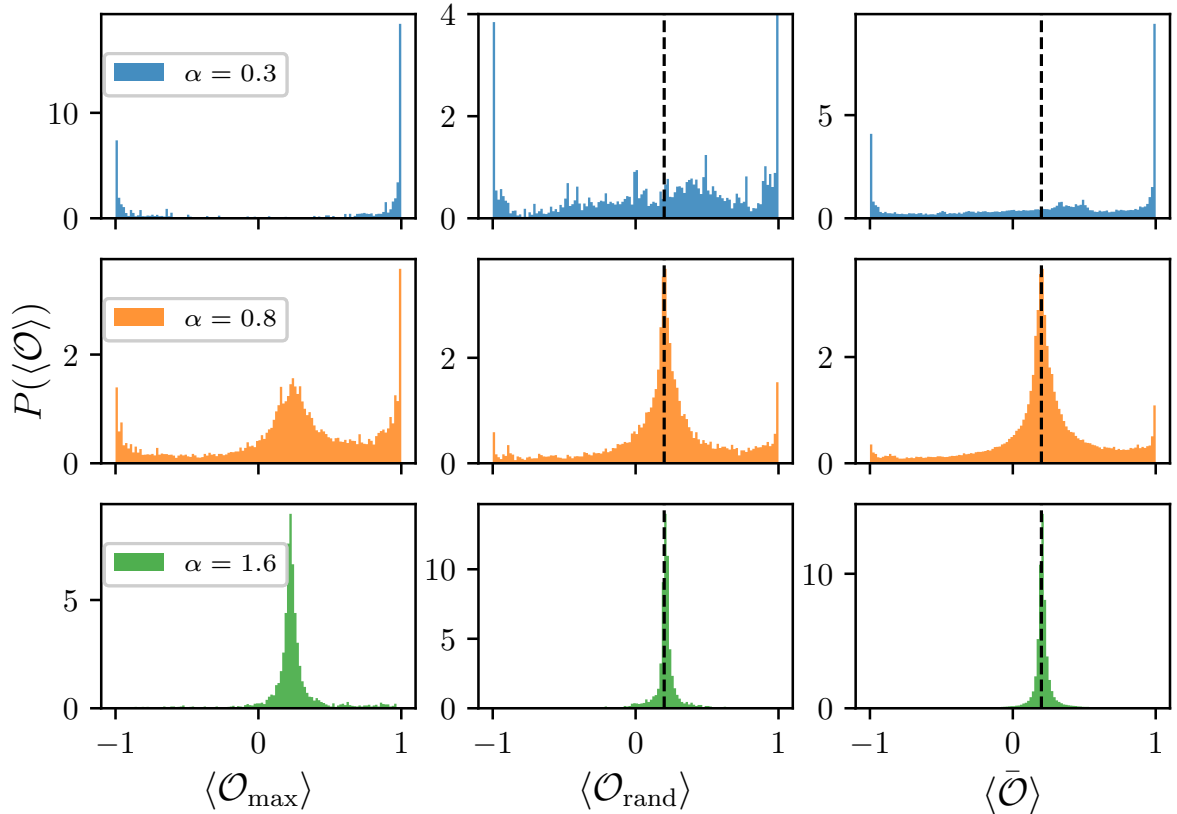


Figure 6.3: Distribution of the local observable $O = P_{i,i+1}$ shown for 3 disorder values $\alpha = 0.3, 0.8, 1.6$ and for system size $L = 21$. Left panel: $\langle \mathcal{O}_{\max} \rangle$, for sites $i_{\max}, i_{\max} + 1$ with the strongest coupling in the chain; middle panel $\langle \mathcal{O}_{\text{rand}} \rangle$, for the site the further away $i = (i_{\max} + L/2) \bmod L$; and right panel the average $\langle \mathcal{O}_{\text{rand}} \rangle$ over all bonds $i, i+1$. The dashed line corresponds to the expected thermal value $\langle \mathcal{O}_{\text{thermal}} \rangle \simeq 0.2$ for $L = 21$, as obtained from a random state, which is quite different from the expected thermodynamical value $1/3$.

3 and $O = -1$) irrep. This explains the two peaks at ± 1 in the distribution $P(\mathcal{O}_{\max})$ and their relative height. The opposite bond $(i_{\max} + L/2) \bmod L$ would be decimated later in the decimation procedure, resulting in intermediate values with nevertheless the most likely values being again ± 1 . This is exactly what is observed in the top middle panel for $P(\mathcal{O}_{\text{rand}})$ at $\alpha = 0.3$. Finally, the average over all possible bonds (right panel) corresponds to averaging over all levels of decimation, resulting in a distribution $P(\langle \bar{\mathcal{O}} \rangle)$ close to the one for the strongest bond $P(\langle \mathcal{O}_{\max} \rangle)$. We thus find that our data for $P(\langle \mathcal{O} \rangle)$ for the SU(3) case are compatible with the strong disorder scenario advocated at small α in the SU(2) case, namely that eigenstates can be considered (for moderate systems sizes) to be close to those obtained from a strong disorder RSRG procedure.

We now continue with the smallest disorder $\alpha = 1.6$. We observe a close to Gaussian distribution around a most likely value $\mathcal{O}^* \simeq 0.2$, for all three distributions $P(\mathcal{O}_{\max})$, $P(\mathcal{O}_{\text{rand}})$, $P(\bar{\mathcal{O}})$, which as we argue now matches the expectation of ETH. In the thermal

regime and for mid-spectrum eigenstates, the observable should be the average taken uniformly over all the states formed by coupling two fundamental tableaus on sites i and $i + 1$. It is easy to see that this average should be $1/3$ in the thermodynamic limit (and in the general case $1/N$ for $SU(N)$), however for finite (small) systems this may not be exactly the case. Indeed by randomly sampling Hilbert space of finite systems, we find that the expected limit $1/3$ is reached only slowly as $1/L$. More precisely, we find that the expression $\langle \text{Random}(L) | \bar{\mathcal{O}} | \text{Random}(L) \rangle = \frac{1-8/(L-1)}{3}$ fits very well the data for singlet tableaus. In particular, for the singlet size $L = 21$ (singlet tableau), the random sampling provides an average $\langle \bar{\mathcal{O}} \rangle \simeq 0.200$, which is matching very well with the “ergodic” peaks at $\mathcal{O}^* \simeq 0.2$ in Fig. 6.3 for $\alpha = 1.6$.

The situation for the intermediate disorder $\alpha = 0.8$ is very instructive. For random $P(\langle \mathcal{O}_{\text{rand}} \rangle)$ and average $P(\langle \bar{\mathcal{O}} \rangle)$ distributions, the ergodic peak at $\mathcal{O}^* \simeq 0.2$ dominates but a non-zero background for all other possible values of \mathcal{O} is present with peaks at ± 1 . We interpret this as a tendency to ETH for this observable for most eigenstates, with remnants of non-thermal behavior. For the strongest coupling, the distribution $P(\langle \mathcal{O}_{\text{max}} \rangle)$ is trimodal with a central peak at $\mathcal{O}^* \simeq 0.2$, but slightly more dominant peaks at ± 1 , together with the same background of non-zero probability for other values of $\langle \mathcal{O}_{\text{max}} \rangle$. This behavior is also compatible with a tendency to thermalization for this value of α but with a slower convergence / stronger finite-size effect for this observable, which indeed is particular as associated to the strongest bond in the Hamiltonian.

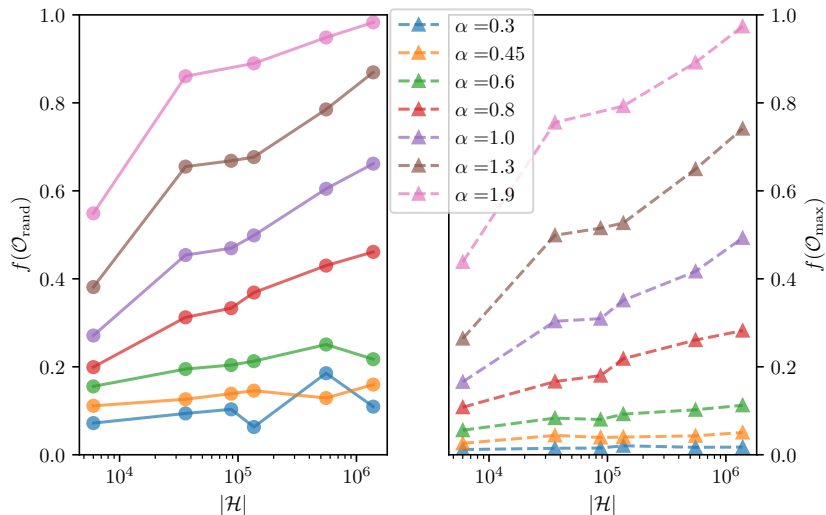


Figure 6.4: Fraction of eigenstates that belong to the central ergodic peak (belonging to the central peak actually means \mathcal{O} in $[\mathcal{O}^* - \delta, \mathcal{O}^* + \delta]$ with $\delta = 1/4$), with $\hat{\mathcal{O}}_{\text{max}}$ in straight lines and $\hat{\mathcal{O}}_{\text{rand}}$ with dashed lines. Different symbols are used for singlet or non-singlet tableaus.

In order to probe finite-size effects for this observable, we consider the scaling (with the size of Hilbert space $|\mathcal{H}|$) of the fraction $f(\mathcal{O})$ of eigenstates which belong to the

“ergodic” peak close to 0.2, similar to what was done in Ref. [127]. We consider the fraction of states which have $\langle O \rangle$ in $[O^*(|\mathcal{H}|) - \delta, O^*(|\mathcal{H}|) + \delta]$, with $O^*(|\mathcal{H}|)$ the most probably value obtained from a random-state sampling and where $\delta = 1/4$ (as chosen to be able to make a comparison with Ref. [127] which considers $\delta = 1/8$ for an observable in the range $[-3/4, 1/4]$). Our results in Fig. 6.4 are compatible with a fraction of eigenstates belonging to the thermal peak that tends to 1, as predicted by ETH, for all values of $\alpha \geq 0.6$, for both \mathcal{O}_{\max} and $\mathcal{O}_{\text{rand}}$, with different speeds of convergence. For the two strongest disorders, we find an overall very slight tendency for this fraction to increase with Hilbert space size, albeit obscured by a finite-size and Young tableau shape dependence. It is clear nevertheless that on these small system sizes, the ETH prediction $f \rightarrow 1$ is far from being reached since $f < 0.2$ for $\alpha \leq 0.6$, meaning that the eigenstates are clearly non-thermal for these ranges of L and disorder α . This is overall in agreement with the existence of a finite-size regime with non-thermal behavior for this SU(3) disordered system. Comparing to SU(2) disordered chains with the same Hilbert space sizes (see Fig.9 in Ref. [127]), we find similar ergodic fractions for $\alpha = 0.6, 0.8$, and SU(2) systems being very slightly more thermal than SU(3) systems for $\alpha = 1.0$.

6.5.4 Scaling of entanglement entropy

We present results of entanglement entropy (as defined in section 6.1.3 and following Ref. [172] for its computation in the orthogonal basis unit, see also appendix A.2) for the non-degenerate singlet mid-spectrum eigenstates of the largest system we could simulate (system size $L = 21$) as a function of block size L_A in Fig. 6.5. The results are symmetric with respect to inversion of L_A and $L_B = L - L_A$, thus we only show data up to $L_A = 10$. For small disorder (large $\alpha \geq 1.3$), the entanglement entropy follows a very clear volume law scaling (with S growing linearly with the block size, see top panel of Fig. 6.5), with a coefficient matching with the expected Page [133, 171] behavior obtained by considering the entanglement entropy of random vectors (distributed on the Haar sphere), presented as a solid line in Fig. 6.5. For intermediate disorder $\alpha = 0.8, 1.0$, the growth of entanglement appears linear for small L_A but data bends as L_A reaches $L/2$, due to the finite-size limitation. For larger disorder (particularly for $\alpha = 0.3, 0.45$), we observe a slow growth of entanglement, which we find compatible with a logarithmic growth, within the system sizes that can be addressed (see bottom panel of Fig. 6.5 where fits to logarithmic scaling of $S(|n\rangle)$ are shown). This contrasts not only with the volume law at large α , but also with a strict area law expected for standard MBL eigenstates. This logarithmic “subthermal” behavior has been predicted for the entanglement entropy in the intermediate, finite-size, regime of SU(2) disordered chains by the RSRG calculations [173, 127], but was not strictly speaking observed in the finite-size exact diagonalization results of

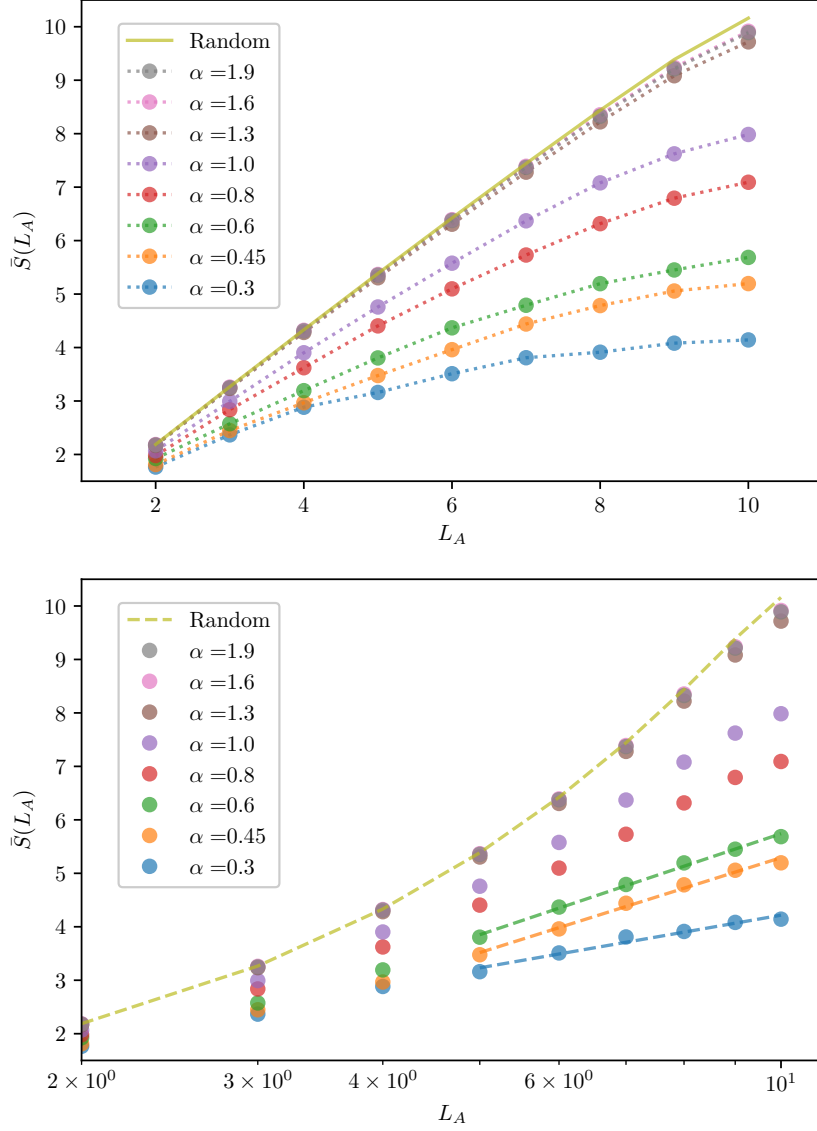


Figure 6.5: Both panels represent entanglement entropy S of mid-spectrum eigenstates versus block size L_A , as a function of disorder parameter α and for a chain with $L = 21$ sites. The solid line is the result for a wave-function on a similar $L = 21$ size with Gaussian-distributed coefficients, corresponding to the Page [171] entanglement volume law. Top panel: linear scale for the block size L_A , with dashed lines represent guides to the eye. Bottom panel: logarithmic scale for L_A . The dashed lines are fits to a logarithmic scaling $S(L_A) = a + b \log(L_A)$ for the three strongest disorders and $L_A \in [5, 10]$.

Ref. [127].

6.6 Conclusion

Through the lens of various indicators (spectral statistics, expectation values of local observables, entanglement entropy), we examined the behavior of mid-spectrum eigenstates

for disordered chains with the non-abelian $SU(3)$ symmetry. While the data at weak disorder perfectly match the expectations for a thermal phase, our numerical analysis on finite sizes at strong disorder (small values of α) point towards a non-thermal regime.

Could our data be interpreted as signatures of a phase transition from a (standard) MBL phase (or regime) to a thermal phase at a small value of, say around $\alpha = 0.45$, similar to the interpretation of similar data in the standard MBL model [124]? We believe this is not the case for the following reasons: first, there is no regime where the spectral statistics exhibit perfect Poisson statistics. The level repulsion at $P(0)$ is either sub-Poissonian (for $\alpha = 0.3$) on the system sizes considered, or already non-Poissonian for the nearby disorder strength $\alpha = 0.45$. Second, even at very large disorder $\alpha = 0.3$, the distribution of expectation values of local observable has a non-zero background for some local observable (such as $\mathcal{O}_{\text{random}}$ in top middle panel of Fig. 6.3). Finally, the entanglement entropy displays a behavior compatible with a logarithmic growth (as a function of block size) in the region $\alpha = 0.3 - 0.6$. While it is hard to distinguish a log from a small power-law, our data rule appear to clearly rule out an area law that standard MBL eigenstates would follow.

We thus interpret our data as completely compatible with the existence of a non-thermal, finite-size, regime in the region $\alpha \approx [0.3, 0.6]$ for systems below an ergodic length scale $L^{*,SU(3)}$, similar to the $SU(2)$ situation predicted by the RSRG computation [127, 173]. It is difficult to conclude on whether the thermal length scale $L^*(\alpha)$ above which the system converges to the ETH is larger for $SU(3)$ systems than $SU(2)$. The gap ratio data do not explicitly show a minimum behavior (except maybe for $\alpha = 0.6$) as in the $SU(2)$ case which would help identifying this length scale. We believe this is mostly due to the lack of systems with intermediate Hilbert space sizes which could help visualizing this behavior. On the other hand, the very slightly more thermal data for the fraction of thermal eigenstates for $SU(2)$ for fixed Hilbert space size can possibly and at best indicate that $L^{*,SU(3)}(\alpha = 1) \gtrsim L^{*,SU(2)}(\alpha = 1) \ln(2)/\ln(3)$, which is not predictive. The overall agreement of the evidence of non-thermal data for $\alpha = 0.3, 0.45$, and intermediate behaviour for $\alpha = 0.6, 0.8$ in a similar range of system sizes for $SU(2)$ (Ref. [127]) and $SU(3)$ (our data) point towards the hypothesis that these two length scales are probably very similar $L^{*,SU(3)}(\alpha) \sim L^{*,SU(2)}(\alpha)$. It would be very interesting, albeit more involved, to have RSRG predictions for the $SU(3)$ case for this length scale, as well as in general to compare to our exact diagonalization data when possible.

Chapter 7

Conclusion

In this conclusion, we provide overall perspectives opened by the works presented in this thesis, giving suggestions chapter by chapter.

In Chapter 4, we explored the finite temperature phase diagram of the QDM on the square lattice and showed an unusual re-entrance effect in the lines of constant g in the critical phase. We also studied the phase transitions out of the critical phase to low temperature crystalline orderings of dimers (columnar and staggered). We show that the phase transition on the columnar side could be understood by the same Sine-Gordon field theory as the Classical Interacting Dimer Model. This phase diagram was obtained by supplementing the SCA with a classical loop move rendering it ergodic at finite temperature. Our finite temperature improvement of the SCA still presents a bottleneck to ergodically sample at lower temperature. A possible way forward could be to use a better set of transition probabilities for the classical directed loop move, which have lower bounce back rates. It would be interesting to understand the behaviour of the critical lines starting from $T = 0$ by performing some perturbative expansion near the RK point. This could allow us to understand if the observed reentrant behaviour is linked to the $U(1)$ like behaviour observed at low energies near the RK point [174, 175] and make connections with the critical lines obtained by a high temperature expansion shown above. The Sweeping Cluster Algorithm described in Chapter 3 could in principle be extended to study other quantum constrained models. So far the algorithm has been successfully used on models with hard-core dimer or loop constraint. It would be interesting to explore how the algorithm performs for a different class of constrained models, for example a model of hard-core bosons with ring exchange interactions [176], which has been proposed as a possible candidate model to host a Exciton Bose Liquid phase [177]. More insight could be obtained for the algorithm by studying the statistical properties of the clusters it creates in SSE, an analogous study has been performed for the worm/directed

loop algorithm [178].

In Chapter 5 we investigated the finite-temperature phase diagram of a classical model of fully-packed loops on the square lattice with attractive local interactions between loop segments. With the help of a directed-loop Monte Carlo algorithm and a field theoretical analysis based on a height description of loop configurations, we are able to locate the finite temperature Kosterlitz-Thouless transition, separating a critical phase at $T > T_{KT}$ and a nematic phase below T_{KT} . We find that in the loop model the anomalous dimension at the KT transition $\eta_D = 1$ is four times larger than that in the classical dimer model [47]. The high-temperature critical phase is fully characterized by the temperature dependence of the Coulomb gas constant presented in Fig.5.14, which is obtained using several different concurrent estimates. We now connect our results to the quantum loop model on the square lattice. From our analysis, we expect that the QLM on the square lattice should also host a critical phase at any sufficiently high-temperature parametrized by a Coulomb gas constant $g(T/t, V/t)$ which depends on temperature and potential energy, similar to the quantum dimer model [179]. At large negative ratio of potential to kinetic energy ($V/t \ll 0$), the QLM hosts a nematic ground-state. From our results, we conclude that the finite-temperature phase transition to the nematic phase in the QLM should occur as a Kosterlitz-phase transition that can be described using the same analysis provided here. The QLM also hosts a plaquette ground-state in a finite range of $-0.35 \lesssim V/t \ll 1$ [88]. We believe that the finite-temperature phase transition to this plaquette phase should be of KT type too, with an effective action described by Eq. 5.2 but with *negative* $\mathcal{V} < 0$, as the two plaquette ground-states have average height $\bar{h} = 0, \frac{1}{2}$. It would be interesting to find a classical model with a similar phase transition and low-temperature phase. We note that the directed loop algorithm that we use can be directly implemented as a new move (as described in Chapter 3) within the sweeping cluster algorithm for the QLM, allowing to study its finite-temperature phase diagram fully taking into account the loop constraints and winding fluctuations.

In the final chapter of the thesis, we studied a disordered $SU(3)$ symmetric spin chain using exact diagonalization. We showed that for finite system sizes and for a certain range of disorder strengths, the model hosts a non-ergodic regime with eigenstates having a logarithmic scaling of entanglement entropy. The results are in agreement with the general arguments forbidding a true MBL phase for systems with non-abelian symmetries [180] as well as the recent dynamical study [165] on the same $SU(3)$ systems (performed on larger system sizes, up to $L = 48$, but at finite time $t_{max} = 500$) which also find a sub-thermal behavior for disorder values $\alpha = 0.3$ and $\alpha = 0.5$. This dynamical analysis indicates a slightly more thermal behavior for $SU(3)$ than for $SU(2)$, for these values of α and lengths. We exploit entirely the $SU(3)$ symmetry by performing exact diagonalization in each irrep thanks to the use of the orthogonal unit basis introduced in Ref. [169]. This basis could be employed to systems with $SU(4)$ symmetry: for singlet eigenstates,

system sizes $L = 16$ and $L = 20$ are reachable within shift-invert computations. Another interesting application of the orthogonal unit basis (which allows for diagonalization or time-evolution of larger systems than in the standard $U(1)$ basis) would be to test in detail recent predictions of a non-abelian version of the ETH [181, 182], which has been argued to present different finite-size convergence to the thermal ensemble than the standard ETH.

In conclusion, this thesis has delved into various aspects of quantum and classical constrained models shedding light on their finite temperature phase transitions and critical behaviour. It also gives valuable insight in the interplay of non-abelian symmetries and thermalization in an isolated quantum many-body system by studying a disordered $SU(3)$ symmetric spin chain.

Chapter 8

Résumé en Français

8.1 Introduction

L'objectif de cette introduction est de souligner l'importance de l'étude des modèles contraints en physique de la matière condensée et en physique statistique en décrivant diverses situations dans lesquelles ils émergent en tant que modèles effectifs capturant la physique à basse énergie. Notre attention se portera sur les modèles avec une contrainte de dimère ou de boucle.

Les modèles de dimères ont été largement étudiés en physique statistique classique. Introduit comme un modèle simple pour l'adsorption de molécules diatomiques sur des surfaces cristallines [1], le modèle de dimères a attiré l'attention après que Kasteleyn [2] a donné une solution exacte à la fonction de partition, qui attribue des fugacités aux dimères sur chaque type de liaison du réseau (voir Fig.8.1 pour une illustration). Dans sa forme la plus simple, la fonction de partition se réduit à énumérer exactement toutes les configurations possibles de dimères sur le réseau. Le problème ressemble en fait également aux problèmes de pavage de dominos en mathématiques. En plus de Kasteleyn, une solution exacte indépendante a également été donnée par Temperley et Fisher [3] à la même époque. Cependant, dans la version de Kasteleyn, l'attribution de fugacités sur les liaisons aux dimères a donné lieu à une transition de phase particulière dans laquelle la chaleur spécifique en dessous de la température de transition T_K est nulle tandis qu'au-dessus de T_K , elle est non nulle et diverge comme $(T - T_K)^{-1/2}$. Ceci montre un contraste marqué avec un autre modèle exactement soluble familier, le modèle d'Ising 2D, où la chaleur spécifique a une divergence logarithmique. Cette classe de transitions de phase est maintenant appelée transitions de phase de type Kasteleyn. Notons que le dénombrement exact des configurations de dimères ne fonctionne que sur des graphes planaires.

Une des contributions les plus significatives des modèles de dimères réside dans leur équivalence avec d'autres modèles physiques importants. Prenons par exemple le modèle d'Ising classique sur le réseau triangulaire avec des couplages antiferromagnétiques. Comme c'est un modèle frustré, l'état fondamental est un ensemble étendu de différentes configurations de spin dégénérées. La Fig.8.1 montre comment chaque configuration de spin peut être représentée par une configuration de dimères sur un réseau dual hexagonal. Comme nous le verrons dans le prochain chapitre, les configurations de dimères sur des réseaux bipartites sont critiques, c'est-à-dire qu'elles présentent des corrélations décroissantes en loi de puissance. Ce *mapping* permet de révéler les corrélations critiques spin-spin dans le modèle frustré [4]. Les *mappings* ne se limitent pas à 2D. La phase de Coulomb bien connue observée expérimentalement dans les matériaux de glace de spin [5] pourrait également être comprise par un *mapping* de dimères similaire en 3D [6].

De plus, les modèles de dimères trouvent leur utilisation au-delà des modèles classiques. Un dimère sur une liaison peut représenter un état singulet de spin-1/2 - $1/\sqrt{2}(|\uparrow\downarrow\rangle - |\downarrow\uparrow\rangle)$ de deux spins sur des sites voisins. Un état constitué de tels singulets a été proposé par Anderson comme un mécanisme par lequel un antiferromagnétique quantique pourrait ne pas s'ordonner à longue portée, menant ainsi à une phase liquide de spin [7]. Rokhsar et Kivelson, s'appuyant là-dessus, vont plus loin et considèrent un "gaz de dimères quantiques de coeur dur" qui élimine essentiellement les degrés de liberté de spin.

Dans certains systèmes, les contraintes de boucle apparaissent de manière subtile, comme de nouveaux degrés de liberté dans la fonction de partition, mais fournissent une compréhension beaucoup plus profonde du système. Un exemple familier est la dualité entre les développements à basse et haute température du modèle d'Ising 2D, qui est capturée par leur *mapping* sur le même ensemble de configurations de boucles [9]. Les modèles de boucles apparaissent de manière plus directe dans l'étude des chaînes de polymères et des marches auto-évitantes. En général, la fonction de partition de modèles de boucles prend la forme suivante [10]

$$Z = \sum_{\mathcal{L}} w(\mathcal{L}) t^{L(\mathcal{L})} \quad (8.1)$$

où \mathcal{L} désigne une seule configuration de boucles sur un réseau, $L(\mathcal{L})$ est la longueur totale de toutes les boucles dans \mathcal{L} et $w(\mathcal{L})$ est le poids attribué à la configuration de boucle \mathcal{L} qui peut dépendre de ses propriétés topologiques. Les configurations de boucles \mathcal{L} sur un réseau peuvent être divisées en différentes catégories selon si les boucles se croisent ou non, si chaque site du réseau est visité par une boucle ou non (ceux-ci sont appelés modèles de boucles *fully packed*) et parfois les boucles peuvent se voir attribuer un degré

de liberté de "couleur". Par exemple, la classe de modèles de boucles la plus largement étudiée appelée modèles de boucles $O(n)$ [11] s'écrit $w(\mathcal{L}) = n^{\mathcal{N}}$ où \mathcal{N} est le nombre de boucles dans une configuration \mathcal{L} . Le nom vient de leur *mapping* sur des modèles $O(n)$ sur un réseau hexagonal.

Plus important encore, les modèles de boucles sont largement utilisés pour étudier les phénomènes critiques - la Fig.8.1 représente des boucles qui sont les murs de domaine du modèle d'Ising au point critique. En raison de leur nature critique, ces modèles peuvent être étudiés à l'aide d'outils analytiques pour les phénomènes critiques tels que le formalisme du gaz de Coulomb [12], la théorie des champs conforme ou l'évolution de Schramm-Loewner [13].

Comme nous le verrons au chapitre 5, les modèles de boucles sont intrinsèquement liés à une autre classe de modèles contraints appelés modèles de vertex. Le plus connu d'entre eux est le modèle à six vertex [14, 15], et se trouve au centre de l'attention dans de nombreux modèles de physique statistique et de physique de la matière condensée. Dans ses premières utilisations, le modèle à six vertex a été introduit pour comprendre l'entropie de la glace d'eau (cette classe de modèles est également appelée modèles de la glace) et les transitions de phase dans les ferroélectriques. Lieb a résolu exactement la fonction de partition en utilisant les méthodes de l'ansatz de Bethe pour un cas spécial qui attribuait des poids égaux à toutes les configurations de vertex, Baxter a ensuite donné une solution exacte dans le cas général en utilisant ce qui est maintenant connu sous le nom d'équation de Yang-Baxter [16].

Modèles contraints sur les simulateurs d'atomes de Rydberg

Les progrès technologiques permettant de piéger individuellement des atomes par laser sur des réseaux optiques ont conduit à une récente vague de réalisation d'Hamiltoniens quantiques à plusieurs corps sur des simulateurs quantiques programmables [17]. Cela renvoie à l'idée proposée par Richard Feynmann d'utiliser un système quantique pour résoudre un problème quantique.

Les états de Rydberg sont des états atomiques avec un grand nombre quantique principal n . De tels états ont de longues durées de vie qui varient comme n^3 , en raison de cela on peut essentiellement traiter un atome de Rydberg comme un système à deux niveaux avec un état fondamental $|g\rangle$ et un état excité $|r\rangle$ appelé un état de Rydberg. Pour deux atomes de Rydberg séparés par une distance R , les excitations simultanées vers l'état de Rydberg $|rr\rangle$ ont un coût énergétique qui varie comme $\Delta E = C_6/R^6$. Cela implique qu'en dessous d'une certaine distance critique $R_b = (C_6/\hbar\Omega)^{1/6}$ appelée le *rayon de blocage*, on ne peut pas avoir d'excitations simultanées de deux atomes de Rydberg. Ω ici est la fréquence d'oscillation de Rabi introduite par le piège laser.

Considérons le Hamiltonien suivant pour des atomes de Rydberg piégés sur un réseau

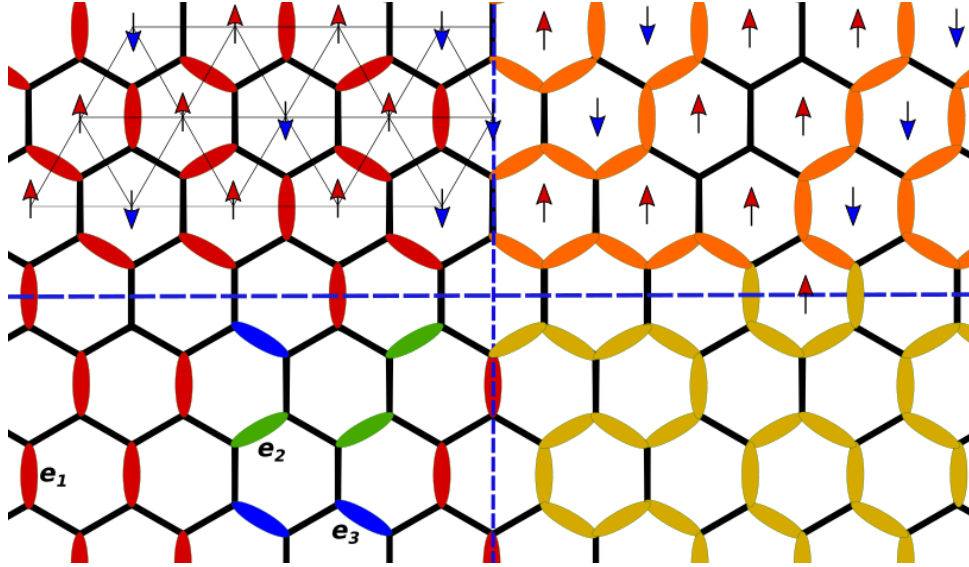


Figure 8.1: En haut à gauche : Mapping des états fondamentaux du modèle d'Ising antiferromagnétique sur le réseau triangulaire vers des pavages de dimères du réseau hexagonal dual. Un dimère est attribué à la liaison qui traverse le lien de deux spins orientés vers le haut. En bas à gauche : les dimères représentent des molécules diatomiques sur une surface cristalline hexagonale. Trois orientations différentes des dimères se voient attribuer différentes fugacités. En haut à droite : Mur de domaine de spins vu comme une boucle. Ici, le modèle de boucle est non compact (non *fully packed*) car certains sites du réseau n'ont aucune boucle qui les traverse. En bas à droite : un modèle de boucle *fully packed* sur le réseau hexagonal.

optique,

$$H_{\text{Rydberg}} = \sum_{i=1}^N \frac{\Omega}{2} (|g\rangle_i \langle r| + |r\rangle_i \langle g|) - \delta |r\rangle_i \langle r| + \frac{1}{2} \sum_{(i,j)} V(|\mathbf{r}_i - \mathbf{r}_j|/a) |r\rangle_i \langle r| \otimes |r\rangle_j \langle r| \quad (8.2)$$

Les paramètres Ω et δ sont la fréquence d'oscillation de Rabi et le désaccord du champ laser cohérent. Le potentiel $V(x) = C_6/x^6$ est l'interaction de Van der Waals entre deux atomes de Rydberg. a ici est l'espacement du réseau. Comme mentionné précédemment, il existe un rayon de blocage R_b qui dépend de Ω , de telle sorte qu'il ne peut pas y avoir d'excitations simultanées de deux atomes de Rydberg dans ce rayon. On a un contrôle sur la portée de ce blocage en changeant simplement l'espacement du réseau a .

Nous pouvons voir que pour des valeurs très grandes et négatives de δ/Ω , il est favorable énergétiquement que tous les atomes soient dans l'état fondamental $|g\rangle$. Pour des valeurs très positives de δ/Ω , tous les atomes devraient être dans leur état excité, mais le blocage des Rydberg introduit maintenant des contraintes sur le nombre pouvant être simultanément excités. Cela conduit à certains *ordres cristallins de Rydberg* selon la portée du blocage, qui peut être contrôlée par le rapport R_b/a .

Considérons maintenant un réseau d'atomes de Rydberg sur un réseau Kagome. La Réf.([20]) montre que dans la limite du désaccord élevé, l'équation (8.2) peut être ap-

proximée par un modèle de bosons de cœur dur sur le réseau Kagome. En utilisant ce *mapping*, on peut identifier les ordres cristallins de Rydberg par des ordres de dimères ou de boucles sur le réseau triangulaire construit en connectant les centres des hexagones du réseau Kagome, voir Fig.8.2.

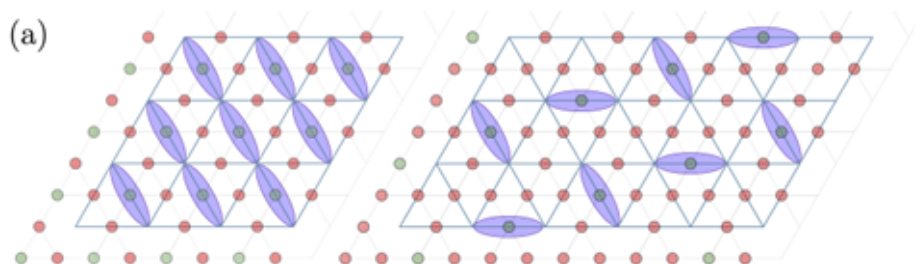


Figure 8.2: Atomes de Rydberg sur le réseau Kagome. Chaque atome excité (indiqué en vert) est représenté par un dimère sur le lien correspondant du réseau triangulaire. L'image de gauche montre un état de boucle nématique tandis que l'image de droite montre un arrangement alterné de dimères. L'image est tirée de [20].

Considérons maintenant que les atomes de Rydberg se trouvent sur les liens du réseau Kagome. Si nous associons un dimère à un atome de Rydberg excité sur ce lien (voir Fig.8.3), les auteurs de la référence ([21]) montrent qu'il est possible de préparer avec une grande fidélité une superposition égale de recouvrements de dimères du réseau Kagome pour 219 atomes de Rydberg. Étant donné qu'un tel état est un liquide de spin quantique, ils sondent également ses diverses excitations topologiques. Des travaux très récents ont

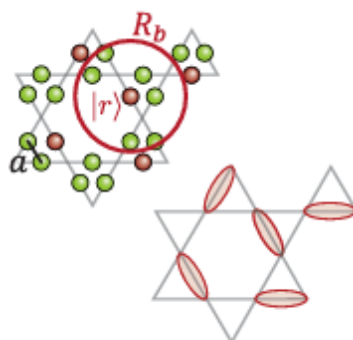


Figure 8.3: Atomes de Rydberg sur les liens du réseau Kagome. Les atomes rouges sont dans l'état excité $|r\rangle$, et à l'intérieur du rayon de blocage R_b , tous les atomes verts sont dans l'état fondamental $|g\rangle$. Un dimère est placé sur chaque atome excité. La figure est tirée de [21].

proposé de réaliser avec des réseaux d'atomes de Rydberg des modèles de dimères sur des réseaux carrés et triangulaires [22], ou même avec d'autres types de contraintes comme des trimères [23] montrant un ordre topologique \mathbb{Z}_3 .

Les réseaux d'atomes de Rydberg permettent de sonder un phénomène assez différent de la physique quantique à plusieurs corps, à savoir la possibilité d'échapper à la thermalisation (rupture d'ergodicité). Ici encore, les contraintes jouent un rôle crucial. Une expérience emblématique qui a observé le phénomène de rupture d'ergodicité a utilisé des atomes de Rydberg piégés sur des chaînes allant jusqu'à 51 atomes [24]. Le blocage était réglé de telle sorte que deux atomes voisins ne pouvaient pas être dans l'état excité en même temps. Cela formait essentiellement un espace de Hilbert contraint dans lequel des états comme $|\dots rr\dots\rangle$ sont énergétiquement interdits. En réalisant une expérience de quench, les auteurs observent que, en partant d'un état initial de type Néel, $Z_2 = |rgrgrg\dots\rangle$, le système oscille dans le temps entre Z_2 et son homologue inversé, c'est-à-dire $|grgrgr\dots\rangle$. Ce comportement de (quasi-)retour à l'état initial habituellement observé pour la précession d'un seul spin dans un champ magnétique est surprenant pour un système à plusieurs corps.

Le modèle contraint paradigmatique qui a pu expliquer les reprises ci-dessus et également capturer divers mécanismes pouvant conduire à une rupture d'ergodicité faible est le modèle PXP [25]. Le modèle est une chaîne 1D d'atomes de Rydberg à deux niveaux comme précédemment avec le Hamiltonien suivant :

$$H_{PXP} = \sum_i P_{i-1} \sigma_i^x P_{i+1} \quad (8.3)$$

où, $\sigma_i^x \equiv |g_i\rangle\langle r_i| + |r_i\rangle\langle g_i|$ et $P_i \equiv |g_i\rangle\langle g_i|$ projettent à l'état fondamental sur les atomes voisins. Comme on peut le voir, le Hamiltonien impose essentiellement la contrainte selon laquelle aucun des atomes voisins ne peut être dans l'état excité. Les simulations numériques de la dynamique de quench sur le modèle PXP montrent le comportement de retour à l'état initial est observé non seulement pour l'état initial Z_2 mais aussi pour $Z_3 = |rggrggr\dots\rangle$ [26]. Le modèle héberge également quelques états propres spéciaux qui montrent une variation logarithmique de l'entropie d'intrication [26], une caractéristique de la rupture d'ergodicité faible.

8.2 Diagramme de phase à température finie du modèle de dimères quantiques sur le réseau carré

Dans cette section, nous résumons les résultats obtenus sur le diagramme de phase à température finie obtenu pour le modèle de dimères quantiques de Rokhsar-Kivelson sur le réseau carré. L'espace de Hilbert pour l'Hamiltonien est constitué de pavages de dimères complets du réseau carré, comme illustré dans la Fig.8.4. Ils satisfont une contrainte de cœur dur selon laquelle un et un seul dimère touche un site du réseau.

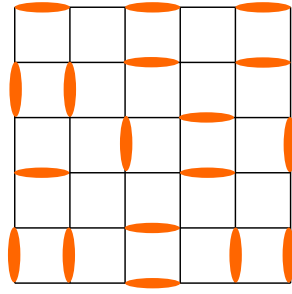


Figure 8.4: Un pavage de dimères complet (*fully packed*) du réseau carré.

Le Hamiltonien est donné par

$$H_{QDM} = \sum_{\square} -t (|\square\rangle\langle\square| + |\square\rangle\langle\square|) + V (|\square\rangle\langle\square| + |\square\rangle\langle\square|) \quad (8.4)$$

Ici, la sommation porte sur toutes les plaquettes du réseau carré. L'hamiltonien se compose des deux termes suivants :

- *Terme cinétique* : il s'agit de la partie *hors-diagonale* de H_{QDM} avec un couplage t qui retourne (*flippe*) deux dimères parallèles sur une plaquette.
- *Terme potentiel* : il s'agit de la partie *diagonale* de H_{QDM} avec un couplage V qui compte le nombre de plaquettes retournables (*flippables*).

Le Hamiltonien a deux limites simples. Pour $V/t \rightarrow -\infty$, le système favorise énergétiquement les plaquettes avec des dimères parallèles. Par conséquent, l'état fondamental est donné par l'une des quatre configurations de dimères montrées dans la Fig.8.5, appelée *ordre colonnaire*. L'ordre colonnaire brise spontanément la symétrie de rotation $\pi/2$ et la symétrie de translation selon un pas du réseau le long de la direction des dimères.

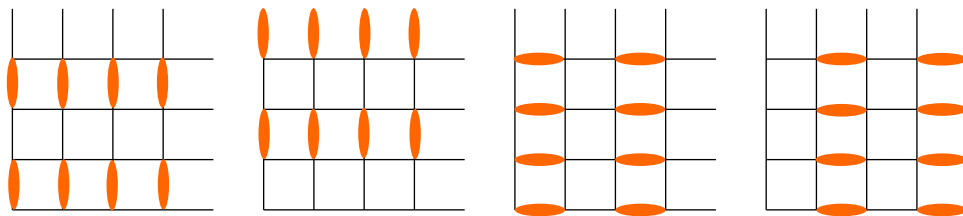


Figure 8.5: 4 configurations colonnaire dégénérées

Pour $V/t \rightarrow \infty$, le système favorise les plaquettes sans dimères parallèles. Ceci est appelé ordre alterné (*staggered*). L'état fondamental de l'ordre alterné a une énergie nulle et, contrairement à l'ordre colonnaire, est extensivement dégénéré.

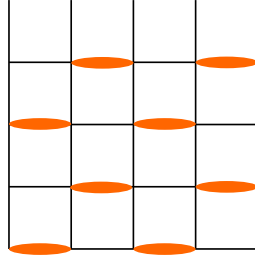


Figure 8.6: Exemple d'une configuration alternée sans dimères parallèles

Les ordres cristallins ci-dessus s'étendent jusqu'à un certain V/t fini dans le diagramme de phase de l'état fondamental de H_{QDM} , paramétré par le rapport V/t . Notre objectif dans cette section est de comprendre comment les phases cristallines ci-dessus fondent sous l'effet des fluctuations thermiques. Nous nous attendons à ce qu'elles survivent jusqu'à une température finie car elles ont des excitations possédant un gap en énergie - la plus petite excitation hors de l'ordre colonnaire est un simple "flip" de plaquette qui coûte une énergie $2V$, tandis que les excitations hors de la phase alternée impliquent le basculement de dimères le long d'une boucle qui s'enroule dans l'une des directions toroïdales et cette excitation coûte une énergie LV .

Les ordres cristallins ci-dessus sont aussi réalisés dans un modèle classique de mécanique statistique appelé modèle classique de dimères en interaction (CIDM), qui a été largement étudié [47, 48, 49, 50, 31]. Le modèle classique capture également les transitions de phase hors des phases cristallines vers une phase désordonnée mais *critique* de dimères. Nous rappelons maintenant brièvement le diagramme de phase du modèle classique ici. La fonction de partition pour le CIDM est donnée par

$$Z = \sum_c e^{-\beta E_c} \quad (8.5)$$

$$E_c = V(N(\text{⬜}) + N(\text{⬜}))$$

où $N(\text{⬜}) + N(\text{⬜})$ compte le nombre total de plaquettes parallèles dans un pavage de dimères c et la sommation est effectuée sur tous ces pavages de dimères. Le signe de V détermine les différents états ordonnés. Si $V < 0$, il est favorable sur le plan énergétique d'avoir des dimères parallèles sur une plaquette, donc à basse température cela conduira à un ordre **colonnaire** (voir Fig. 8.5). Cet état ordonné est dégénéré quatre fois et brise spontanément les symétries de translation et de rotation de $\pi/2$. Si $V > 0$, les plaquettes avec dimères parallèles sont coûteuses en énergie, ce qui à basse température conduit à un ordre de type **alterné** (voir Fig. 8.6), où il n'y a pas de dimères parallèles sur une plaquette.

Dans la limite sans interaction $T = \infty$ ($\beta = 0$), la fonction de partition ci-dessus Eq. 8.5 est la somme non pondérée de tous les pavages de dimères sur le réseau carré, situation qui est exactement soluble [51, 52]. Dans ce cas, il a été montré que les dimères

sont **critiques**, ce qui signifie que les corrélations dimère-dimère décroissent de manière algébrique avec la distance. Plus précisément pour le réseau carré, il peut être démontré exactement que le terme dominant dans la fonction de corrélation décroît comme $1/r^2$. Ceci est en contraste avec les modèles de spin où à $T = \infty$ on retrouve toujours un état paramagnétique, c'est-à-dire entièrement non corrélé.

À haute température, il y a une phase critique où le terme dominant de la fonction de corrélation dimère-dimère décroît de manière algébrique avec la distance comme $1/r^\alpha$ et cet exposant α varie avec la température. Nous savons d'après les résultats exacts que $\alpha(T = \infty) = 2$. Pour les interactions *attractives* ($V < 0$) fixées à $V = -1$ sans perte de généralité, il y a une transition de phase de Kosterlitz Thouless vers les états colonnaires quatre fois dégénérés à $T \sim 0.65$. Cette transition de phase peut être bien comprise par une théorie des champs de *hauteurs* donnée par une action de type Sine-Gordon

$$S = \int d^2r [\pi g (\nabla h(r))^2 + \sum_{p=4,8,\dots} V_p \cos(2\pi p h(r))]. \quad (8.6)$$

Sans entrer dans plus de détails sur l'action ci-dessus, le paramètre important ici est g , la constante du gaz de Coulomb. g est lié à l'exposant de la loi de puissance α des corrélations de dimères comme $g = 1/\alpha$. Dans l'action ci-dessus, le terme cosinus est responsable de la sélection des quatre ordres colonnaires et signalera la transition vers la phase colonnaire lorsqu'il deviendra pertinent (au sens du groupe de renormalisation). Il peut être démontré par une analyse de groupe de renormalisation de l'équation (8.6) que le terme cosinus devient pertinent lorsque $g \geq 4$, où il y a une transition de phase de Kosterlitz-Thouless de la phase critique de dimères vers l'un des quatre ordres colonnaires dégénérés. Nous résumons le diagramme de phase du CIDM pour les interactions attractives dans la Fig.8.7. Pour des interactions *répulsives* ($V > 0$), il y a une transition de phase continue vers un ordre alterné [31]. Cela n'a été démontré que par des méthodes numériques et jusqu'à présent, il n'existe pas de description théorique de cette transition de phase.

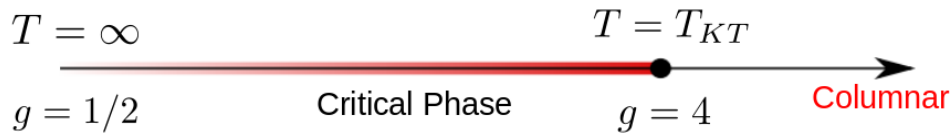


Figure 8.7: Diagramme de phase du CIDM pour des interactions attractives $V < 0$. Ici, $g = 1/\alpha$ est appelée la constante du gaz de Coulomb. Le diagramme de phase montre les valeurs limites de g à $T = \infty$ et à $T_{KT} \sim 0.65$ où il y a une transition de phase de Kosterlitz-Thouless de la phase critique vers une phase colonnaire.

Nous présentons dans la Fig. 8.8 le diagramme de phase à température finie de H_{QDM} obtenu grâce à des simulations de Monte Carlo quantique. Le diagramme de phase est présenté dans un plan 2D avec l'axe des ordonnées représentant la température T/t et

l'axe des abscisses paramétré par V/t (nous fixons $t = 1$). De cette façon, le diagramme de phase classique ci-dessus peut être lu le long de l'axe des ordonnées de notre diagramme de phase quantique dans la limite $V/t \rightarrow \infty$. Dans la phase haute température du diagramme de phase du modèle quantique, la constante du gaz de Coulomb varie maintenant avec la force d'interaction V ainsi qu'avec la température T , $g(T/t, V/t)$. Notre algorithme QMC nous permet de sonder directement g , que nous utilisons pour caractériser la phase critique à haute température. En calculant g , nous montrons également que les transitions de phase hors de la phase colonnaire, au moins jusqu'à $V/t = -0.5$ (une limitation de la simulation), sont de type Kosterlitz-Thouless et peuvent être comprises par la même théorie classique des champs Sine-Gordon donnée par l'Éq.(8.6). Nous estimons également les températures de transition en mesurant les paramètres d'ordre associés. Le diagramme de phase montre également des transitions hors de la phase alternée pour $V/t > 1$. Bien que nous ne connaissions pas encore de théorie pour expliquer cette transition de phase, nous argumentons par une comparaison numérique que la transition de phase dans le cas quantique est dans la même classe d'universalité que le CIDM (qui a été argumenté comme étant continue). Nous observons une variation non monotone de g avec la température dans une plage étroite de V/t près du point Rokhsar Kivelson $V/t = 1$.

8.3 Modèle classique de boucles en interactions sur le réseau carré

Dans cette section, nous présentons le diagramme de phase d'un modèle de mécanique statistique classique de boucles compactes (*fully packed*) sur un réseau carré avec des interactions attractives entre segments de boucles parallèles.

Commençons par définir l'espace de configuration pour le modèle. Similairement au modèle de dimères que nous avons examiné dans la section précédente, nous considérons à nouveau un espace de configuration contraint qui se compose de **boucles compactes sans croisement** sur le réseau carré avec des conditions aux limites périodiques. Comme le montre la Fig.8.9, si nous attribuons une flèche sortante à chaque segment de boucle connectant le sous-réseau A à B et une flèche entrante à chaque liaison vide connectant le sous-réseau A à B (ou vice-versa), les configurations se mappent exactement sur le modèle à six vertex qui est exactement soluble [15, 95, 14, 96, 97, 98].

Les modèles de boucles ou de vertex associent souvent une fugacité à chaque boucle fermée ou à chaque type de vertex respectivement, pour définir la fonction de partition correspondante [80]. Nous nous intéressons ici à un modèle de boucles en interaction

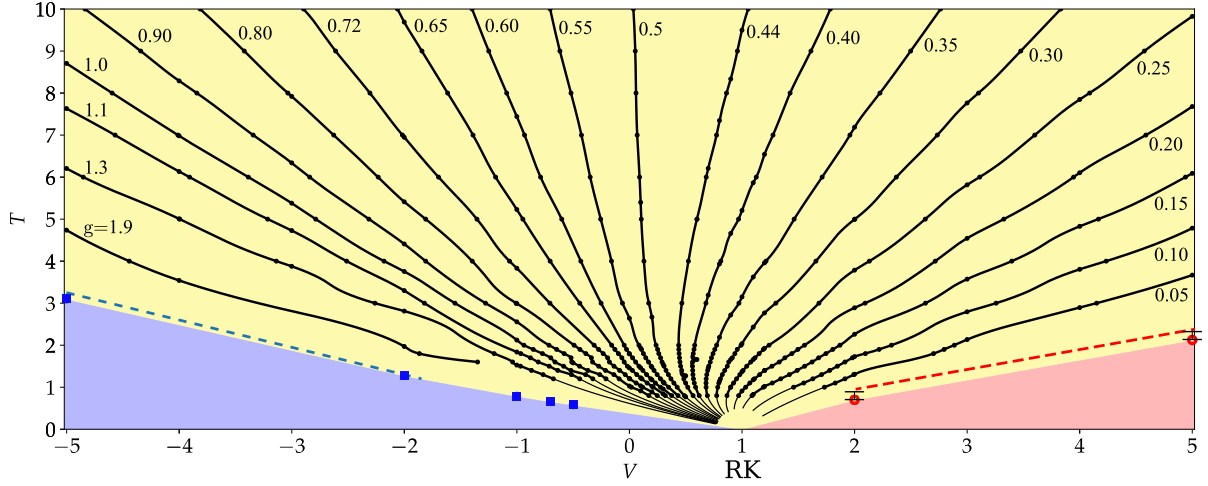


Figure 8.8: Diagramme de phase à température finie du modèle de dimères quantiques sur le réseau carré, dans le plan $(V/t, T/t)$ ($t = 1$ est choisi ici). Les nuances jaunes, bleues et rouges indiquent la phase critique (désordonnée), la phase colonnaire et la phase alternée respectivement. Les lignes noires continues montrent des lignes g constantes. Les lignes solides minces sont des extrapolations vers le point RK $V/t = 1$; elles couvrent des régions inaccessibles aux simulations QMC. Pour cartographier l'ensemble de la phase à haute température, nous avons utilisé des simulations pour des systèmes de taille linéaire $L = 24$ (nous avons vérifié sur des points sélectionnés que l'augmentation de la taille du système jusqu'à $L = 64$ ne changeait pas significativement le diagramme de phase). Les symboles bleus (carré) et rouges (cercle vide) représentent les transitions de phase à température finie vers une phase colonnaire et une phase alternée. Celles-ci sont déterminées en utilisant respectivement les cumulants de Binder des paramètres d'ordre associés aux phases respectives. Les lignes en pointillés représentent le comportement asymptotique classique obtenu pour le CIDM où $T_c = 0.65|V|$ (pour $V < 0$, CIDM attractif [48]) et $T_c = 0.475V$ (pour $V > 0$, CIDM répulsif [31]). La transition vers l'ordre colonnaire (respectivement alterné) est attendue à $g_c = 4$ (respectivement $g = 0$).

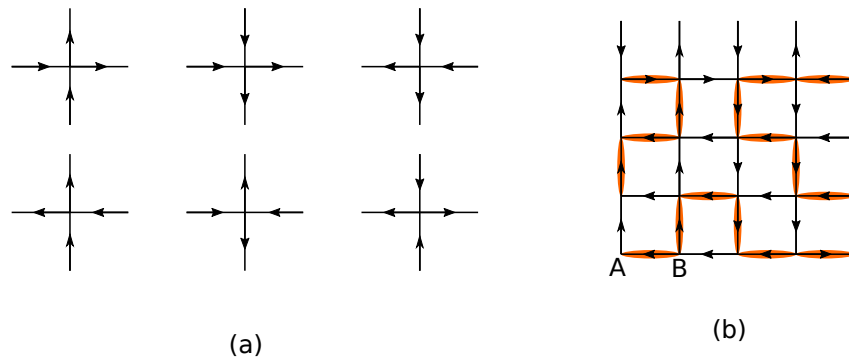


Figure 8.9: (a) montre les six configurations possibles à chaque site du réseau carré pour le modèle à six vertex - deux flèches pointant vers l'intérieur et deux pointant vers l'extérieur. Dans la limite sans interaction, ce mapping est exact avec toutes les six configurations ayant des fugacités égales (point dit de la glace). (b) montre le mapping entre les segments de boucle compacts et les configurations à six vertex.

où nous associons un coût énergétique V aux plaquettes avec des segments de boucles

parallèles. Nous définissons la fonction de partition suivante

$$Z = \sum_c e^{-\beta E_c} \quad (8.7)$$

$$E_c = V(N(\text{□}) + N(\text{□}))$$

où la sommation porte sur toutes les configurations de boucles compactes c et nous attribuons une énergie E_c qui dépend du nombre total de plaquettes avec des segments de boucles parallèles, ici $N(\text{□})$ et $N(\text{□})$ représentent le nombre de plaquettes telles plaquettes. Il n'y a aucune énergie associée aux plaquettes avec plus de deux segments de boucle. Nous nous concentrons sur le cas de $V = -1$ qui correspond à des interactions attractives entre les segments de boucles.

Similairement au cas des dimères [47, 48], nous nous attendons à des états ordonnés à basse température selon le signe de V . Pour $V < 0$, les configurations qui minimisent l'énergie ($E_0 = -L^2$) sont des états ordonnés nématiques, Fig.8.10 qui brisent la symétrie de rotation $\pi/2$. Pour $V > 0$, les configurations d'énergie minimale ($E_0 = 0$) sont celles sans plaquettes parallèles qui forment les états ordonnés alternés, Fig.8.11. Dans la limite sans interaction, les configurations de boucles se mappent sur le modèle à six vertex au point de la glace avec des fugacités égales pour tous les sommets, qui est **critique** avec des corrélations en loi de puissance.

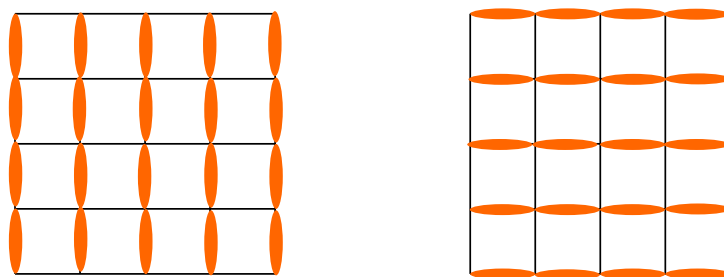


Figure 8.10: Deux états fondamentaux nématiques dégénérés qui brisent la symétrie de rotation par $\pi/2$.

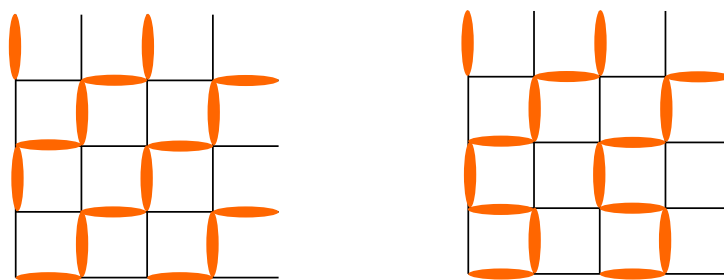


Figure 8.11: Deux exemples de configurations alternées de boucles emballées sur un réseau carré 4x4.

En utilisant des simulations classiques Monte Carlo, nous montrons que pour des interactions *attractives*, le modèle présente une transition de phase de Kosterlitz-Thouless à une température finie, passant d'une phase critique de boucles à haute température à une phase ordonnée nématique de boucles à basse température. Nous montrons également que la transition de phase est à nouveau capturée par une théorie des champs de hauteur donnée par une action de type Sine-Gordon.

$$S = \int d^2r [\pi g (\nabla h(\mathbf{r}))^2 + \mathcal{V} \cos(4\pi \mathbf{h}(\mathbf{r}))] \quad (8.8)$$

où g est à nouveau la constante du gaz de Coulomb.

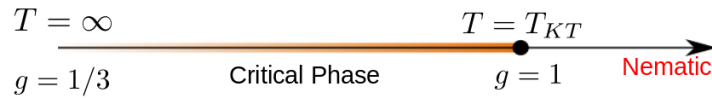


Figure 8.12: Diagramme de phase du modèle de boucle en interaction sur le réseau carré. $T_{KT} = 1.425(1)$ est estimé par des simulations Monte Carlo.

8.4 Régime non-ergodique dans une chaîne de spins désordonnée avec symétrie $SU(3)$

L'existence d'une phase localisée à plusieurs corps stable (MBL) avec une certaine symétrie globale est une question intéressante [158]. Nous avons déjà de nombreuses preuves numériques de phases MBL avec une symétrie abélienne, du moins en 1D. Si nous considérons une phase MBL comme caractérisée par des intégrales de mouvement locales (LIOM), il a été montré que certains ordres topologiques protégés par symétrie et des symétries non abéliennes sont incompatibles avec MBL. L'argument clé avancé est que, en raison de l'existence de dégénérescences exactes dans le spectre à plusieurs corps, les états propres localisés à des énergies finies seraient instables aux interactions : en termes simples, les dégénérescences offrent trop de canaux de thermalisation pour la création de résonances. Par conséquent, le système doit soit thermaliser (comme nous le verrons plus tard pour les symétries continues non abéliennes comme $SU(N)$) soit briser spontanément la symétrie non abélienne en un sous-groupe abélien, ce qui a été démontré pour des chaînes de spin avec des symétries non abéliennes avec des représentations irréductibles de dimension finie [160, 159].

On peut donc exclure une phase MBL complète avec des symétries non abéliennes. Cependant, la possibilité d'une phase partiellement localisée reste. Il pourrait s'agir d'une phase

caractérisée par une croissance logarithmique de l'entropie d'intrication de ses états propres, qui n'est pas entièrement conforme à la loi des aires (pour une phase MBL) mais reste *sous-thermale*. Des exemples de phases avec une telle croissance sont les verres quantiques critiques [161, 162].

Dans cette section, nous rappelons brièvement les résultats importants d'un travail récent sur une chaîne de spin Heisenberg avec symétrie $SU(2)$ en présence de désordre de liens [127]. L'objectif principal de cette étude était d'investiguer si un tel système pourrait héberger une phase non thermique/ergodique et, dans l'affirmative, si une telle phase est stable dans la limite thermodynamique. Ces auteurs se concentrent sur un Hamiltonien très simple

$$H = \sum_{i=1}^L J_i \mathbf{S}_i \mathbf{S}_{i+1} \quad (8.9)$$

où les couplages J_i sont tirés au hasard à partir d'une distribution de probabilité et \mathbf{S}_i sont les opérateurs de spin habituels de spin-1/2. Les auteurs montrent que, sous une certaine approximation, les états propres de l'équation (8.9) ont une structure hiérarchique en forme d'arbre, ce qui entraîne une croissance logarithmique de l'entropie d'intrication ($S_A \sim \ln(L_A)$). De tels états en forme d'arbre ne sont que des approximations des états propres de l'équation (8.9), car ils sont construits à l'aide d'une procédure de renormalisation dans l'espace réel (RSRG), appelé *Strong Disorder Renormalization Group* (SDRG) [163, 164]. Il est donc impératif de vérifier si de tels états propres en forme d'arbre sont de bonnes approximations des vrais états propres de l'équation (8.9). Les auteurs de [127] effectuent cette analyse en comparant les résultats SDRG à des résultats de diagonalisation exacte.

Diagonalisation exacte sur des tailles de système plus petites: Les auteurs effectuent une diagonalisation jusqu'à des tailles de système de $L = 26$. En examinant les sondes MBL standard comme le rapport de participation, les statistiques de niveaux, le test de l'ETH et l'entropie d'intrication, ils extraient une échelle de longueur $L^*(\alpha)$ ($1/\alpha$ quantifie la force du désordre). Pour des tailles de système en dessous de cette échelle de longueur, les états propres en forme d'arbre sont en fait de bonnes approximations de l'équation (8.9), tandis que pour des tailles de système supérieures à $L^*(\alpha)$, les états propres en forme d'arbre deviennent instables. Cette échelle de longueur augmente avec la force du désordre. Pour un désordre faible, même des chaînes relativement petites se thermalisent. Cependant, pour des forces de désordre élevées, les résultats indiquent que les états propres en forme d'arbre sont stables, jusqu'à la plus grande taille de système accessible par diagonalisation.

Limite thermodynamique: La question se pose maintenant de savoir si, pour des forces de désordre élevées, l'image des états propres en arbre reste stable dans la limite thermodynamique. Les auteurs étudient cela en identifiant dans le RSRG des processus de *résonance* qui pourraient entraîner une thermalisation. Ils parviennent à extraire à

nouveau une échelle de longueur $L^{SDRG}(\alpha)$ au-delà de laquelle les processus de résonance prolifèrent et conduisent à la thermalisation. Ces échelles de longueur peuvent être assez grandes pour des forces de désordre élevées, par exemple $L^{SDRG}(0.3) \approx 300$. Cela montre que même pour des forces de désordre élevées, la chaîne de spin-1/2 de Heisenberg finirait par se thermaliser dans la limite thermodynamique. Cela contraste avec une phase MBL conventionnelle qui est censée être stable dans la limite thermodynamique pour des forces de désordre élevées.

En conclusion, même si le Hamiltonien dans l'équation (8.9) se thermalise dans la limite thermodynamique, les échelles de longueur pour cela sont très grandes pour des désordres forts. Par conséquent, pour toutes fins pratiques et expérimentalement réalisables, l'équation (8.9) montre une région sous-thermale non ergodique pour une large gamme de forces de désordre et de tailles de système. Cette région non ergodique montre cependant une croissance logarithmique de l'entropie l'intrication avec des états propres avec une structure de réseau tensoriel en arbre, ce qui diffère considérablement d'une phase MBL standard. Dans cette section, nous présentons les résultats de la diagonalisation exacte pour une chaîne de spins désordonnée avec symétrie $SU(3)$. Sans utiliser de symétries, les matrices des chaînes de spins de taille L auraient une taille 3^L . Cependant, nous exploitons entièrement la symétrie $SU(3)$, suivant la construction décrite dans [169] et le Chapitre 6 de cette thèse. Cela nous permet d'atteindre des tailles de système allant jusqu'à $L = 21$ au lieu d'au mieux $L = 15$ avec des calculs dans la base standard $U(1)$ (S^z).

Nous commençons par définir le modèle et fournir quelques détails techniques sur les tailles de système et les formes de tableau considérées. Nous analysons ensuite les différents indicateurs de thermalisation qui incluent les statistiques spectrales, la distribution d'une observable locale et la variation de l'entropie d'intrication. En chemin, nous comparons avec les indicateurs similaires étudiés précédemment pour le cas $SU(2)$ [127]. Le modèle que nous étudions est donné par le Hamiltonien suivant avec une symétrie $SU(3)$ et des couplages aléatoires sur une chaîne 1D de longueur L .

$$H_{SU(3)} = \sum_{i=1}^L J_i P_{i,i+1} \quad (8.10)$$

Sur chaque site de la chaîne, l'espace de Hilbert local est de dimension 3 avec une base locale $|c_i\rangle$, où $c_i = 1, 2, 3$ dénote les trois "couleurs" possibles d'une particule sur chaque site i . L'opérateur $P_{i,i+1}$ permute les couleurs entre les sites i et $i+1$: $P_{i,i+1}|\dots c_i c'_{i+1} \dots\rangle = |\dots c'_i c_{i+1} \dots\rangle$.

La valeur absolue des constantes de couplage J_i est une variable aléatoire tirée de la distribution de probabilité

$$P(|J|) = \frac{\alpha \Theta(1 - |J|)}{|J|^{1-\alpha}} \quad (8.11)$$

où α dénote l'inverse de la force du désordre (le système est plus désordonné lorsque $\alpha \rightarrow 0$). De plus, le signe de J_i est pris comme positif/négatif avec une probabilité égale, sans perte de généralité.

Nous présentons ci-dessous l'un des indicateurs importants de non-ergodicité, qui est la variation de l'entropie d'intrication dans l'Éq.(8.10) pour une chaîne de taille $L = 21$, en fonction de la taille du bloc d'intrication. Considérons une bipartition de la chaîne en deux parties A et B constituées respectivement par les L_A premiers sites $A = \{i = 1 \dots L_A\}$ et les L_B restants $B = \{i = L_A \dots L\}$ avec $L_A + L_B = L$. En définissant la matrice de densité réduite $\rho_A = \text{Tr}_B |n\rangle\langle n|$ d'un état propre $|n\rangle$ pour une telle bipartition, l'entropie d'intrication de cet état propre est donnée par :

$$S(|n\rangle) = -\text{Tr}_A \rho_A \log(\rho_A).$$

Nous présentons les résultats de l'entropie d'intrication (suivant Ref. [172] pour son calcul dans la base $\text{SU}(3)$) pour les états propres singulets non dégénérés du milieu du spectre du plus grand système que nous avons pu simuler (taille de système $L = 21$) en fonction de la taille du bloc L_A dans Fig. 8.13. Les résultats sont symétriques par rapport à l'inversion de L_A et $L_B = L - L_A$, nous montrons donc uniquement les données jusqu'à $L_A = 10$. Pour un faible désordre (grand $\alpha \geq 1.3$), l'entropie d'intrication suit une loi de volume très claire (avec S croissant linéairement avec la taille du bloc, voir le panneau supérieur de Fig. 8.13), avec un coefficient correspondant au comportement attendu de Page [133, 171] obtenu en considérant l'entropie d'intrication de vecteurs aléatoires (distribués sur la sphère de Haar), présenté sous forme de ligne solide dans Fig. 8.13. Pour un désordre intermédiaire $\alpha = 0.8, 1.0$, la croissance de l'intrication semble linéaire pour de petits L_A mais les données se courbent lorsque L_A atteint $L/2$, en raison de la limitation de la taille finie. Pour un désordre plus important (en particulier pour $\alpha = 0.3, 0.45$), nous observons une croissance lente de l'intrication, compatible avec une croissance logarithmique, pour les tailles de systèmes que nous pouvons atteindre (voir le panneau inférieur de Fig. 8.13 où des fits à une croissance logarithmique de $S(|n\rangle)$ sont montrés). Cela contraste non seulement avec la loi de volume pour de grands α , mais aussi avec la loi des aires stricte attendue pour les états propres MBL standard. Ce comportement logarithmique "sous-thermal" a été prédit pour l'entropie d'intrication dans le régime intermédiaire et de taille finie des chaînes désordonnées $\text{SU}(2)$ par les calculs RSRG [173, 127], mais n'a pas été observée dans les résultats de diagonalisation exacte de taille finie de Ref. [127].

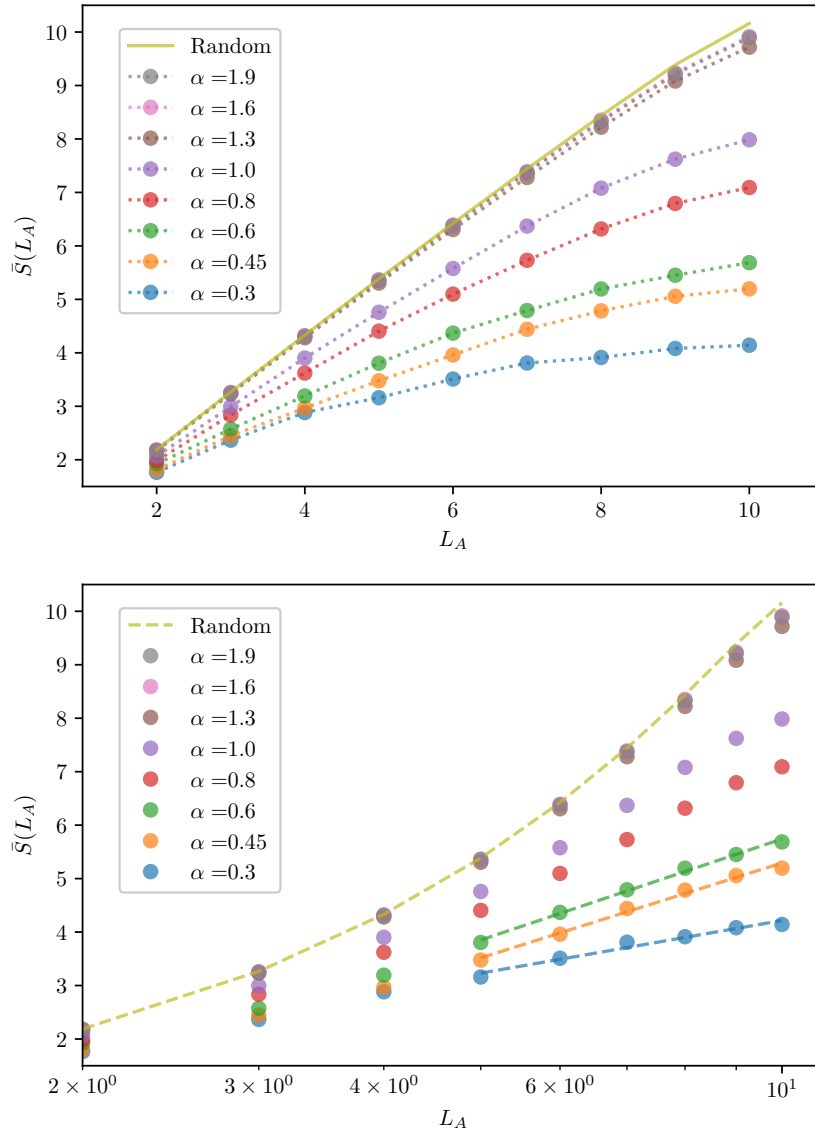


Figure 8.13: Les deux panneaux représentent l'entropie d'intrication S des états propres du milieu du spectre en fonction de la taille du bloc L_A , en fonction du paramètre de désordre α et pour une chaîne de $L = 21$ sites. La ligne solide représente le résultat pour une fonction d'onde sur une taille similaire $L = 21$ avec des coefficients distribués selon une loi gaussienne, correspondant à la loi de volume d'intrication de Page [171]. Panneau supérieur : échelle linéaire pour la taille du bloc L_A , avec des lignes en pointillés représentant des guides visuels. Panneau inférieur : échelle logarithmique pour L_A . Les lignes en pointillés sont des fits à une loi logarithmique $S(L_A) = a + b \log(L_A)$ pour les trois désordres les plus forts et $L_A \in [5, 10]$.

Appendix A

Exact expression for $\langle W^2 \rangle$ at $g = 1$

Here we will present a simple derivation for the exact value of $\langle W^2 \rangle = 1/(4\pi)$ at $g = 1$. We start with the observation that the denominator of Eq. 2.8 is a *Jacobi theta function* $\theta(g)$

$$\theta(g) = \sum_{n \in \mathbb{Z}} e^{-\pi g n^2} \quad (\text{A.1})$$

We can therefore write Eq. 2.8 as

$$\langle W^2(g) \rangle = -\frac{1}{\pi} \frac{d\theta/dg}{\theta(g)} = -\frac{1}{\pi} \frac{d}{dg} \log(\theta(g)) \quad (\text{A.2})$$

We will now make use of the functional equation for the Jacobi theta function

$$\theta(g) = \frac{1}{\sqrt{g}} \theta(1/g) \quad (\text{A.3})$$

Using Eq. A.3 in Eq. A.2

$$\langle W^2(g) \rangle = -\frac{1}{\pi} \frac{d}{dg} \log\left(\frac{1}{\sqrt{g}} \theta(1/g)\right) = -\frac{1}{\pi} \frac{d}{dg} \log(\theta(1/g)) + \frac{1}{2\pi g} \quad (\text{A.4})$$

Expressing the derivative in $1/g$ we have

$$\langle W^2(g) \rangle = \frac{1}{\pi g^2} \frac{d}{d(1/g)} \log(\theta(1/g)) + \frac{1}{2\pi g} \quad (\text{A.5})$$

Replacing g with $1/g$ in Eq. A.2

$$\langle W^2(1/g) \rangle = -\frac{1}{\pi} \frac{d}{dg} \log(\theta(1/g)) \quad (\text{A.6})$$

We can hence write Eq. A.5 as

$$\langle W^2(g) \rangle = -\frac{\langle W^2(1/g) \rangle}{g^2} + \frac{1}{2\pi g} \quad (\text{A.7})$$

Substituting $g = 1$ in above we have

$$\langle W^2(1) \rangle = \frac{1}{4\pi} \quad (\text{A.8})$$

Appendix B

Computation of entanglement entropy in Young tableaux basis

We show with an example how to compute the entanglement entropy (EE) directly in the Young tableau basis. Note that, the method shown only works for rectangular 3-rows tableaux i.e for the singlet sector.

Let us take an example of a $SU(3)$ singlet sector on 6 lattice sites, for which there are 5 valid states of rectangular tableaux with 3 rows and 2 columns. Say the eigenstate for which we want to compute the EE is given by

$$\begin{aligned}
 |\psi\rangle = & c_1 \left| \begin{array}{|c|c|} \hline 1 & 2 \\ \hline 3 & 4 \\ \hline 5 & 6 \\ \hline \end{array} \right\rangle + c_2 \left| \begin{array}{|c|c|} \hline 1 & 3 \\ \hline 2 & 4 \\ \hline 5 & 6 \\ \hline \end{array} \right\rangle + c_3 \left| \begin{array}{|c|c|} \hline 1 & 2 \\ \hline 3 & 5 \\ \hline 4 & 6 \\ \hline \end{array} \right\rangle + c_4 \left| \begin{array}{|c|c|} \hline 1 & 3 \\ \hline 2 & 5 \\ \hline 4 & 6 \\ \hline \end{array} \right\rangle \\
 & + c_5 \left| \begin{array}{|c|c|} \hline 1 & 4 \\ \hline 2 & 5 \\ \hline 3 & 6 \\ \hline \end{array} \right\rangle
 \end{aligned}
 \tag{B.1}$$

Let us say for example we that want to compute the EE for a subsystem A of two sites ($L_A = 2$) and the rest of the subsystem B of the remaining four sites ($L_B = L - L_A = 4$). The next step involves reshaping the coefficient vector, $\{c_1, c_2, c_3, c_4, c_5\}$ in a matrix where the rows label the indices for subsystem A and the columns label the indices for subsystem B.

$$\Psi_{2,4} = \begin{array}{c} \boxed{1} \ \boxed{2} \\ \boxed{1} \\ \boxed{2} \end{array} \left(\begin{array}{ccccc} \begin{array}{|c|c|} \hline 3 & 4 \\ \hline 5 & 6 \\ \hline \end{array} & \begin{array}{|c|c|} \hline 3 & 5 \\ \hline 4 & 6 \\ \hline \end{array} & \begin{array}{|c|} \hline 3 \\ \hline 4 \\ \hline 5 \\ \hline 6 \\ \hline \end{array} & \begin{array}{|c|} \hline 3 \\ \hline 5 \\ \hline 6 \\ \hline \end{array} & \begin{array}{|c|} \hline 4 \\ \hline 5 \\ \hline 6 \\ \hline \end{array} \\ c_1 & c_3 & 0 & 0 & 0 \\ 0 & 0 & c_2 & c_4 & c_5 \end{array} \right)$$

Another example for a half-chain EE i.e subsystem A of three sites and subsystem B of three sites gives

$$\Psi_{3,3} = \begin{array}{c} \begin{array}{|c|c|} \hline 1 & 2 \\ \hline 3 & \end{array} \\ \begin{array}{|c|c|} \hline 1 & 3 \\ \hline 2 & \end{array} \\ \begin{array}{|c|} \hline 1 \\ \hline 2 \\ \hline 3 \\ \hline \end{array} \end{array} \left(\begin{array}{ccc} \begin{array}{|c|c|} \hline 4 \\ \hline 5 \\ \hline 6 \\ \hline \end{array} & \begin{array}{|c|c|} \hline 5 \\ \hline 6 \\ \hline \end{array} & \begin{array}{|c|} \hline 4 \\ \hline 5 \\ \hline 6 \\ \hline \end{array} \\ c_1 & c_3 & 0 \\ c_2 & c_4 & 0 \\ 0 & 0 & c_5 \end{array} \right)$$

Once a particular shape of tableau is chosen for subsystem A, the possible tableau shape for subsystem B is constrained by the fact that the full tableau must be 3-rows rectangular (singlet). What we have just shown is a reshape operation on $|\psi\rangle$ which is now given by

$$|\psi\rangle = \sum_{i_A, i_B} c_{i_A i_B} |i_A i_B\rangle \quad (\text{B.2})$$

where the indices i_A and i_B belong to subsystems L_A and L_B respectively. If the density matrix of the pure state $|\psi\rangle$ is given by

$$\rho = |\psi\rangle\langle\psi| = \sum_{i_A, i_B, i'_A, i'_B} c_{i_A i_B} c_{i'_A i'_B}^* |i_A i_B\rangle\langle i'_A i'_B| \quad (\text{B.3})$$

the reduced density matrix for subsystem A is

$$\rho_A = \text{Tr}_B \rho = \sum_{i_A, i'_A} \left(\sum_{i_B} c_{i_A i_B} c_{i'_A i_B}^* \right) |i_A i_B\rangle \langle i'_A i_B| = \Psi \Psi^\dagger \quad (\text{B.4})$$

Performing an SVD for Ψ gives

$$\rho_A = U S V^\dagger V S U^\dagger = U S^2 U^\dagger \quad (\text{B.5})$$

The entanglement entropy for subsystem A is then given by

$$S_A = -\text{Tr}(\rho_A \log \rho_A) = -\sum_i s_i^2 \log s_i^2 \quad (\text{B.6})$$

Where s_i are the singular values of Ψ .

References

- [1] R. H. Fowler and G. S. Rushbrooke. “An attempt to extend the statistical theory of perfect solutions”. In: *Trans. Faraday Soc.* 33 (0 1937), pp. 1272–1294. DOI: [10.1039/TF9373301272](https://doi.org/10.1039/TF9373301272).
- [2] P. W. Kasteleyn. “Dimer Statistics and Phase Transitions”. In: *Journal of Mathematical Physics* 4.2 (Feb. 1963), pp. 287–293. ISSN: 0022-2488. DOI: [10.1063/1.1703953](https://doi.org/10.1063/1.1703953). eprint: https://pubs.aip.org/aip/jmp/article-pdf/4/2/287/19156929/287_1_online.pdf.
- [3] H. N. V. Temperley and Michael E. Fisher. “Dimer problem in statistical mechanics— an exact result”. In: *Philosophical Magazine* 6 (1961), pp. 1061–1063.
- [4] Henk W. J. Blöte and M. Peter Nightingale. “Antiferromagnetic triangular Ising model: Critical behavior of the ground state”. In: *Phys. Rev. B* 47 (22 June 1993), pp. 15046–15059. DOI: [10.1103/PhysRevB.47.15046](https://doi.org/10.1103/PhysRevB.47.15046).
- [5] T. Fennell et al. “Magnetic Coulomb Phase in the Spin Ice”. In: *Science* 326.5951 (2009), pp. 415–417. DOI: [10.1126/science.1177582](https://doi.org/10.1126/science.1177582). eprint: <https://www.science.org/doi/pdf/10.1126/science.1177582>.
- [6] David A. Huse et al. “Coulomb and Liquid Dimer Models in Three Dimensions”. In: *Phys. Rev. Lett.* 91 (16 Oct. 2003), p. 167004. DOI: [10.1103/PhysRevLett.91.167004](https://doi.org/10.1103/PhysRevLett.91.167004).
- [7] P.W. Anderson. “Resonating valence bonds: A new kind of insulator?” In: *Materials Research Bulletin* 8.2 (1973), pp. 153–160. ISSN: 0025-5408. DOI: [https://doi.org/10.1016/0025-5408\(73\)90167-0](https://doi.org/10.1016/0025-5408(73)90167-0).
- [8] Daniel S. Rokhsar and Steven A. Kivelson. “Superconductivity and the Quantum Hard-Core Dimer Gas”. In: *Phys. Rev. Lett.* 61 (20 Nov. 1988), pp. 2376–2379. DOI: [10.1103/PhysRevLett.61.2376](https://doi.org/10.1103/PhysRevLett.61.2376).
- [9] Mehran Kardar. *Statistical Physics of Fields*. Cambridge University Press, 2007.

- [10] Paul Fendley. “Loop models and their critical points”. In: *Journal of Physics A: Mathematical and General* 39.50 (Nov. 2006), p. 15445. DOI: [10.1088/0305-4470/39/50/011](https://doi.org/10.1088/0305-4470/39/50/011).
- [11] C. Domb and J. L. Lebowitz, eds. *PHASE TRANSITIONS AND CRITICAL PHENOMENA. VOL. 11*. 1987.
- [12] Bernard Nienhuis. “Coulomb gas formulations of two-dimensional phase transitions”. In: *Phase transitions and critical phenomena Vol. 11*. Ed. by C. Domb and J.L. Lebowitz. Academic Press, 1987. Chap. 1, pp. 1–53.
- [13] John Cardy. “SLE for theoretical physicists”. In: *Annals of Physics* 318.1 (2005). Special Issue, pp. 81–118. ISSN: 0003-4916. DOI: <https://doi.org/10.1016/j.aop.2005.04.001>.
- [14] Elliott H. Lieb. “Exact Solution of the F Model of An Antiferroelectric”. In: *Phys. Rev. Lett.* 18 (24 June 1967), pp. 1046–1048. DOI: [10.1103/PhysRevLett.18.1046](https://doi.org/10.1103/PhysRevLett.18.1046).
- [15] E. H. Lieb and F. Y. Wu. “Two-dimensional Ferroelectric Models”. In: *Phase transitions and critical phenomena: Exact Results*. Ed. by C. Domb and M. S. Green. Vol. 1. Academic, London, 1972. Chap. 8, pp. 331–490.
- [16] R. J. Baxter. “Exactly Solved Models in Statistical Mechanics”. In: *Integrable Systems in Statistical Mechanics*, pp. 5–63. DOI: [10.1142/9789814415255_0002](https://doi.org/10.1142/9789814415255_0002). eprint: https://www.worldscientific.com/doi/pdf/10.1142/9789814415255_0002.
- [17] Pascal Scholl et al. “Quantum simulation of 2D antiferromagnets with hundreds of Rydberg atoms”. In: *Nature* 595.7866 (July 2021), pp. 233–238. ISSN: 1476-4687. DOI: [10.1038/s41586-021-03585-1](https://doi.org/10.1038/s41586-021-03585-1).
- [18] Richard P. Feynman. “Simulating physics with computers”. In: *International Journal of Theoretical Physics* 21.6 (June 1982), pp. 467–488. ISSN: 1572-9575. DOI: [10.1007/BF02650179](https://doi.org/10.1007/BF02650179).
- [19] E. Urban et al. “Observation of Rydberg blockade between two atoms”. In: *Nature Physics* 5.2 (Feb. 2009), pp. 110–114. ISSN: 1745-2481. DOI: [10.1038/nphys1178](https://doi.org/10.1038/nphys1178).
- [20] Rhine Samajdar et al. “Quantum phases of Rydberg atoms on a kagome lattice”. In: *Proceedings of the National Academy of Sciences* 118.4 (2021), e2015785118. DOI: [10.1073/pnas.2015785118](https://doi.org/10.1073/pnas.2015785118).
- [21] G. Semeghini et al. “Probing topological spin liquids on a programmable quantum simulator”. In: *Science* 374.6572 (Dec. 2021), pp. 1242–1247. DOI: [10.1126/science.abi8794](https://doi.org/10.1126/science.abi8794).

- [22] Zhongda Zeng, Giuliano Giudici, and Hannes Pichler. *Quantum dimer models with Rydberg gadgets*. 2024. arXiv: [2402.10651](https://arxiv.org/abs/2402.10651) [[quant-ph](#)].
- [23] Giacomo Giudice et al. “Trimer states with \mathbb{Z}_3 topological order in Rydberg atom arrays”. In: *Phys. Rev. B* 106 (19 Nov. 2022), p. 195155. DOI: [10.1103/PhysRevB.106.195155](https://doi.org/10.1103/PhysRevB.106.195155).
- [24] Hannes Bernien et al. “Probing many-body dynamics on a 51-atom quantum simulator”. In: *Nature* 551.7682 (Nov. 2017), pp. 579–584. ISSN: 1476-4687. DOI: [10.1038/nature24622](https://doi.org/10.1038/nature24622).
- [25] Igor Lesanovsky and Hosho Katsura. “Interacting Fibonacci anyons in a Rydberg gas”. In: *Phys. Rev. A* 86 (4 Oct. 2012), p. 041601. DOI: [10.1103/PhysRevA.86.041601](https://doi.org/10.1103/PhysRevA.86.041601).
- [26] C. J. Turner et al. “Quantum scarred eigenstates in a Rydberg atom chain: Entanglement, breakdown of thermalization, and stability to perturbations”. In: *Phys. Rev. B* 98 (15 Oct. 2018), p. 155134. DOI: [10.1103/PhysRevB.98.155134](https://doi.org/10.1103/PhysRevB.98.155134).
- [27] T. Senthil et al. “Deconfined Quantum Critical Points”. In: *Science* 303.5663 (2004), pp. 1490–1494. DOI: [10.1126/science.1091806](https://doi.org/10.1126/science.1091806). eprint: <https://www.science.org/doi/pdf/10.1126/science.1091806>.
- [28] R. Moessner and K. S. Raman. *Quantum dimer models*. 2008. arXiv: [0809.3051](https://arxiv.org/abs/0809.3051) [[cond-mat.str-el](#)].
- [29] R. B. Laughlin. “Nobel Lecture: Fractional quantization”. In: *Rev. Mod. Phys.* 71 (4 July 1999), pp. 863–874. DOI: [10.1103/RevModPhys.71.863](https://doi.org/10.1103/RevModPhys.71.863).
- [30] S.A. Kivelson. “Electron fractionalization”. In: *Synthetic Metals* 125.1 (2001). Celebrating the year 2000 Nobel prize in Chemistry for the discovery and development of conducting polymers, pp. 99–106. ISSN: 0379-6779. DOI: [https://doi.org/10.1016/S0379-6779\(01\)00516-1](https://doi.org/10.1016/S0379-6779(01)00516-1).
- [31] Neil Wilkins and Stephen Powell. “Interacting double dimer model on the square lattice”. In: *Phys. Rev. B* 102 (17 Nov. 2020), p. 174431. DOI: [10.1103/PhysRevB.102.174431](https://doi.org/10.1103/PhysRevB.102.174431).
- [32] A. Ralko, D. Poilblanc, and R. Moessner. “Generic Mixed Columnar-Plaquette Phases in Rokhsar-Kivelson Models”. In: *Phys. Rev. Lett.* 100 (3 Jan. 2008), p. 037201. DOI: [10.1103/PhysRevLett.100.037201](https://doi.org/10.1103/PhysRevLett.100.037201).
- [33] M. Mambrini, S. Capponi, and F. Alet. “Engineering SU(2) invariant spin models to mimic quantum dimer physics on the square lattice”. In: *Phys. Rev. B* 92 (13 Oct. 2015), p. 134413. DOI: [10.1103/PhysRevB.92.134413](https://doi.org/10.1103/PhysRevB.92.134413).

- [34] R. Moessner and S. L. Sondhi. “Resonating Valence Bond Phase in the Triangular Lattice Quantum Dimer Model”. In: *Phys. Rev. Lett.* 86 (9 Feb. 2001), pp. 1881–1884. DOI: [10.1103/PhysRevLett.86.1881](https://doi.org/10.1103/PhysRevLett.86.1881).
- [35] Subir Sachdev. “Spin-Peierls ground states of the quantum dimer model: A finite-size study”. In: *Phys. Rev. B* 40 (7 Sept. 1989), pp. 5204–5207. DOI: [10.1103/PhysRevB.40.5204](https://doi.org/10.1103/PhysRevB.40.5204).
- [36] Olav F. Syljuåsen. “Plaquette phase of the square-lattice quantum dimer model: Quantum Monte Carlo calculations”. In: *Phys. Rev. B* 73 (24 June 2006), p. 245105. DOI: [10.1103/PhysRevB.73.245105](https://doi.org/10.1103/PhysRevB.73.245105).
- [37] D. Banerjee et al. “Finite-volume energy spectrum, fractionalized strings, and low-energy effective field theory for the quantum dimer model on the square lattice”. In: *Phys. Rev. B* 94 (11 Sept. 2016), p. 115120. DOI: [10.1103/PhysRevB.94.115120](https://doi.org/10.1103/PhysRevB.94.115120).
- [38] Zheng Yan et al. “Widely existing mixed phase structure of the quantum dimer model on a square lattice”. In: *Phys. Rev. B* 103 (9 Mar. 2021), p. 094421. DOI: [10.1103/PhysRevB.103.094421](https://doi.org/10.1103/PhysRevB.103.094421).
- [39] Thiago M. Schlittler, Rémy Mosseri, and Thomas Barthel. “Phase diagram of the hexagonal lattice quantum dimer model: Order parameters, ground-state energy, and gaps”. In: *Phys. Rev. B* 96 (19 Nov. 2017), p. 195142. DOI: [10.1103/PhysRevB.96.195142](https://doi.org/10.1103/PhysRevB.96.195142).
- [40] R. Moessner and S. L. Sondhi. “Three-dimensional resonating-valence-bond liquids and their excitations”. In: *Phys. Rev. B* 68 (18 Nov. 2003), p. 184512. DOI: [10.1103/PhysRevB.68.184512](https://doi.org/10.1103/PhysRevB.68.184512).
- [41] Olga Sikora et al. “Quantum Liquid with Deconfined Fractional Excitations in Three Dimensions”. In: *Phys. Rev. Lett.* 103 (24 Dec. 2009), p. 247001. DOI: [10.1103/PhysRevLett.103.247001](https://doi.org/10.1103/PhysRevLett.103.247001).
- [42] Olga Sikora et al. “Extended quantum $U(1)$ -liquid phase in a three-dimensional quantum dimer model”. In: *Phys. Rev. B* 84 (11 Sept. 2011), p. 115129. DOI: [10.1103/PhysRevB.84.115129](https://doi.org/10.1103/PhysRevB.84.115129).
- [43] Doron L. Bergman, Gregory A. Fiete, and Leon Balents. “Ordering in a frustrated pyrochlore antiferromagnet proximate to a spin liquid”. In: *Phys. Rev. B* 73 (13 Apr. 2006), p. 134402. DOI: [10.1103/PhysRevB.73.134402](https://doi.org/10.1103/PhysRevB.73.134402).
- [44] Grégoire Misguich and Frédéric Mila. “Quantum dimer model on the triangular lattice: Semiclassical and variational approaches to vison dispersion and condensation”. In: *Phys. Rev. B* 77 (13 Apr. 2008), p. 134421. DOI: [10.1103/PhysRevB.77.134421](https://doi.org/10.1103/PhysRevB.77.134421).

- [45] G. Misguich, D. Serban, and V. Pasquier. “Quantum Dimer Model on the Kagome Lattice: Solvable Dimer-Liquid and Ising Gauge Theory”. In: *Phys. Rev. Lett.* 89 (13 Sept. 2002), p. 137202. DOI: [10.1103/PhysRevLett.89.137202](https://doi.org/10.1103/PhysRevLett.89.137202).
- [46] G. Misguich, D. Serban, and V. Pasquier. “Quantum dimer model with extensive ground-state entropy on the kagome lattice”. In: *Phys. Rev. B* 67 (21 June 2003), p. 214413. DOI: [10.1103/PhysRevB.67.214413](https://doi.org/10.1103/PhysRevB.67.214413).
- [47] Fabien Alet et al. “Interacting Classical Dimers on the Square Lattice”. In: *Phys. Rev. Lett.* 94 (23 June 2005), p. 235702. DOI: [10.1103/PhysRevLett.94.235702](https://doi.org/10.1103/PhysRevLett.94.235702).
- [48] Fabien Alet et al. “Classical dimers with aligning interactions on the square lattice”. In: *Phys. Rev. E* 74 (4 Oct. 2006), p. 041124. DOI: [10.1103/PhysRevE.74.041124](https://doi.org/10.1103/PhysRevE.74.041124).
- [49] Stefanos Papanikolaou, Erik Luijten, and Eduardo Fradkin. “Quantum criticality, lines of fixed points, and phase separation in doped two-dimensional quantum dimer models”. In: *Phys. Rev. B* 76 (13 Oct. 2007), p. 134514. DOI: [10.1103/PhysRevB.76.134514](https://doi.org/10.1103/PhysRevB.76.134514).
- [50] Fabien Alet. “Dimères classiques en interaction & Autres problèmes en magnétisme quantique”. Habilitation à diriger des recherches. Université Paul Sabatier (Toulouse 3), Feb. 2016.
- [51] Michael E. Fisher. “Statistical Mechanics of Dimers on a Plane Lattice”. In: *Phys. Rev.* 124 (6 Dec. 1961), pp. 1664–1672. DOI: [10.1103/PhysRev.124.1664](https://doi.org/10.1103/PhysRev.124.1664).
- [52] P.W. Kasteleyn. “The statistics of dimers on a lattice: I. The number of dimer arrangements on a quadratic lattice”. In: *Physica* 27.12 (1961), pp. 1209–1225. ISSN: 0031-8914. DOI: [https://doi.org/10.1016/0031-8914\(61\)90063-5](https://doi.org/10.1016/0031-8914(61)90063-5).
- [53] Chen Zeng and Christopher L. Henley. “Zero-temperature phase transitions of an antiferromagnetic Ising model of general spin on a triangular lattice”. In: *Phys. Rev. B* 55 (22 June 1997), pp. 14935–14947. DOI: [10.1103/PhysRevB.55.14935](https://doi.org/10.1103/PhysRevB.55.14935).
- [54] Sidney Coleman. “Quantum sine-Gordon equation as the massive Thirring model”. In: *Phys. Rev. D* 11 (8 Apr. 1975), pp. 2088–2097. DOI: [10.1103/PhysRevD.11.2088](https://doi.org/10.1103/PhysRevD.11.2088).
- [55] Bernard Nienhuis. “Exact Critical Point and Critical Exponents of $O(n)$ Models in Two Dimensions”. In: *Phys. Rev. Lett.* 49 (15 Oct. 1982), pp. 1062–1065. DOI: [10.1103/PhysRevLett.49.1062](https://doi.org/10.1103/PhysRevLett.49.1062).
- [56] Eduardo Fradkin et al. “Bipartite Rokhsar–Kivelson points and Cantor deconfinement”. In: *Phys. Rev. B* 69 (22 June 2004), p. 224415. DOI: [10.1103/PhysRevB.69.224415](https://doi.org/10.1103/PhysRevB.69.224415).

- [57] Nicholas Metropolis et al. “Equation of State Calculations by Fast Computing Machines”. In: *The Journal of Chemical Physics* 21.6 (June 1953), pp. 1087–1092. ISSN: 0021-9606. DOI: [10.1063/1.1699114](https://pubs.aip.org/aip/jcp/article-pdf/21/6/1087/18802390/1087_1_online.pdf). eprint: https://pubs.aip.org/aip/jcp/article-pdf/21/6/1087/18802390/1087_1_online.pdf.
- [58] Werner Krauth. “Statistical Mechanics: Algorithms and Computations”. In: 2006.
- [59] Werner Krauth. “Event-Chain Monte Carlo: Foundations, Applications, and Prospects”. In: *Frontiers in Physics* 9 (2021). ISSN: 2296-424X. DOI: [10.3389/fphy.2021.663457](https://doi.org/10.3389/fphy.2021.663457).
- [60] Etienne P. Bernard, Werner Krauth, and David B. Wilson. “Event-chain Monte Carlo algorithms for hard-sphere systems”. In: *Phys. Rev. E* 80 (5 Nov. 2009), p. 056704. DOI: [10.1103/PhysRevE.80.056704](https://doi.org/10.1103/PhysRevE.80.056704).
- [61] Hidemaro Suwa. “Geometric allocation approach to accelerating directed worm algorithm”. In: *Phys. Rev. E* 103 (1 Jan. 2021), p. 013308. DOI: [10.1103/PhysRevE.103.013308](https://doi.org/10.1103/PhysRevE.103.013308).
- [62] S Todo and H Suwa. “Geometric allocation approaches in Markov chain Monte Carlo”. In: *Journal of Physics: Conference Series* 473.1 (Dec. 2013), p. 012013. DOI: [10.1088/1742-6596/473/1/012013](https://doi.org/10.1088/1742-6596/473/1/012013).
- [63] Fabien Alet and Erik S. Sørensen. “Directed geometrical worm algorithm applied to the quantum rotor model”. In: *Phys. Rev. E* 68 (2 Aug. 2003), p. 026702. DOI: [10.1103/PhysRevE.68.026702](https://doi.org/10.1103/PhysRevE.68.026702).
- [64] Anders W. Sandvik and R. Moessner. “Correlations and confinement in nonplanar two-dimensional dimer models”. In: *Phys. Rev. B* 73 (14 Apr. 2006), p. 144504. DOI: [10.1103/PhysRevB.73.144504](https://doi.org/10.1103/PhysRevB.73.144504).
- [65] Olav F. Syljuåsen and Anders W. Sandvik. “Quantum Monte Carlo with directed loops”. In: *Phys. Rev. E* 66 (4 Oct. 2002), p. 046701. DOI: [10.1103/PhysRevE.66.046701](https://doi.org/10.1103/PhysRevE.66.046701).
- [66] Olav F Syljuåsen and MB Zvonarev. “Directed-loop Monte Carlo simulations of vertex models”. In: *Physical Review E* 70.1 (2004), p. 016118.
- [67] G. T. Barkema and M. E. J. Newman. “Monte Carlo simulation of ice models”. In: *Phys. Rev. E* 57 (1 Jan. 1998), pp. 1155–1166. DOI: [10.1103/PhysRevE.57.1155](https://doi.org/10.1103/PhysRevE.57.1155).
- [68] G. J. Sreejith and Stephen Powell. “Critical behavior in the cubic dimer model at nonzero monomer density”. In: *Phys. Rev. B* 89 (1 Jan. 2014), p. 014404. DOI: [10.1103/PhysRevB.89.014404](https://doi.org/10.1103/PhysRevB.89.014404).
- [69] Lode Pollet et al. “Optimal Monte Carlo updating”. In: *Phys. Rev. E* 70 (5 Nov. 2004), p. 056705. DOI: [10.1103/PhysRevE.70.056705](https://doi.org/10.1103/PhysRevE.70.056705).

- [70] Anders W. Sandvik. “Computational Studies of Quantum Spin Systems”. In: *AIP Conference Proceedings* 1297.1 (Nov. 2010), pp. 135–338. ISSN: 0094-243X. DOI: [10.1063/1.3518900](https://doi.org/10.1063/1.3518900). eprint: https://pubs.aip.org/aip/acp/article-pdf/1297/1/135/11407753/135\1_online.pdf.
- [71] Zheng Yan et al. “Sweeping cluster algorithm for quantum spin systems with strong geometric restrictions”. In: *Phys. Rev. B* 99 (16 Apr. 2019), p. 165135. DOI: [10.1103/PhysRevB.99.165135](https://doi.org/10.1103/PhysRevB.99.165135).
- [72] Martin Hasenbusch. “The Binder cumulant at the Kosterlitz–Thouless transition”. In: *Journal of Statistical Mechanics: Theory and Experiment* 2008.08 (Aug. 2008), P08003. DOI: [10.1088/1742-5468/2008/08/P08003](https://doi.org/10.1088/1742-5468/2008/08/P08003).
- [73] Ling Wang, K. S. D. Beach, and Anders W. Sandvik. “High-precision finite-size scaling analysis of the quantum-critical point of $S = 1/2$ Heisenberg antiferromagnetic bilayers”. In: *Phys. Rev. B* 73 (1 Jan. 2006), p. 014431. DOI: [10.1103/PhysRevB.73.014431](https://doi.org/10.1103/PhysRevB.73.014431).
- [74] Thiago Schlittler et al. “Phase Diagram of an Extended Quantum Dimer Model on the Hexagonal Lattice”. In: *Phys. Rev. Lett.* 115 (21 Nov. 2015), p. 217202. DOI: [10.1103/PhysRevLett.115.217202](https://doi.org/10.1103/PhysRevLett.115.217202).
- [75] Lei Wang et al. “Fidelity Susceptibility Made Simple: A Unified Quantum Monte Carlo Approach”. In: *Phys. Rev. X* 5 (3 July 2015), p. 031007. DOI: [10.1103/PhysRevX.5.031007](https://doi.org/10.1103/PhysRevX.5.031007).
- [76] David Schwandt, Fabien Alet, and Sylvain Capponi. “Quantum Monte Carlo Simulations of Fidelity at Magnetic Quantum Phase Transitions”. In: *Phys. Rev. Lett.* 103 (17 Oct. 2009), p. 170501. DOI: [10.1103/PhysRevLett.103.170501](https://doi.org/10.1103/PhysRevLett.103.170501).
- [77] Fabien Alet and Erik S. Sørensen. “Directed geometrical worm algorithm applied to the quantum rotor model”. In: *Phys. Rev. E* 68 (2 Aug. 2003), p. 026702. DOI: [10.1103/PhysRevE.68.026702](https://doi.org/10.1103/PhysRevE.68.026702).
- [78] Jané Kondev and Christopher L. Henley. “Kac-Moody symmetries of critical ground states”. In: *Nuclear Physics B* 464.3 (1996), pp. 540–575. ISSN: 0550-3213. DOI: [https://doi.org/10.1016/0550-3213\(96\)00064-8](https://doi.org/10.1016/0550-3213(96)00064-8).
- [79] R. Moessner, Oleg Tchernyshyov, and S. L. Sondhi. “Planar Pyrochlore, Quantum Ice and Sliding Ice”. In: *Journal of Statistical Physics* 116.1-4 (Aug. 2004), pp. 755–772. DOI: [10.1023/B:JOSS.0000037247.54022.62](https://doi.org/10.1023/B:JOSS.0000037247.54022.62).
- [80] Bernard Nienhuis. “Loop models”. In: *Exact methods in low-dimensional statistical physics and quantum computing*. Ed. by J. Jacobsen et al. Oxford: Oxford University Press, 2010. Chap. 6, pp. 159–195.

- [81] J. L. Jacobsen, N. Read, and H. Saleur. “Dense Loops, Supersymmetry, and Goldstone Phases in Two Dimensions”. In: *Phys. Rev. Lett.* 90 (9 Mar. 2003), p. 090601. DOI: [10.1103/PhysRevLett.90.090601](https://doi.org/10.1103/PhysRevLett.90.090601).
- [82] Jesper Lykke Jacobsen. “Conformal Field Theory Applied to Loop Models”. In: *Polygons, Polyominoes and Polycubes*. Ed. by Anthony J. Guttmann. Dordrecht: Springer Netherlands, 2009, pp. 347–424. ISBN: 978-1-4020-9927-4. DOI: [10.1007/978-1-4020-9927-4_14](https://doi.org/10.1007/978-1-4020-9927-4_14).
- [83] Adam Nahum et al. “Loop models with crossings”. In: *Phys. Rev. B* 87 (18 May 2013), p. 184204. DOI: [10.1103/PhysRevB.87.184204](https://doi.org/10.1103/PhysRevB.87.184204).
- [84] Claudio Castelnovo et al. “From quantum mechanics to classical statistical physics: Generalized Rokhsar–Kivelson Hamiltonians and the “Stochastic Matrix Form” decomposition”. In: *Annals of Physics* 318.2 (2005), pp. 316–344. ISSN: 0003-4916. DOI: <https://doi.org/10.1016/j.aop.2005.01.006>.
- [85] Shankar Balasubramanian, Victor Galitski, and Ashvin Vishwanath. “Classical vertex model dualities in a family of two-dimensional frustrated quantum anti-ferromagnets”. In: *Phys. Rev. B* 106 (19 Nov. 2022), p. 195127. DOI: [10.1103/PhysRevB.106.195127](https://doi.org/10.1103/PhysRevB.106.195127).
- [86] Louis-Paul Henry and Tommaso Roscilde. “Order-by-Disorder and Quantum Coulomb Phase in Quantum Square Ice”. In: *Phys. Rev. Lett.* 113 (2 July 2014), p. 027204. DOI: [10.1103/PhysRevLett.113.027204](https://doi.org/10.1103/PhysRevLett.113.027204).
- [87] Krishanu Roychowdhury, Subhro Bhattacharjee, and Frank Pollmann. “ \mathbb{Z}_2 topological liquid of hard-core bosons on a kagome lattice at 1/3 filling”. In: *Phys. Rev. B* 92 (7 Aug. 2015), p. 075141. DOI: [10.1103/PhysRevB.92.075141](https://doi.org/10.1103/PhysRevB.92.075141).
- [88] Xiaoxue Ran et al. “Fully packed quantum loop model on the square lattice: Phase diagram and application for Rydberg atoms”. In: *Phys. Rev. B* 107 (12 Mar. 2023), p. 125134. DOI: [10.1103/PhysRevB.107.125134](https://doi.org/10.1103/PhysRevB.107.125134).
- [89] Zheng Yan et al. “Fully packed quantum loop model on the triangular lattice: Hidden vison plaquette phase and cubic phase transitions”. In: (). arXiv: [2205.04472\(2022\)](https://arxiv.org/abs/2205.04472) [[cond-mat.str-el](https://arxiv.org/abs/2205.04472)].
- [90] Zheng Yan et al. “Height-conserving quantum dimer models”. In: *Phys. Rev. B* 106 (4 July 2022), p. L041115. DOI: [10.1103/PhysRevB.106.L041115](https://doi.org/10.1103/PhysRevB.106.L041115).
- [91] Ruben Verresen and Ashvin Vishwanath. “Unifying Kitaev Magnets, Kagomé Dimer Models, and Ruby Rydberg Spin Liquids”. In: *Phys. Rev. X* 12 (4 Dec. 2022), p. 041029. DOI: [10.1103/PhysRevX.12.041029](https://doi.org/10.1103/PhysRevX.12.041029).

- [92] Frank Pollmann et al. “Fermionic quantum dimer and fully-packed loop models on the square lattice”. In: *Phys. Rev. B* 83 (15 Apr. 2011), p. 155117. DOI: [10.1103/PhysRevB.83.155117](https://doi.org/10.1103/PhysRevB.83.155117).
- [93] D Banerjee et al. “The (2 + 1)-d U(1) quantum link model masquerading as deconfined criticality*”. In: *Journal of Statistical Mechanics: Theory and Experiment* 2013.12 (Dec. 2013), P12010. DOI: [10.1088/1742-5468/2013/12/P12010](https://doi.org/10.1088/1742-5468/2013/12/P12010).
- [94] Ruben Verresen, Mikhail D. Lukin, and Ashvin Vishwanath. “Prediction of Toric Code Topological Order from Rydberg Blockade”. In: *Phys. Rev. X* 11 (3 July 2021), p. 031005. DOI: [10.1103/PhysRevX.11.031005](https://doi.org/10.1103/PhysRevX.11.031005).
- [95] Elliott H. Lieb. “Residual Entropy of Square Ice”. In: *Phys. Rev.* 162 (1 Oct. 1967), pp. 162–172. DOI: [10.1103/PhysRev.162.162](https://doi.org/10.1103/PhysRev.162.162).
- [96] Elliott H. Lieb. “Exact Solution of the Two-Dimensional Slater KDP Model of a Ferroelectric”. In: *Phys. Rev. Lett.* 19 (3 July 1967), pp. 108–110. DOI: [10.1103/PhysRevLett.19.108](https://doi.org/10.1103/PhysRevLett.19.108).
- [97] Bill Sutherland. “Exact Solution of a Two-Dimensional Model for Hydrogen-Bonded Crystals”. In: *Phys. Rev. Lett.* 19 (3 July 1967), pp. 103–104. DOI: [10.1103/PhysRevLett.19.103](https://doi.org/10.1103/PhysRevLett.19.103).
- [98] Elliott H. Lieb. “Exact Solution of the Problem of the Entropy of Two-Dimensional Ice”. In: *Phys. Rev. Lett.* 18 (17 Apr. 1967), pp. 692–694. DOI: [10.1103/PhysRevLett.18.692](https://doi.org/10.1103/PhysRevLett.18.692).
- [99] Sergei Lukyanov and Véronique Terras. “Long-distance asymptotics of spin–spin correlation functions for the XXZ spin chain”. en. In: *Nuclear Physics B* 654.3 (Mar. 2003), pp. 323–356. ISSN: 0550-3213. DOI: [10.1016/S0550-3213\(02\)01141-0](https://doi.org/10.1016/S0550-3213(02)01141-0).
- [100] T Hikihara and A Furusaki. “Correlation amplitude for the S= 1 2 XXZ spin chain in the critical region: Numerical renormalization-group study of an open chain”. In: *Physical Review B* 58.2 (1998), R583.
- [101] Paul Ginsparg. “Curiosities at c= 1”. In: *Nuclear Physics B* 295.2 (1988), pp. 153–170.
- [102] P. Falco. “Arrow-arrow correlations for the six-vertex model”. In: *Phys. Rev. E* 88 (3 Sept. 2013), p. 030103. DOI: [10.1103/PhysRevE.88.030103](https://doi.org/10.1103/PhysRevE.88.030103).
- [103] P. Archambault et al. “Universal magnetic fluctuations in the two-dimensional XY model”. In: *Journal of Applied Physics* 83.11 (1998), pp. 7234–7236. DOI: [10.1063/1.367855](https://doi.org/10.1063/1.367855). eprint: <https://doi.org/10.1063/1.367855>.

- [104] J. Atchison et al. “Finite-size Kosterlitz-Thouless transition in 2DXY Fe/W(001) ultrathin films”. In: *Phys. Rev. B* 99 (12 Mar. 2019), p. 125425. DOI: [10.1103/PhysRevB.99.125425](https://doi.org/10.1103/PhysRevB.99.125425).
- [105] A. Moreo and D. J. Scalapino. “Two-dimensional negative-U Hubbard model”. In: *Phys. Rev. Lett.* 66 (7 Feb. 1991), pp. 946–948. DOI: [10.1103/PhysRevLett.66.946](https://doi.org/10.1103/PhysRevLett.66.946).
- [106] S. V. Isakov and R. Moessner. “Interplay of quantum and thermal fluctuations in a frustrated magnet”. In: *Phys. Rev. B* 68 (10 Sept. 2003), p. 104409. DOI: [10.1103/PhysRevB.68.104409](https://doi.org/10.1103/PhysRevB.68.104409).
- [107] Thereza Paiva et al. “Critical temperature for the two-dimensional attractive Hubbard model”. In: *Phys. Rev. B* 69 (18 May 2004), p. 184501. DOI: [10.1103/PhysRevB.69.184501](https://doi.org/10.1103/PhysRevB.69.184501).
- [108] Chuang Chen et al. “Fermi arcs and pseudogap in a lattice model of a doped orthogonal metal”. In: *Phys. Rev. B* 103 (16 Apr. 2021), p. 165131. DOI: [10.1103/PhysRevB.103.165131](https://doi.org/10.1103/PhysRevB.103.165131).
- [109] N. C. Costa et al. “Phonon Dispersion and the Competition between Pairing and Charge Order”. In: *Phys. Rev. Lett.* 120 (18 May 2018), p. 187003. DOI: [10.1103/PhysRevLett.120.187003](https://doi.org/10.1103/PhysRevLett.120.187003).
- [110] Weilun Jiang et al. “Monte Carlo study of the pseudogap and superconductivity emerging from quantum magnetic fluctuations”. In: *Nature Communications* 13 (2022), p. 2655. DOI: [10.1038/s41467-022-30302-x](https://doi.org/10.1038/s41467-022-30302-x).
- [111] Souvik Kundu and Kedar Damle. *Flux fractionalization transition in two-dimensional dimer-loop models*. 2023. arXiv: [2305.07012](https://arxiv.org/abs/2305.07012) [[cond-mat.stat-mech](https://arxiv.org/abs/2305.07012)].
- [112] J. M. Deutsch. “Quantum statistical mechanics in a closed system”. In: *Phys. Rev. A* 43 (4 Feb. 1991), pp. 2046–2049. DOI: [10.1103/PhysRevA.43.2046](https://doi.org/10.1103/PhysRevA.43.2046).
- [113] Mark Srednicki. “Chaos and quantum thermalization”. In: *Phys. Rev. E* 50 (2 Aug. 1994), pp. 888–901. DOI: [10.1103/PhysRevE.50.888](https://doi.org/10.1103/PhysRevE.50.888).
- [114] Marcos Rigol, Vanja Dunjko, and Maxim Olshanii. “Thermalization and its mechanism for generic isolated quantum systems”. In: *Nature* 452.7189 (Apr. 2008), pp. 854–858. ISSN: 1476-4687. DOI: [10.1038/nature06838](https://doi.org/10.1038/nature06838).
- [115] D.M. Basko, I.L. Aleiner, and B.L. Altshuler. “Metal–insulator transition in a weakly interacting many-electron system with localized single-particle states”. In: *Annals of Physics* 321.5 (2006), pp. 1126–1205. ISSN: 0003-4916. DOI: <https://doi.org/10.1016/j.aop.2005.11.014>.

- [116] I. V. Gornyi, A. D. Mirlin, and D. G. Polyakov. “Interacting Electrons in Disordered Wires: Anderson Localization and Low- T Transport”. In: *Phys. Rev. Lett.* 95 (20 Nov. 2005), p. 206603. DOI: [10.1103/PhysRevLett.95.206603](https://doi.org/10.1103/PhysRevLett.95.206603).
- [117] Vadim Oganesyan and David A. Huse. “Localization of interacting fermions at high temperature”. In: *Phys. Rev. B* 75 (15 Apr. 2007), p. 155111. DOI: [10.1103/PhysRevB.75.155111](https://doi.org/10.1103/PhysRevB.75.155111).
- [118] Bela Bauer and Chetan Nayak. “Area laws in a many-body localized state and its implications for topological order”. In: *Journal of Statistical Mechanics: Theory and Experiment* 2013.09 (Sept. 2013), P09005. DOI: [10.1088/1742-5468/2013/09/P09005](https://doi.org/10.1088/1742-5468/2013/09/P09005).
- [119] Maksym Serbyn, Z. Papić, and Dmitry A. Abanin. “Universal Slow Growth of Entanglement in Interacting Strongly Disordered Systems”. In: *Phys. Rev. Lett.* 110 (26 June 2013), p. 260601. DOI: [10.1103/PhysRevLett.110.260601](https://doi.org/10.1103/PhysRevLett.110.260601).
- [120] David A. Huse, Rahul Nandkishore, and Vadim Oganesyan. “Phenomenology of fully many-body-localized systems”. In: *Phys. Rev. B* 90 (17 Nov. 2014), p. 174202. DOI: [10.1103/PhysRevB.90.174202](https://doi.org/10.1103/PhysRevB.90.174202).
- [121] V. Ros and M. Müller. “Remanent Magnetization: Signature of Many-Body Localization in Quantum Antiferromagnets”. In: *Phys. Rev. Lett.* 118 (23 June 2017), p. 237202. DOI: [10.1103/PhysRevLett.118.237202](https://doi.org/10.1103/PhysRevLett.118.237202).
- [122] Jens H. Bardarson, Frank Pollmann, and Joel E. Moore. “Unbounded Growth of Entanglement in Models of Many-Body Localization”. In: *Phys. Rev. Lett.* 109 (1 July 2012), p. 017202. DOI: [10.1103/PhysRevLett.109.017202](https://doi.org/10.1103/PhysRevLett.109.017202).
- [123] Marko Žnidarič, Tomaž Prosen, and Peter Prelovšek. “Many-body localization in the Heisenberg XXZ magnet in a random field”. In: *Phys. Rev. B* 77 (6 Feb. 2008), p. 064426. DOI: [10.1103/PhysRevB.77.064426](https://doi.org/10.1103/PhysRevB.77.064426).
- [124] David J. Luitz, Nicolas Laflorencie, and Fabien Alet. “Many-body localization edge in the random-field Heisenberg chain”. In: *Phys. Rev. B* 91 (8 Feb. 2015), p. 081103. DOI: [10.1103/PhysRevB.91.081103](https://doi.org/10.1103/PhysRevB.91.081103).
- [125] Arijeet Pal and David A. Huse. “Many-body localization phase transition”. In: *Phys. Rev. B* 82 (17 Nov. 2010), p. 174411. DOI: [10.1103/PhysRevB.82.174411](https://doi.org/10.1103/PhysRevB.82.174411).
- [126] Titas Chanda, Piotr Sierant, and Jakub Zakrzewski. “Many-body localization transition in large quantum spin chains: The mobility edge”. In: *Phys. Rev. Res.* 2 (3 Aug. 2020), p. 032045. DOI: [10.1103/PhysRevResearch.2.032045](https://doi.org/10.1103/PhysRevResearch.2.032045).
- [127] Ivan V. Protopopov et al. “Non-Abelian Symmetries and Disorder: A Broad Non-ergodic Regime and Anomalous Thermalization”. In: *Phys. Rev. X* 10 (1 Feb. 2020), p. 011025. DOI: [10.1103/PhysRevX.10.011025](https://doi.org/10.1103/PhysRevX.10.011025).

- [128] Andrii O. Maksymov and Alexander L. Burin. “Many-body localization in spin chains with long-range transverse interactions: Scaling of critical disorder with system size”. In: *Phys. Rev. B* 101 (2 Jan. 2020), p. 024201. DOI: [10.1103/PhysRevB.101.024201](https://doi.org/10.1103/PhysRevB.101.024201).
- [129] Joshua M Deutsch. “Eigenstate thermalization hypothesis”. In: *Reports on Progress in Physics* 81.8 (July 2018), p. 082001. DOI: [10.1088/1361-6633/aac9f1](https://doi.org/10.1088/1361-6633/aac9f1).
- [130] Anatoli Polkovnikov Luca D’Alessio Yariv Kafri and Marcos Rigol. “From quantum chaos and eigenstate thermalization to statistical mechanics and thermodynamics”. In: *Advances in Physics* 65.3 (2016), pp. 239–362. DOI: [10.1080/00018732.2016.1198134](https://doi.org/10.1080/00018732.2016.1198134). eprint: <https://doi.org/10.1080/00018732.2016.1198134>.
- [131] M.L. Mehta. *Random Matrices*. Pure and applied mathematics vol. 142. Elsevier/Academic Press, 2004. ISBN: 9780120884094.
- [132] Y. Y. Atas et al. “Distribution of the Ratio of Consecutive Level Spacings in Random Matrix Ensembles”. In: *Phys. Rev. Lett.* 110 (8 Feb. 2013), p. 084101. DOI: [10.1103/PhysRevLett.110.084101](https://doi.org/10.1103/PhysRevLett.110.084101).
- [133] Don N. Page. “Average entropy of a subsystem”. In: *Phys. Rev. Lett.* 71 (9 Aug. 1993), pp. 1291–1294. DOI: [10.1103/PhysRevLett.71.1291](https://doi.org/10.1103/PhysRevLett.71.1291).
- [134] Maksym Serbyn, Dmitry A. Abanin, and Zlatko Papić. “Quantum many-body scars and weak breaking of ergodicity”. In: *Nature Physics* 17.6 (June 2021), pp. 675–685. ISSN: 1745-2481. DOI: [10.1038/s41567-021-01230-2](https://doi.org/10.1038/s41567-021-01230-2).
- [135] P. W. Anderson. “Absence of Diffusion in Certain Random Lattices”. In: *Phys. Rev.* 109 (5 Mar. 1958), pp. 1492–1505. DOI: [10.1103/PhysRev.109.1492](https://doi.org/10.1103/PhysRev.109.1492).
- [136] Elihu Abrahams. *50 Years of Anderson Localization*. WORLD SCIENTIFIC, 2010. DOI: [10.1142/7663](https://doi.org/10.1142/7663). eprint: <https://www.worldscientific.com/doi/pdf/10.1142/7663>.
- [137] Ferdinand Evers and Alexander D. Mirlin. “Anderson transitions”. In: *Rev. Mod. Phys.* 80 (4 Oct. 2008), pp. 1355–1417. DOI: [10.1103/RevModPhys.80.1355](https://doi.org/10.1103/RevModPhys.80.1355).
- [138] Dmitry A. Abanin et al. “Colloquium: Many-body localization, thermalization, and entanglement”. In: *Rev. Mod. Phys.* 91 (2 May 2019), p. 021001. DOI: [10.1103/RevModPhys.91.021001](https://doi.org/10.1103/RevModPhys.91.021001).
- [139] Fabien Alet and Nicolas Laflorencie. “Many-body localization: An introduction and selected topics”. In: *Comptes Rendus Physique* 19.6 (2018). Quantum simulation / Simulation quantique, pp. 498–525. ISSN: 1631-0705. DOI: <https://doi.org/10.1016/j.crhy.2018.03.003>.

- [140] J. Eisert, M. Cramer, and M. B. Plenio. “Colloquium: Area laws for the entanglement entropy”. In: *Rev. Mod. Phys.* 82 (1 Feb. 2010), pp. 277–306. DOI: [10.1103/RevModPhys.82.277](https://doi.org/10.1103/RevModPhys.82.277).
- [141] S. P. Lim and D. N. Sheng. “Many-body localization and transition by density matrix renormalization group and exact diagonalization studies”. In: *Phys. Rev. B* 94 (4 July 2016), p. 045111. DOI: [10.1103/PhysRevB.94.045111](https://doi.org/10.1103/PhysRevB.94.045111).
- [142] Vedika Khemani et al. “Critical Properties of the Many-Body Localization Transition”. In: *Phys. Rev. X* 7 (2 Apr. 2017), p. 021013. DOI: [10.1103/PhysRevX.7.021013](https://doi.org/10.1103/PhysRevX.7.021013).
- [143] Rajeev Singh, Jens H Bardarson, and Frank Pollmann. “Signatures of the many-body localization transition in the dynamics of entanglement and bipartite fluctuations”. In: *New Journal of Physics* 18.2 (Feb. 2016), p. 023046. DOI: [10.1088/1367-2630/18/2/023046](https://doi.org/10.1088/1367-2630/18/2/023046).
- [144] Hyungwon Kim and David A. Huse. “Ballistic Spreading of Entanglement in a Diffusive Nonintegrable System”. In: *Phys. Rev. Lett.* 111 (12 Sept. 2013), p. 127205. DOI: [10.1103/PhysRevLett.111.127205](https://doi.org/10.1103/PhysRevLett.111.127205).
- [145] Michael Schreiber et al. “Observation of many-body localization of interacting fermions in a quasirandom optical lattice”. In: *Science* 349.6250 (2015), pp. 842–845. DOI: [10.1126/science.aaa7432](https://doi.org/10.1126/science.aaa7432). eprint: <https://www.science.org/doi/pdf/10.1126/science.aaa7432>.
- [146] John Z. Imbrie. “Diagonalization and Many-Body Localization for a Disordered Quantum Spin Chain”. In: *Phys. Rev. Lett.* 117 (2 July 2016), p. 027201. DOI: [10.1103/PhysRevLett.117.027201](https://doi.org/10.1103/PhysRevLett.117.027201).
- [147] V. Ros, M. Müller, and A. Scardicchio. “Integrals of motion in the many-body localized phase”. In: *Nuclear Physics B* 891 (2015), pp. 420–465. ISSN: 0550-3213. DOI: <https://doi.org/10.1016/j.nuclphysb.2014.12.014>.
- [148] Wojciech De Roeck and François Huveneers. “Stability and instability towards delocalization in many-body localization systems”. In: *Phys. Rev. B* 95 (15 Apr. 2017), p. 155129. DOI: [10.1103/PhysRevB.95.155129](https://doi.org/10.1103/PhysRevB.95.155129).
- [149] K.S. Tikhonov and A.D. Mirlin. “From Anderson localization on random regular graphs to many-body localization”. In: *Annals of Physics* 435 (2021). Special Issue on Localisation 2020, p. 168525. ISSN: 0003-4916. DOI: <https://doi.org/10.1016/j.aop.2021.168525>.
- [150] Jan Šuntajs et al. “Quantum chaos challenges many-body localization”. In: *Phys. Rev. E* 102 (6 Dec. 2020), p. 062144. DOI: [10.1103/PhysRevE.102.062144](https://doi.org/10.1103/PhysRevE.102.062144).

- [151] D.A. Abanin et al. “Distinguishing localization from chaos: Challenges in finite-size systems”. In: *Annals of Physics* 427 (2021), p. 168415. ISSN: 0003-4916. DOI: <https://doi.org/10.1016/j.aop.2021.168415>.
- [152] M Schulz et al. “Phenomenology of anomalous transport in disordered one-dimensional systems”. In: *Journal of Statistical Mechanics: Theory and Experiment* 2020.2 (Feb. 2020), p. 023107. DOI: [10.1088/1742-5468/ab6de0](https://doi.org/10.1088/1742-5468/ab6de0).
- [153] Scott R. Taylor and Antonello Scardicchio. “Subdiffusion in a one-dimensional Anderson insulator with random dephasing: Finite-size scaling, Griffiths effects, and possible implications for many-body localization”. In: *Phys. Rev. B* 103 (18 May 2021), p. 184202. DOI: [10.1103/PhysRevB.103.184202](https://doi.org/10.1103/PhysRevB.103.184202).
- [154] Dries Sels and Anatoli Polkovnikov. “Dynamical obstruction to localization in a disordered spin chain”. In: *Phys. Rev. E* 104 (5 Nov. 2021), p. 054105. DOI: [10.1103/PhysRevE.104.054105](https://doi.org/10.1103/PhysRevE.104.054105).
- [155] Dries Sels and Anatoli Polkovnikov. “Thermalization of Dilute Impurities in One-Dimensional Spin Chains”. In: *Phys. Rev. X* 13 (1 Mar. 2023), p. 011041. DOI: [10.1103/PhysRevX.13.011041](https://doi.org/10.1103/PhysRevX.13.011041).
- [156] Alan Morningstar et al. “Avalanches and many-body resonances in many-body localized systems”. In: *Phys. Rev. B* 105 (17 May 2022), p. 174205. DOI: [10.1103/PhysRevB.105.174205](https://doi.org/10.1103/PhysRevB.105.174205).
- [157] Piotr Sierant et al. *Many-Body Localization in the Age of Classical Computing*. 2024. arXiv: [2403.07111](https://arxiv.org/abs/2403.07111) [[cond-mat.dis-nn](https://arxiv.org/abs/2403.07111)].
- [158] S A Parameswaran and Romain Vasseur. “Many-body localization, symmetry and topology”. In: *Reports on Progress in Physics* 81.8 (July 2018), p. 082501. DOI: [10.1088/1361-6633/aac9ed](https://doi.org/10.1088/1361-6633/aac9ed).
- [159] Aaron J. Friedman et al. “Localization-protected order in spin chains with non-Abelian discrete symmetries”. In: *Phys. Rev. B* 98 (6 Aug. 2018), p. 064203. DOI: [10.1103/PhysRevB.98.064203](https://doi.org/10.1103/PhysRevB.98.064203).
- [160] Abhishodh Prakash et al. “Eigenstate phases with finite on-site non-Abelian symmetry”. In: *Phys. Rev. B* 96 (16 Oct. 2017), p. 165136. DOI: [10.1103/PhysRevB.96.165136](https://doi.org/10.1103/PhysRevB.96.165136).
- [161] Ronen Vosk and Ehud Altman. “Many-Body Localization in One Dimension as a Dynamical Renormalization Group Fixed Point”. In: *Phys. Rev. Lett.* 110 (6 Feb. 2013), p. 067204. DOI: [10.1103/PhysRevLett.110.067204](https://doi.org/10.1103/PhysRevLett.110.067204).
- [162] R. Vasseur, A. C. Potter, and S. A. Parameswaran. “Quantum Criticality of Hot Random Spin Chains”. In: *Phys. Rev. Lett.* 114 (21 May 2015), p. 217201. DOI: [10.1103/PhysRevLett.114.217201](https://doi.org/10.1103/PhysRevLett.114.217201).

- [163] Ronen Vosk and Ehud Altman. “Dynamical Quantum Phase Transitions in Random Spin Chains”. In: *Phys. Rev. Lett.* 112 (21 May 2014), p. 217204. DOI: [10.1103/PhysRevLett.112.217204](https://doi.org/10.1103/PhysRevLett.112.217204).
- [164] David Pekker et al. “Hilbert-Glass Transition: New Universality of Temperature-Tuned Many-Body Dynamical Quantum Criticality”. In: *Phys. Rev. X* 4 (1 Mar. 2014), p. 011052. DOI: [10.1103/PhysRevX.4.011052](https://doi.org/10.1103/PhysRevX.4.011052).
- [165] Dimitris Saraidaris et al. *Finite-size subthermal regime in disordered $SU(N)$ -symmetric Heisenberg chains*. 2023. arXiv: [2304.03099](https://arxiv.org/abs/2304.03099) [quant-ph].
- [166] Miguel A. Cazalilla and Ana Maria Rey. “Ultracold Fermi gases with emergent $SU(N)$ symmetry”. In: *Reports on Progress in Physics* 77.12 (Nov. 2014), p. 124401. DOI: [10.1088/0034-4885/77/12/124401](https://doi.org/10.1088/0034-4885/77/12/124401).
- [167] Carsten Honerkamp and Walter Hofstetter. “Ultracold Fermions and the $SU(N)$ Hubbard Model”. In: *Phys. Rev. Lett.* 92 (17 Apr. 2004), p. 170403. DOI: [10.1103/PhysRevLett.92.170403](https://doi.org/10.1103/PhysRevLett.92.170403).
- [168] A. V. Gorshkov et al. “Two-orbital $SU(N)$ magnetism with ultracold alkaline-earth atoms”. In: *Nature Physics* 6.4 (Apr. 2010), pp. 289–295. ISSN: 1745-2481. DOI: [10.1038/nphys1535](https://doi.org/10.1038/nphys1535).
- [169] Pierre Nataf and Frédéric Mila. “Exact Diagonalization of Heisenberg $SU(N)$ Models”. In: *Phys. Rev. Lett.* 113 (12 Sept. 2014), p. 127204. DOI: [10.1103/PhysRevLett.113.127204](https://doi.org/10.1103/PhysRevLett.113.127204).
- [170] Francesca Pietracaprina et al. “Shift-invert diagonalization of large many-body localizing spin chains”. In: *SciPost Phys.* 5 (2018), p. 045. DOI: [10.21468/SciPostPhys.5.5.045](https://doi.org/10.21468/SciPostPhys.5.5.045).
- [171] Don N. Page. “Information in black hole radiation”. In: *Phys. Rev. Lett.* 71 (23 Dec. 1993), pp. 3743–3746. DOI: [10.1103/PhysRevLett.71.3743](https://doi.org/10.1103/PhysRevLett.71.3743).
- [172] Pierre Nataf and Frédéric Mila. “Density matrix renormalization group simulations of $SU(N)$ Heisenberg chains using standard Young tableaux: Fundamental representation and comparison with a finite-size Bethe ansatz”. In: *Phys. Rev. B* 97 (13 Apr. 2018), p. 134420. DOI: [10.1103/PhysRevB.97.134420](https://doi.org/10.1103/PhysRevB.97.134420).
- [173] Ivan V. Protopopov, Wen Wei Ho, and Dmitry A. Abanin. “Effect of $SU(2)$ symmetry on many-body localization and thermalization”. In: *Phys. Rev. B* 96 (4 July 2017), p. 041122. DOI: [10.1103/PhysRevB.96.041122](https://doi.org/10.1103/PhysRevB.96.041122).
- [174] D. Banerjee et al. “Interfaces, strings, and a soft mode in the square lattice quantum dimer model”. In: *Phys. Rev. B* 90 (24 Dec. 2014), p. 245143. DOI: [10.1103/PhysRevB.90.245143](https://doi.org/10.1103/PhysRevB.90.245143).

- [175] Tom Oakes et al. “Phases of quantum dimers from ensembles of classical stochastic trajectories”. In: *Phys. Rev. B* 98 (6 Aug. 2018), p. 064302. DOI: [10.1103/PhysRevB.98.064302](https://doi.org/10.1103/PhysRevB.98.064302).
- [176] Tiamhock Tay and Olexei I. Motrunich. “Possible Exciton Bose Liquid in a Hard-Core Boson Ring Model”. In: *Phys. Rev. Lett.* 105 (18 Oct. 2010), p. 187202. DOI: [10.1103/PhysRevLett.105.187202](https://doi.org/10.1103/PhysRevLett.105.187202).
- [177] Arun Paramekanti, Leon Balents, and Matthew P. A. Fisher. “Ring exchange, the exciton Bose liquid, and bosonization in two dimensions”. In: *Phys. Rev. B* 66 (5 Aug. 2002), p. 054526. DOI: [10.1103/PhysRevB.66.054526](https://doi.org/10.1103/PhysRevB.66.054526).
- [178] Geet Rakala, Kedar Damle, and Deepak Dhar. “Fractional Brownian motion of worms in worm algorithms for frustrated Ising magnets”. In: *Phys. Rev. E* 103 (6 June 2021), p. 062101. DOI: [10.1103/PhysRevE.103.062101](https://doi.org/10.1103/PhysRevE.103.062101).
- [179] Bhupen Dabholkar, G. J. Sreejith, and Fabien Alet. “Reentrance effect in the high-temperature critical phase of the quantum dimer model on the square lattice”. In: *Phys. Rev. B* 106 (20 Nov. 2022), p. 205121. DOI: [10.1103/PhysRevB.106.205121](https://doi.org/10.1103/PhysRevB.106.205121).
- [180] Andrew C. Potter and Romain Vasseur. “Symmetry constraints on many-body localization”. In: *Phys. Rev. B* 94 (22 Dec. 2016), p. 224206. DOI: [10.1103/PhysRevB.94.224206](https://doi.org/10.1103/PhysRevB.94.224206).
- [181] Chaitanya Murthy et al. “Non-Abelian Eigenstate Thermalization Hypothesis”. In: *Phys. Rev. Lett.* 130 (14 Apr. 2023), p. 140402. DOI: [10.1103/PhysRevLett.130.140402](https://doi.org/10.1103/PhysRevLett.130.140402).
- [182] Shayan Majidy et al. “Non-Abelian symmetry can increase entanglement entropy”. In: *Phys. Rev. B* 107 (4 Jan. 2023), p. 045102. DOI: [10.1103/PhysRevB.107.045102](https://doi.org/10.1103/PhysRevB.107.045102).